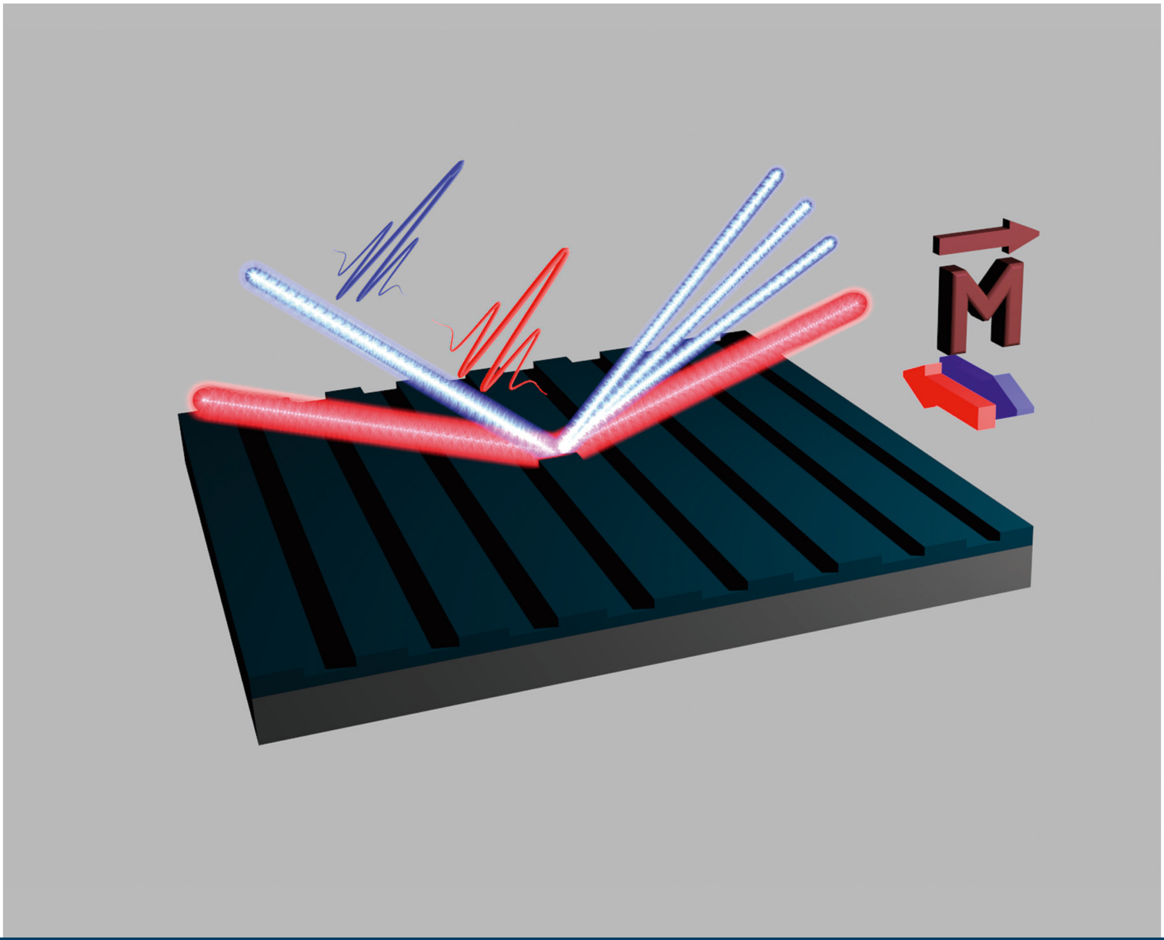

Element-Selective Investigation of Femtosecond Spin Dynamics in Ni_xPd_{1-x} Magnetic Alloys using Extreme Ultraviolet Radiation

Seung-gi Gang

Information
Band / Volume 58
ISBN 978-3-95806-411-9

Mitglied der Helmholtz-Gemeinschaft

JÜLICH
Forschungszentrum

Schriften des Forschungszentrums Jülich
Reihe Information / Information — Band / Volume 58

Forschungszentrum Jülich GmbH
Peter Grünberg Institut (PGI)
Elektronische Eigenschaften (PGI-6)

Element-Selective Investigation of Femtosecond Spin Dynamics in Ni_xPd_{1-x} Magnetic Alloys using Extreme Ultraviolet Radiation

Seung-gi Gang

Schriften des Forschungszentrums Jülich
Reihe Information / Information Band / Volume 58

ISSN 1866-1777 ISBN 978-3-95806-411-9

Bibliografische Information der Deutschen Nationalbibliothek.
Die Deutsche Nationalbibliothek verzeichnet diese Publikation in der
Deutschen Nationalbibliografie; detaillierte Bibliografische Daten
sind im Internet über http://dnb.d-nb.de abrufbar.

Herausgeber und Vertrieb: Forschungszentrum Jülich GmbH
Zentralbibliothek, Verlag
52425 Jülich
Tel.: +49 2461 61-5368
Fax: +49 2461 61-6103
zb-publikation@fz-juelich.de
www.fz-juelich.de/zb

Umschlaggestaltung: Grafische Medien, Forschungszentrum Jülich GmbH

Druck: Grafische Medien, Forschungszentrum Jülich GmbH

Schriften des Forschungszentrums Jülich
Reihe Information / Information, Band / Volume 58

D 464 (Diss., Duisburg, Univ., 2019)

ISSN 1866-1777
ISBN 978-3-95806-411-9

Zusammenfassung

Aufgrund der steigenden Nachfrage nach kleineren Speichermedien mit größerer Datenkapazität und schnellerer Datenverarbeitung, versuchen laufende theoretische und experimentelle Untersuchungen zu neuen magnetischen Materialien und deren physikalischen Mechanismen, die Grenzen magnetischer Aufzeichnung zu verstehen und voranzutreiben. Nach ersten Beobachtungen der ultraschnellen Entmagnetisierung in Nickel-Dünnschichtproben im Jahr 1996 wurde die optisch induzierte ultraschnelle Magnetisierungsdynamik durch Femtosekunden-Laserpulse als ein vielversprechender neuer Ansatz betrachtet, die bisherigen Grenzen zu überwinden und die Schaltgeschwindigkeit magnetischer Dünnschichtsysteme drastisch zu erhöhen. Des Weiteren konnte gezeigt werden, dass die optische Anregung eines Ferromagneten spinpolarisierte Elektronenströme im Femtosekundenbereich erzeugt, welche letztendlich dazu genutzt werden können, die Magnetisierung der Probe im Nanometerbereich zu manipulieren. In den letzten Jahren haben viele wissenschaftliche und technologische Entwicklungen, dazu gehören neue magnetische Materialien, theoretische Arbeiten und neue experimentelle Techniken, zu großen Fortschritten in Richtung schnellerer und kleinerer elektronische Geräte geführt.

Im Rahmen meines Promotionsprojekts wurden die stöchiometrieabhängigen Magnetisierungsdynamiken mehrerer Nickel-Palladium-Proben für verschieden Nickelanteile $\mathrm{Ni}_x\mathrm{Pd}_{1-x}$ untersucht, um zunächst Einblicke in die magnetischen Eigenschaften der Legierung aus Palladium und dem 3d ferromagnetischen Nickel zu gewinnen. Da das paramagnetische Palladium mit dem ferromagnetischen Nickel in der Legierung gekoppelt ist, wird erwartet, dass das Palladium ein magnetisches Moment erhält, welches durch verschiedene Messungen detektiert werden soll. Die Magnetisierungsdynamiken magnetischer Materialien hängt außerdem von weiteren magnetischen Eigenschaften wie der Curie-Temperatur, dem magnetischen Moment und der Spin-Flip-Streuwahrscheinlichkeit ab. Durch Variation des Ni-Pd-Mischungsverhältnisses haben wir, aufgrund der höheren Ordnungszahl Palladiums im Vergleich zu Nickel, die Spin-Bahn-Kopplung in der Legierung abgestimmt und deren Einfluss auf die Entmagnetisierungsdynamik auf Femtosekunden-Zeitskalen untersucht.

Obwohl es viele theoretische Modelle gibt, die die Spin- und Magnetisierungsdynamik in magnetischen Legierungen und Mehrschichtsystemen erklären wollen, ist der zugrundeliegende physikalische Mechanismus noch unklar. Die experimentellen Studien, die in meiner Dissertation ausführlich beschrieben wurden, liefern zusätzliche Erkenntnisse, die die Suche nach den Mechanismen der ultraschnellen Magnetisierungsdynamik in ferromagnetischen Legierungen unterstützt. Die vorliegende Analyse der stöchiometrieabhängigen Dynamik wurde auf Basis des mikroskopischen Drei-Temperatur-Modells (M3TM) durchgeführt.

In meiner Doktorarbeit verwendete ich laser-erzeugtes XUV-Licht, um die ultraschnelle Magnetisierungsdynamik der Legierungen im Femtosekundenbereich zu untersuchen. Das XUV-Licht mit Photonenenergie im Bereich von 20 bis 72 eV wurde durch den sogenannten HHG-Prozess (High Harmonic Generation) erzeugt, indem ein intensiver Femtosekunden-Laserpuls in eine mit Neongas gefüllte Kapillare fokussiert wurde. Um die dynamische Antwort der Legierungen zu erfassen, verwendete ich Messungen auf Basis des transversal magneto-optischen Kerr-Effekts (T-MOKE) in Form einer Infrarot-Anrege-XUV-Abfrage-Geometrie. Um die Dynamik in Ni- und Pd-Subsystemen mit Elementselektivität zu messen, wurde die spektroskopische Analyse durch Strukturieren einer Gitterstruktur an der Oberfläche der Proben durchgeführt.

Ausgehend von statischen Messungen habe ich während meiner Diplomarbeit zum ersten Mal die induzierte Magnetisierung in elementarem Paramagneten Pd in einer ferromagnetischen Legierung unter Verwendung von lasergeneriertem XUV-Licht gemessen. Dies ermöglichte es mir, sowohl statische als auch dynamische Messungen der Magnetisierung der Legierungen mit Elementselektivität durchzuführen. Die induzierte Magnetisierung an der Pd $N_{2,3}$–Absorptionskante aus statischen Messungen entspricht der theoretischen Berechnung auf Basis der Dichtefunktionaltheorie [1]. Die stöchiometrieabhängige Dynamik, die bei konstanter Anregefluenz durchgeführt wurde, variiert mit der Curie-Temperatur. Die Magnetisierungsdynamik mit höheren Pd-Konzentrationen zeigte im Vergleich zu den niedrigen Pd-Konzentrationen ein stärkeres Quenching und eine langsamere Relaxationszeit. Ich fand heraus, dass in Übereinstimmung mit früheren Untersuchungen [2] die Abhängigkeit mit T/T_C skaliert, wobei T_C die Curie-Temperatur ist. Zusätzlich zu der stöchiometrisch abhängigen Dynamik mit konstantem Quenching fand ich heraus, dass ein höherer Pd-Gehalt zu einer Verringerung der Entmagnetisierungszeit führt, was in guter Übereinstimmung mit der $\tau_M \propto \mu_{AT}/a_{sf}T_C$-Skalierung des M3T-Modelles ist, welches aufgrund der Spin-Bahn-Kopplung mit a_{sf}^4 skaliert. Die vorgestellten Daten weisen auf eine entscheidende Rolle der Spin-Bahn-Kopplung in der Femtosekunden-Magnetisierungsdynamik in ferromagnetischen Legierungen hin.

Abstract

Since Beaurepaire et al. discovered optically induced ultrafast magnetization dynamics in Ni thin films in 1996, a variety of experimental and theoretical studies have been made to understand the underlying physical mechanism of the magnetization dynamics. Among the suggested mechanisms, spin-flip electron-phonon scattering described by the microscopic three-temperature model (M3TM)[3] and superdiffusive spin transport[4],[5] are currently considered to be major physical mechanisms contributing substantially to the ultrafast spin dynamics. It is believed that more than one mechanism is responsible for the dynamics. The analysis of magnetization dynamics in $\mathrm{Ni}_x\mathrm{Pd}_{1-x}$ alloys with varying composition presented in this thesis provides deeper insight into the relation between the spin dynamics and spin-orbit coupling (SOC) in these materials. Our measurements were mostly done in the transversal magneto-optic Kerr effect (T-MOKE) geometry. To measure ultrafast magnetization dynamics with element selectivity, femtosecond pulses in the extreme ultraviolet (XUV) regime have been produced by laser-based high-order harmonic generation (HHG) in a noble gas. The XUV light from neon gas with an energy range from 20 to 72 eV covering the $\mathrm{M}_{2,3}$-edges of ferromagnetic materials (52.7 eV for Fe, 58.9 eV for Co, and 68, 66.2 eV for Ni) can be expanded to form a spectrum, by a optical grating introduced on the sample surface. The magnetic contrast and the optically-induced dynamic response can be obtained using XUV light with energy corresponding to the absorption edges of the involved elements. In the $\mathrm{Ni}_x\mathrm{Pd}_{1-x}$ alloys, the intrinsically paramagnetic Pd is expected to be magnetically coupled to ferromagnetic Ni via complex exchange paths. One can study spin dynamics in the paramagnetic material (Pd) with induced magnetic moment as a consequence of the exchange coupling with ferromagnetic material (Ni). In addition, element selective measurements allow investigation of questions related to a possible superdiffusive spin transport between the Ni and Pd subsystems. The influence of the increased SOC on the spin dynamics in the $\mathrm{Ni}_x\mathrm{Pd}_{1-x}$ alloys can be also investigated by varying the mixing ratio of Ni and Pd in the alloy system. From static T-MOKE, we experimentally confirmed that increasing the Pd content in the alloy gives rise to a pronounced magnetic asymmetry of a bipolar shape at the Pd N_3-absorption edge (50.9 eV). Varying the mixing ratio in the $\mathrm{Ni}_x\mathrm{Pd}_{1-x}$ alloy changes the magnetic properties such as the magnetic moment μ, the Curie temperature T_C, and the spin-flip scattering probability a_{sf} of the alloy. We show that these parameters are closely related to the magnetization dynamics. Especially, the spin-flip scattering probability a_{sf} scales with the atomic number Z as $a_{sf} \propto Z^4$ due to SOC. The magnetization dynamics in the $\mathrm{Ni}_x\mathrm{Pd}_{1-x}$ alloys can be tuned by the alloy stoichiometry due to a considerable difference in atomic numbers of Ni (Z_{Ni}=28) and Pd (Z_{Pd}=46). Our results can then be explained by considering the spin-flip scattering probability a_{sf}

within the framework of M3TM, and point to the crucial role of the Pd-mediated SOC in optically-induced spin dynamics in the $\mathrm{Ni}_x\mathrm{Pd}_{1-x}$ alloys.

Contents

Chapter 1

Introduction

Our daily life is inseparable from information and electronic technology accompanied with a fast development of personal computers and smartphones. After realization of the first digital computer in the 1940's, the performance of the computer circuits has advanced quickly, approximately doubling the number of transistors on densely integrated chips every 2 years (Moore's law). The performance of the first computers filling a whole room can be now miniaturized into mobile devices even with huge storage capacity. Furthermore, the rapidly increasing flow of information worldwide raises the demand for not only huge recording capacity, but also for new techniques that would reduce the time necessary for saving and reading the information. The present memory devices are able to save and read data on the nanosecond time scale. To decrease the time for data processing even below the nanosecond barrier, utilizing the interaction of short pulsed laser light and magnetic materials has been considered as a promising approach. In 1996, the optically-induced demagnetization of Ni thin films on femtosecond timescales employing the time-resolved magneto-optic Kerr effect (TR-MOKE) was observed by Beaurepaire et al. [6] The authors explained the optically induced magnetization dynamics with the three-temperature model (3TM) considering three different subsystems modelled by heat baths: the electron-, lattice- and spin bath, each having a specific temperature and interacting with each other. In this model, during laser excitation, the energy absorbed by the sample increases first the temperature of electrons in the electron bath and the heat is subsequently transferred to the other baths following different time scales. The authors of Ref. [6] only consider heat transfer between the baths. There is no consideration of angular momentum transfer, which is essential to describe the demagnetization process. Nevertheless, this discovery stimulated the study of ultrafast magnetization in magnetic materials and strong progress has been made in understanding the underlying mechanisms of the interaction between the femtosecond light pulse and the magnetic materials. Several mechanisms have been suggested and two mechanisms among them have been favored as plausible explanations for the demagnetization process. First, Elliott-Yafet type spin-flip scattering between electrons and phonons in the microscopic three-temperature model (M3TM) is considered as a channel for dissipation of angular momentum [3]. In this model the spin-flip process is proportional to spin-flip scattering probability, a_{sf}, which depends on and strongly affects the demagnetization time τ_M ($\tau_M \sim 1/a_{sf}$). The other mechanism is superdiffusive spin transport in magnetic multilayers, which involves the mean free path difference of majority- and minority spin electrons after optical excitation. There is no direct description of a channel for angular momentum transfer in this mechanism, either. For instance, in 3d transition metals, majority spin electrons optically excited from the d-band to sp-like states above the Fermi level have a higher mobility than that of the d-band electrons. Consequently, the sp-like electrons can travel longer distances resulting in a spin-polarized transport with an assumption that the electron spin is conserved after the optical excitation. The superdiffusive spin transport was theoretically described in [4],[7] and experimentally observed in [5],[8],[9],[10]. Later experiments showed that both superdiffusive spin current and spin-flip scattering are responsible for the spin dynamics [11]. In this case, the dynamics in a multilayer system with different spacer materials between the ferromagnetic layers was investigated, and the two mechanisms were separately investigated by using also spacer materials with short spin lifetime. According to these results, the two mechanisms with different microscopic descriptions simultaneously contribute to the dynamics on a comparable time scale.

Besides spin dynamics resulting in demagnetization, the excitation by a laser pulse may result in a complete magnetization reversal in some magnetic materials systems. In Ref. [12], the authors investigated ferrimagnetic GdFeCo, in which Fe and Gd spins are antiferromagnetically coupled and the magnetization reversal of the Fe and Gd subsystems induced by optical excitation was observed by element-specific X-ray dichroism. The magnetization reversal was explained with the following process. After optical excitation, the temperature of electronic system initially increases and the thermal energy is transferred to the spin system leading to a demagnetization in Fe and Gd subsystems with different characteristic time scales. Since the demagnetization and reversal of the Fe subsystem happens on much shorter times ($\sim$ 300 fs) than that of Gd subsystem ($\sim$ 1.5 ps), Fe and Gd exhibit a temporary ferromagnetic spin alignment and the reversal of the Gd subsystem takes place due to antiferromagnetic exchange relaxation between the Fe and Gd subsystems. Further numerical and experimental investigations of optically-induced magnetization switching can be found in [13]. In Ref. [14] Graves et al. investigated inhomogeneous ferrimagnetic GdFeCo of similar composition as in the Ref. [12]. The samples were found to be consisting of Gd-rich and Fe-rich nanoregions. By optical excitation, both types of the nanoregions are initially demagnetized. After about 1 ps, only the Gd-rich region exhibits magnetization reversal, but not the Fe-rich regions. The angular momentum transfer by *lateral* spin current from Fe-rich to Gd-rich region is considered to be the mechanism responsible for the magnetization reversal in Gd-rich region.

Up to date, a spin transport-related magnetization dynamics has been considered in several different types of magnetic systems. In Ref. [5], Rudolf et al. experimentally confirmed the existence of spin transfer between spatially separated metallic layers. This mechanism is generally possible, because spin majority electrons have a longer mean free path than minority spin electrons. In Ref. [14], *lateral* spin transport causing an angular momentum transfer from Fe-rich to Gd-rich region was used to explain the optically-induced switching of inhomogeneous GdFeCo as explained above. Finally, Bar'yakhtar and collaborators predicted that in multicomponent alloys an exchange interaction related spin relaxation could cause longitudinal spin dissipation of atomic moments leading to local spin currents between atoms [15],[16]. In 2018, J. K. Dewhurst et al. theoretically demonstrated changes in the magnetic structure including a magnetization switching in both multilayer (e.g. Mn/Co/Cu(001)) and alloy systems (e.g. FePt with 33% Mn) via optically-induced intersite spin transfer (OISTR) [17]. The OISTR takes place within short time scale (less than 40 fs) in which spin-orbit induced spin-flip scattering is insignificant for magnetization dynamics. It remains an open question whether such physical pictures can be applied to homogeneous multicomponent $\mathrm{Ni}_x\mathrm{Pd}_{1-x}$ alloys, the system of choice for our investigation. There is no complete theory to describe the ultrafast magnetization dynamics yet. Instead, theoretical studies and experimental observations suggest that more than one mechanism is responsible for the ultrafast magnetization dynamics by ultrafast optical excitation.

In this thesis, magnetization properties and spin dynamics in $\mathrm{Ni}_x\mathrm{Pd}_{1-x}$ magnetic alloys are investigated with element selectivity. In the $\mathrm{Ni}_x\mathrm{Pd}_{1-x}$ alloy, Pd that almost fulfills the Stoner criterion magnetically couples to Ni and acquires a magnetic moment due to complex exchange interaction. This thesis especially treats the magnetic signature of the intrinsically paramagnetic Pd subsystem by the exchange coupling with the ferromagnetic Ni subsystem. In addition, the effect of Pd-mediated spin-orbit coupling (SOC) on the spin dynamics is also considered with varying the mixing ratio of Ni and Pd. To examine this idea, an experimental technique based on the transversal magneto-optic Kerr effect (T-MOKE) with XUV light has been mainly employed. The T-MOKE detects difference of reflected intensities of XUV on a magnetic sample surface with external magnetic fields in opposite directions, and the difference provides the magnetic asymmetry of the sample. In static measurements, the induced magnetization in the Pd subsystem and the magnetic asymmetry change in Ni and Pd are experimentally investigated. The change of magnetic asymmetries in Ni and Pd is explained by d-band dispersion which comes from stoichiometry-dependent SOC and hybridization of Ni and Pd in the alloys [18]. In dynamic measurements, a pump-probe technique is employed to measure the composition-dependent dynamics of the $\mathrm{Ni}_x\mathrm{Pd}_{1-x}$ alloys. In our experiment, we tuned the magnetic properties of the alloys, such as Curie temperature, atomic magnetic moment and spin-flip scattering probability by varying the mixing ratio of Ni and Pd. As the demagnetization time depends on these parameters, we observed changes of the magnetization dynamics in $\mathrm{Ni}_x\mathrm{Pd}_{1-x}$ alloys for different compositions. In addition, we experimentally confirmed that spin-orbit coupling must be taken into account in order to fully understand the dynamics in $\mathrm{Ni}_x\mathrm{Pd}_{1-x}$ alloys. A brief description of Chapters is given below:

Chapter 2 provides the theoretical basis of magnetism and ferromagnetism in 3d transition metals. The magnetic properties of $\mathrm{Ni}_x\mathrm{Pd}_{1-x}$ alloys with different compositions are discussed in view of their effect on spin dynamics. In addition, physical mechanisms for ultrafast magnetization dynamics are discussed expanding to the microscopic description.

Chapter 3 gives information about the sample preparation process and the characterization of the $\mathrm{Ni}_x\mathrm{Pd}_{1-x}$ alloys. Magnetic hysteresis of $\mathrm{Ni}_x\mathrm{Pd}_{1-x}$ alloys is measured by longitudinal MOKE (L-MOKE). In addition, energy-dependent reflectivity of the thin film grating sample for precise analysis of the magnetic asymmetry is also presented.

Chapter 4 describes the experimental setup employed for the measurements. The femtosecond laser system and high-harmonic generation (HHG) for extreme ultraviolet (XUV) radiation from a waveguide filled with noble gas are shown. Schematic pump-probe T-MOKE setup for the dynamic measurement is also discussed. In the experimental scheme part, the general concept of the magneto-optic Kerr effect (MOKE) for the magnetization measurement is introduced and especially the transversal MOKE (T-MOKE) geometry is presented in detail. The chapter gives also a description of the HHG process employed to produce XUV light pulses.

Chapter 5 presents the analysis and discussion of the magnetization and the dynamics in the $\mathrm{Ni}_x\mathrm{Pd}_{1-x}$ alloys. From the static measurements, the special emphasis is placed on the induced magnetic asymmetry in the intrinsically paramagnetic Pd due to exchange coupling with ferromagnetic Ni. Technical details of data analysis such as subpixel shift correction are presented. In the dynamics part, the optically induced magnetization dynamics of the Ni and Pd subsystems are compared. Temperature-dependent dynamics of Ni subsystem due to the different Curie temperature tuned by the mixing ratio is investigated. Furthermore, the dependence of the demagnetization on varying composition of the $\mathrm{Ni}_x\mathrm{Pd}_{1-x}$ alloys is presented and related to the strength of the spin-orbit coupling. The data analysis is based on the microscopic three-temperature model (M3TM).

Chapter 6 summarizes and lists important conclusions of the presented study and Chapter 7 presents further scientific approaches in magnetization dynamics for practical applications as an Outlook.

Chapter 2

Fundamental Considerations

2.1 Magnetism

The following section gives a brief consideration of the theoretical understanding of magnetic interactions starting from the simplest two-electron system such as the H_2 molecule and expand to the larger ferromagnetic systems. A more detailed fundamental description of magnetism can be found in [19], [20].

2.1.1 Magnetic Moment

We start with the magnetic properties of the single electron. The magnetic moment of an electron, $\vec{m}_{electron}$, consists of two parts. First, movement of the charged particle, seen as a stationary electric ring current, is leading to an orbital magnetic moment, $\vec{m}_{orb}$, related to classical orbital angular momentum, $\vec{l}$, by:

$$\vec{m}_{orb} = -\frac{e\mu_0}{2m_e}\vec{l} \tag{2.1}$$

with the elementary charge e, the vacuum permeability μ_0, and the electron mass m_e. The classical definition of the orbital angular moment can be converted to the quantum mechanical expression by considering that the angular momentum $\vec{l}$ is quantized in integer multiples of Plank's constant. The expectation value of $\langle l_z \rangle = \hbar \mathrm{l}_z$ along z-axis leads to the quantum mechanical expression:

$$< m_o^z > = -\frac{e\mu_0}{2m_e}\hbar l_z. \tag{2.2}$$

Second, the spin magnetic moment, $\vec{m}_{spin}$, originates from the intrinsic quantum property of the particle related to spin angular momentum, $\vec{s}$ (observed first in the Stern-Gerlach experiment[21]). The spin magnetic moment is given by:

$$\vec{m}_{spin} = -\frac{e\mu_0}{m_e}\vec{s}\ . \tag{2.3}$$

The quantum mechanical expression of 2.3 can be written as:

$$< m_s^z >= -\frac{e\mu_0}{m_e}\hbar s_z. \tag{2.4}$$

where $\vec{s}$ can have values of $+\hbar/2$ or $-\hbar/2$. The total electron magnetic moment in quantum mechanical expression is given by:

$$< m_{total}^z >=< m_o^z > + < m_s^z >= -\frac{\mu_B}{\hbar}(g_s \langle s_z \rangle + g_l \langle l_z \rangle) \tag{2.5}$$

where $\mu_B = e\mu_0\hbar/2m_e$ indicates the Bohr magneton. The g-factors for the spin- and orbital moments are given by $g_s=2$ and $g_l=1$ in atomic regime. In pure 3d transition metals as solid states, the g-factors are 2.09, 2.18, and 2.21 for Fe, Co, and Ni. These values deviate from the spin-only considered value of 2.0 by a small amount in consequence of the presence of an orbital moment. The orbital moment contribution to the total magnetic moment of 3d transition metal is about 4-10% and the magnetic moments for 3d transition metals are predominantly governed by the spin of the 3d electrons. Although the orbital moment has relatively small contribution to the total magnetic moment, it is essential for magnetism since the orbital moment and the g-factor are anisotropic to the lattice directions.

Nuclei are also charged particles with magnetic moment. However, the nuclei have about 3 order higher masses compared to that of electrons. As the magnetic moment is inversely proportional to the mass of particle, contribution of the nuclei to the overall magnetic moment of an atom can be neglected.

Ferromagnetism is governed by a collective behavior of the electron magnetic moments leading to a macroscopic magnetization in a material, which can be described by band and ligand field methods. The macroscopic magnetic moment, $\vec{M}$, is related to the microscopic magnetic moment, $\vec{m}$, by adding all N number of elementary magnetic dipole moments $\vec{m}$ in the volume V:

$$\vec{M} = \frac{N}{V}\vec{m}\ . \tag{2.6}$$

Most magnetic materials except diamagnetic materials exhibit a paramagnetic behavior with the magnetization $\vec{M}$ of the material being proportional to an external magnetic field $\vec{B_0}$:

$$\mu_0 \vec{M} = \chi \vec{B_0} \tag{2.7}$$

where μ_0, χ indicate the vacuum permeability and the magnetic susceptibility. On the other hand, the macroscopic magnetic properties of 3d transition metals such as Fe, Co, Ni are governed by ferromagnetic characteristics with spontaneous magnetic order. The *atomic* transition metals can have a 12 possible electrons in 3d and 4s shells and the unfilled states in the 3d shell determine their magnetic properties. According to the Hund's rules, Fe, Co, and Ni have 4, 3, and 2 unpaired electrons, which determine the magnetic spin moments. The Fe with 4 unpaired electrons exhibits the spin magnetic moment, m_s=$4\mu_B$. Similarly Co and Ni are predicted to have spin moments of $3\mu_B$ and $2\mu_B$, respectively. In *solid* state of 3d transition metals, the total atomic moments are not exactly multiples of the Bohr magneton. According to the spontaneous magnetization in 3d transition metals, the atomic moments are $2.216\mu_B$, $1.715\mu_B$, and $0.616\mu_B$ for Fe, Co, and Ni, respectively. This means that the 3d electrons are not strictly localized, instead the electrons are itinerant leading to orbital magnetic moments. This can be described by the *band-like model* of ferromagnetism (see Section 2.1.3). The atomic model gives the atomic moments including spin and orbital contribution as $6\mu_B$, $6\mu_B$, $5\mu_B$ for Fe, Co, and Ni. The severe difference in the atomic moments between the atomic model and the measurements is due to the overestimation of the orbital magnetic moments in the atomic model. Since 3d electrons participate in the bonding with the ligands in ionic system such as transition metal oxides, the *ligand field* effects leading to significant quenching of the orbital magnetic moments by the bonding should be considered [22],[23].

2.1.2 Exchange Interaction

In magnetic materials, the magnetic moment $\vec{M}$ of the material is established by alignment of the electron magnetic moments. The spontaneous alignment in a ferromagnetic material originates from the fundamental mechanism called exchange interaction. In 1926, Heisenberg employed the concept of exchange interaction for interpretation of the He spectrum [24]. The exchange interaction is a quantum mechanical effect between identical particles such as electrons and considered as the strongest magnetic interaction. The exchange interaction comes from the Coulomb interaction between electrons

and the symmetrization postulate. Under exchange of indistinguishable particles considering exchange symmetry, the symmetric (antisymmetric) system gives unchanged (changed) sign of the wavefunctions of the particles. The exchange interaction for electrons appears as Pauli repulsion related to Pauli exclusion principle [25].
Ferromagnets can be divided into two groups according to the origin of collective spin ordering; i.e., itinerant and localized ferromagnets [26]. Ferromagnetism in the itinerant ferromagnets represented by 3d transition metals arises from electrons in the valance band. Here, the electrons are only weakly bound to the atoms and are moving in a crystal potential. The ferromagnetism in rare earth elements arises from localized spin-polarized 4f-electrons strongly bound to the atom. The 4f-electrons are not contributing to the chemical properties of the atoms, and the elements with magnetic moment fixed at lattice points can be theoretically treated in a spin-lattice model [27]. In this Section, the localized magnetism in rare earth ferromagnets is discussed. The ferromagnetism in 3d transition metals is explained in Section 2.1.3.

In order to describe the electronic and spin structure of atoms, the modified Schrödinger equation that includes electron spin should be taken into account [28],[29]. For a basic understanding of exchange interaction, the simplest 2-electron system can be considered first. The time-independent Pauli equation for the system can be written as:

$$[\mathcal{H}_e + \mathcal{H}_s]\psi(\vec{r}, \vec{s}) = E\psi(\vec{r}, \vec{s}) \tag{2.8}$$

The H$_e$ in Equation 2.8 indicates the spherically symmetric central field electronic Hamiltonian given as:

$$\mathcal{H}_e = \sum_{i=1}^{N} \left(\frac{p_i^2}{2m_e} - \frac{Ze^2}{4\pi\epsilon_0 |r_i|} \right) + \sum_{i<j} \frac{e^2}{4\pi\epsilon_0 |r_j - r_i|} \tag{2.9}$$

In Equation 2.9, the first term in the brackets indicates kinetic energy and the second the Coulomb interaction between the electrons and the nucleus. The last term stands for the Coulomb interaction between the electrons and leads to the exchange interaction and correlation. The second term in Equation 2.8, $\mathcal{H}_s$, is the nonrelativistic spin energy and related to the *spin-orbit interaction* which will be discussed in the section 2.1.4.
The one-electron wave functions including spin can be written as:

$$\psi(a) = \psi_{n,l,m}(r, s) = R_{n,l}(r)Y_{l,m}(\theta, \phi)\chi(s_z). \tag{2.10}$$

Considering two indistinguishable electrons marked 1,2 bound to the atomic cores A,B as the two hydrogen atoms with covalent bond and neglecting Coulomb repulsion, the Heitler-London approximation provides a spatial wave function as:

$$\Psi(a,b) = \frac{1}{\sqrt{2}}[\psi_1(a)\psi_2(b) \pm \psi_2(a)\psi_1(b)] \tag{2.11}$$

Here, + stands for symmetric and - for antisymmetric spatial wave functions. The spin wave function should be also taken into consideration for describing the total wave function. Antisymmetric- and symmetric spin wave functions are given as:

$$\chi_{as}(s_1,s_2) = \frac{1}{\sqrt{2}}[\alpha\beta - \beta\alpha] \tag{2.12}$$

$$\chi_{sym}(s_1,s_2) = \begin{cases} \alpha\alpha \\ \frac{1}{\sqrt{2}}[\alpha\beta + \beta\alpha]. \\ \beta\beta \end{cases} \tag{2.13}$$

where α and β indicate spin-up and spin-down states. The total wave function can be expressed by a product of spatial- and spin-wave functions, and the total wave function must be antisymmetric under the exchange operation according to the *Symmetrization Postulates* written as:

$$\Psi_{as}(a,b) = \Psi_{sym}(r_1,r_2)\chi_{as}(s_1,s_2) \tag{2.14}$$

or

$$\Psi_{as}(a,b) = \Psi_{as}(r_1,r_2)\chi_{sym}(s_1,s_2). \tag{2.15}$$

Equation 2.14 stands for a spin singlet state and Equation 2.15 for a spin triplet state.

The simplest 2-electron system has been discussed above, and we now expand the system to the solid state. The magnetic property of a material arises from collective contributions of all involved electrons, therefore the interactions between electrons should be included as well in perturbation calculations. By including the Coulomb repulsion described by Coulomb integral I and the exchange interaction described by the exchange integral J, the consequent energies of the singlet and triplet states can be described by:

$$E_s = E_0 + I + J, \tag{2.16}$$

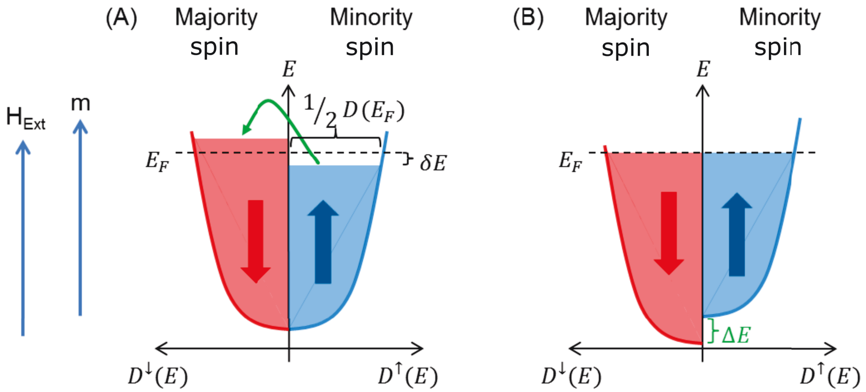

FIGURE 2.1: (A) Spin redistribution from the minority band into unoccupied states in the majority band leading to increased kinetic energy of the system. (B) Exchange splitting (ΔE) from the increased kinetic energy and the gain of exchange energy. Herein the direction of external magnetic field is parallel to the direction of magnetic moment of the system($\vec{H}_{ext} \| \vec{m}$). Due to the relation of $\vec{m}$=-g$\mu_B \vec{s}$, the majority spins have opposite direction (spin-down) to the magnetic moment of the system.

$$E_t = E_0 + I - J \tag{2.17}$$

where E_0 is the energy of the ground state of the hydrogen atom. For J>0, parallel spin coupling of two electrons is energetically favorable and antiparallel coupling for J<0. The energy difference between the singlet and triplet states ($\Delta E = 2J$) represents the *exchange splitting*. In a ferromagnetic metal, the exchange splitting is typically about 1 eV. This is magnetic exchange interaction applicable for deeply bound localized electrons in the case of 4f-rare earth ferromagnets. The magnetism of 3d transition materials with itinerant 3d-electrons should be explained by interaction of electrons in the Stoner model of metallic ferromagnetism with the spin-resolved density of states (DOS).

2.1.3 Ferromagnetism in 3d Transition Metals

As discussed in the Section 2.1.1, the non-integer multiple of the Bohr magneton numbers in the ferromagnetic metals could be explained by the band theory. The Stoner model is the simplest band-like model which accounts for the itinerant ferromagnetism in 3d transition metals [30],[31]. In Figure 2.1, the Stoner model can be applied to the spin-resolved density of states (DOS) with an assumption that spin-down electrons are redistributed into unoccupied spin-up states. While the system gains the exchange energy, the redistributed spin-down electrons experience an increase of the kinetic energy by δE. The number of majority (minority) electrons is increased (decreased) by δN=$\frac{1}{2}$D(E$_F$)δE. As discussed above, the redistribution of spins gives rise to increase of the kinetic energy density per volume V in the system:

$$\Delta E_{kin} = \frac{\delta N}{V}\delta E = \frac{1}{2V}D(E_F)(\delta E)^2 \tag{2.18}$$

The redistribution of spin also causes a change in Coulomb energy density which can be written as:

$$\Delta E_C = -\frac{I}{2V}D(E_F)^2(\delta E)^2 \tag{2.19}$$

which is proportional to the square of the magnetization of the system, M.[1] Thus, the total energy change in the system by spin redistribution is expressed as:

$$\Delta E = \Delta E_{kin} + \Delta E_C = \frac{1}{2V}D(E_F)(\delta E)^2[1 - I \cdot D(E_F)]. \tag{2.20}$$

If ΔE is negative, then the system assumes a ferromagnetic state. The condition to be fulfilled for band ferromagnetism in a solid is given as:

$$I \cdot D(E_F) \geq 1 \tag{2.21}$$

which is called the Stoner Criterion [32]. For all 3d-transition metals, the exchange interaction is similar leading to a Stoner parameter I $\sim$ 1 eV [33],[34], the density of state at the Fermi level, D(E$_F$), is the dominant parameter to determine the ferromagnetism in 3d transition metals.

2.1.4 Spin-Orbit Interaction

In previous sections, the magnetic moment of single electrons and the interaction between electron-electron (exchange interaction) have been discussed. In this section, we deal with the spin-orbit interaction, which is the interaction between the spin, $\vec{s}$, of the electron and the magnetic field induced by electron's orbital motion around the nucleus in the presence of a Coulomb potential [19],[20],[26]. The Hamiltonian, $\mathcal{H}_s$, related to the SOC is given by:

---

[1] The magnetization of the system is given by M = -μ_B(n$_\uparrow$-n$_\downarrow$)) = -$\mu_B\frac{D(E_F)}{V}\delta E$.

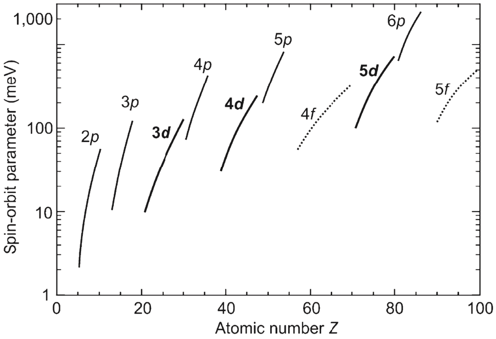

Figure 2.2: Calculated values for the spin-orbit parameter ξ for the valence shells of neutral atoms in ground state [35].

$$\vec{\mathcal{H}}_L = \frac{2\mu_B}{\hbar m_e c^2}\frac{1}{r}\frac{dV(r)}{dr}\,\vec{L}\cdot\vec{S}\,. \tag{2.22}$$

However, the SOC Hamiltonian in Equation 2.22 contains only the interaction between the magnetic moment of the electron and the magnetic field of the nucleus, the so-called Larmor interaction energy. The motion of the electron along a curved trajectory, the so-called Thomas precession correction, must also be considered:

$$\vec{\mathcal{H}}_T = -\frac{\mu_B}{\hbar m_e c^2}\frac{1}{r}\frac{dV(r)}{dr}\,\vec{L}\cdot\vec{S}\,. \tag{2.23}$$

Then, the total SOC Hamiltonian in a spherical potential is obtained as:

$$\vec{\mathcal{H}}_s = \vec{\mathcal{H}}_L + \vec{\mathcal{H}}_T = \frac{\mu_B}{\hbar m_e c^2}\frac{1}{r}\frac{dV(r)}{dr}\,\vec{L}\cdot\vec{S} = \xi(r)\,\vec{L}\cdot\vec{S}\,. \tag{2.24}$$

$\xi(r)$ is called the spin-orbit coupling constant and $\xi(r) \propto (1/r)dV/dr \sim -Z\,|e|\,/r^3 \propto -Z^4$, because of the expectation value $\left\langle 1/r^3 \right\rangle \propto Z^3$ where Z is the atomic number. Therefore, in general, heavy atoms and alloys with heavy averaged effective atomic number show stronger SOC. Figure 2.2 shows the calculated spin-orbit parameters with varying Z values [35]. Regarding the electron subshells, the SOC is especially stronger for p-electrons since the s-orbital has no angular momentum and the p-electron has a larger amplitude of wavefunction being close to the nucleus compared to d- or f-electron. The 3d transition metals normally exhibit relatively small spin-orbit interaction, $\Delta E_{SO} = 0.01 - 0.1eV$ compared to the exchange interaction $\Delta E_{Ex} \approx 1eV$ and the ligand field interaction (a few eV). In contrast, the 4f rare-earths have the larger spin-orbit interaction with the smaller ligand field effects leading to larger orbital magnetic moments for the lanthanides.

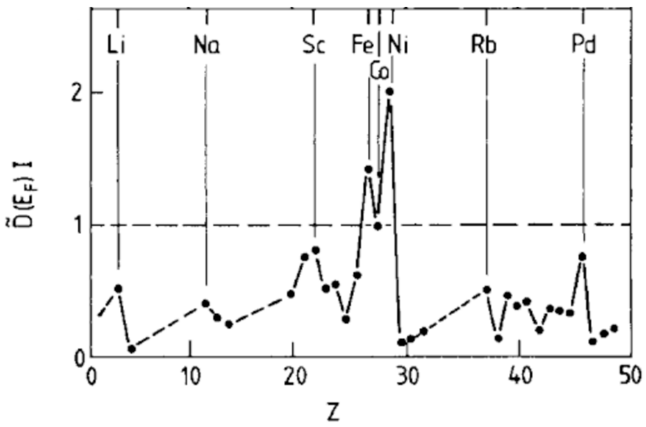

FIGURE 2.3: Product of the Stoner exchange coupling parameter I and the density of states at the Fermi energy per spin direction $\tilde{D}$ for different elements [40]. For ferromagnetic materials (Fe, Co and Ni), I is larger than unity fulfilling the Stoner criterion. Pd in its elemental state is a paramagnetic transition metal, which has the product close to unity nearly fulfilling the Stoner criterion.

In solids, the difference of SO interaction along the magnetic easy-axis and hard-axis determines the magnetocrystalline anisotropy, i.e. the magnetocrystalline anisotropy is the energy required to rotate the magnetization from the easy-axis to the hard-axis [19].

2.2 Properties of $\mathrm{Ni}_x\mathrm{Pd}_{1-x}$ alloys

For application of mass data storage technology with enhanced performance, the magnetic properties of complex magnetic alloys and compounds of 3d transition metals in thin film structure have been extensively investigated [36],[37],[38]. The study can be extended to magnetic alloys of 3d transition metals with other materials. The alloys of 3d and 5d elements, e.g. $\mathrm{Co}_x\mathrm{Pt}_{1-x}$, shows unique magneto-optical properties due to higher spin-orbit coupling of the 5d elements [39]. Alloys of 3d and 4d elements are also expected to give different magnetic or/and dynamic properties compared to the alloys of 3d transition metals. The main purpose of this study is to investigate the magnetic properties in $\mathrm{Ni}_x\mathrm{Pd}_{1-x}$ alloys and to study how the dynamics of the alloys changes with increasing Pd concentration in the system. Thus, it is reasonable to start with a description of the properties of Pd and $\mathrm{Ni}_x\mathrm{Pd}_{1-x}$ alloys. While forming an alloy, Pd atoms are expected to magnetically couple to Ni. This section describes the properties of the $\mathrm{Ni}_x\mathrm{Pd}_{1-x}$ alloys such as magnetization, Curie temperature and electronic structure.

According to the Stoner criterion as shown in Figure 2.3, Pd is one of paramagnetic transition metals that nearly fulfills the Stoner criterion for ferromagnetism. Pd has the

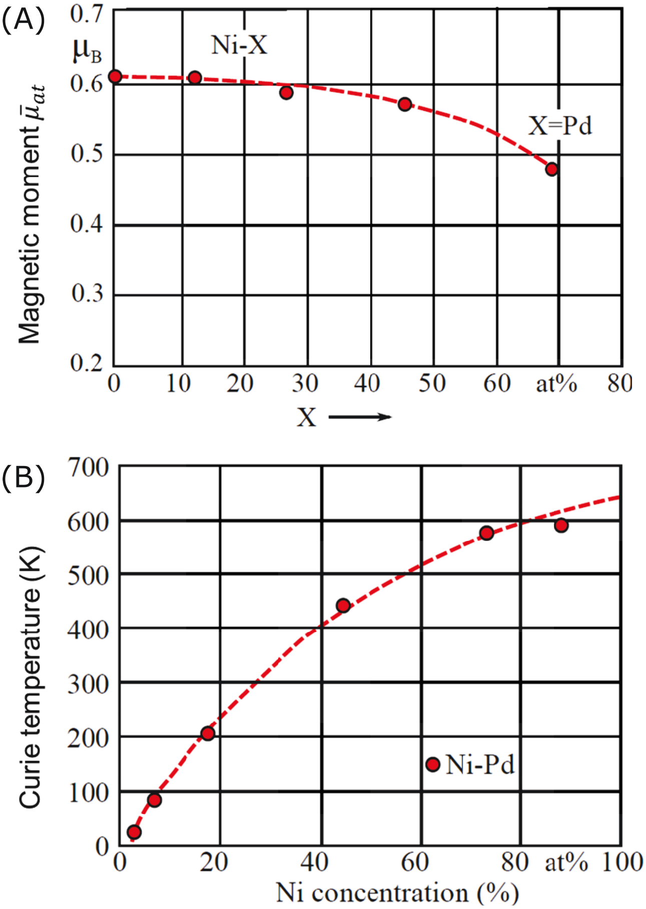

FIGURE 2.4: Magnetic moment and Curie temperature of the $\mathrm{Ni}_x\mathrm{Pd}_{1-x}$ alloy changing with stoichiometry [41]. (A) Influence of Pd, a paramagnetic transition metal, in $\mathrm{Ni}_x\mathrm{Pd}_{1-x}$ alloy on magnetic moment per atom of the compound. 50% of Pd in the alloy leads to about 10% drop in the magnetic moment compared to pure Ni. (B) Curie temperature variation in the $\mathrm{Ni}_x\mathrm{Pd}_{1-x}$ alloy with different compositions. 50% of Pd in the alloy leads to about 30% drop of Curie temperature.

fascinating magnetic property that it develops a high exchange interaction with a large magnetic moment if brought in close proximity to another ferromagnet. Figure 2.4 shows the properties of the $\mathrm{Ni}_x\mathrm{Pd}_{1-x}$ alloys with varying Pd content. A magnetic moment of $\mathrm{Ni}_x\mathrm{Pd}_{1-x}$ alloys with increasing Pd content in Figure 2.4(A) indicates that up to 50% Pd concentration in the alloy results in only about 10% drop in the average magnetic moment of the alloy as compared to pure Ni. This behavior suggests that paramagnetic Pd atoms can be polarized by coupling with Ni. As the alloy with increasing Pd content exhibits gradual decrease of magnetic moment, Pd atoms are expected to be ferromagnetically coupled to Ni atoms in the system. In addition, the Curie temperature T_C, of

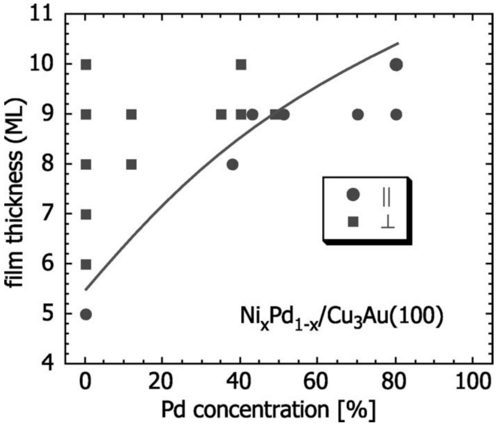

FIGURE 2.5: Thickness- and stoichiometry-dependent magnetic phase of the $\mathrm{Ni}_x\mathrm{Pd}_{1-x}$ films on $\mathrm{Cu_3Au}(100)$ substrate [42]. As Pd content in the alloy increases, magnetization direction turns from out-of-plane($\perp$) to in-plane($||$).

the alloys in Figure 2.4(B) shows that 50% of Pd contents in the alloy leads to about 30% drop of Curie temperature compared to pure Ni. Magnetic moment and Curie temperature are important parameters for determining the spin dynamics in $\mathrm{Ni}_x\mathrm{Pd}_{1-x}$ alloys. In particular, the microscopic three-temperature model (M3TM) suggests that the demagnetization time τ_M scales as $\tau_M \sim \mu/a_{sf}T_C$, where the spin-flip scattering probability a_{sf} depends on the stoichiometry.

The $\mathrm{Ni}_x\mathrm{Pd}_{1-x}$ thin films have different properties compared to that of bulk. In the bulk, $\mathrm{Ni}_x\mathrm{Pd}_{1-x}$ alloys have a stable fcc-phase for all compositions and exhibit ferromagnetic ordering in the range of $0.03 \leq x \leq 1$. The thin film properties are determined by crystalline structure, chemical composition and electronic structure [42].
Spin reorientation transition (SRT) of the $\mathrm{Ni}_x\mathrm{Pd}_{1-x}$ alloys on *single crystalline* $\mathrm{Cu_3Au}(100)$ was experimentally observed as a function of composition and film thickness (see Figure 2.5) [42]. The SRT is strain-driven and originated from the lattice mismatch between the thin film and the substrate. In our study, on the other hand, the $\mathrm{Ni}_x\mathrm{Pd}_{1-x}$ alloys were epitaxially grown on *polycrystalline* $\mathrm{SiO_2}$ substrate and the film thickness was kept constant at 20 nm, therefore, the SRT by tuning strain effect cannot be achieved due to averaged lattice parameter of the polycrystalline substrate. Thus, the stoichiometry-dependent SRT of the $\mathrm{Ni}_x\mathrm{Pd}_{1-x}$ thin films on the $\mathrm{SiO_2}$ substrate is mainly determined by contribution of Pd introducing higher spin-orbit interaction compared to Ni. In Section 3.2, the L-MOKE results can be interpreted by Pd-mediated spin-orbit interaction depending on the composition of the alloy (see Section 3.2).

The electronic structure of $\mathrm{Ni}_x\mathrm{Pd}_{1-x}$ alloy will be discussed to understand the magnetic properties such as magnetic anisotropy on the basis of the observation by U. Muschiol

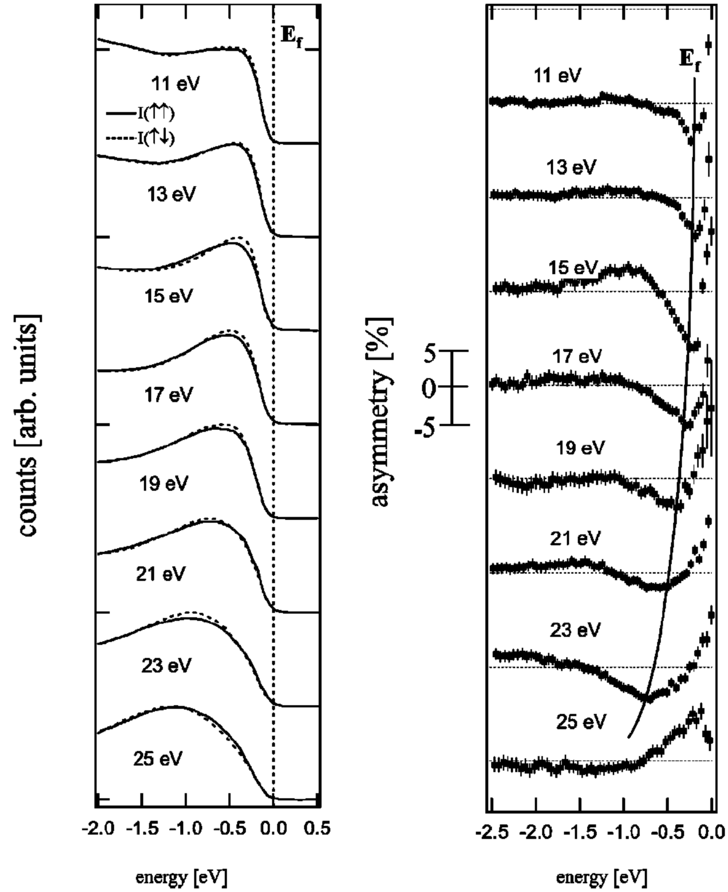

FIGURE 2.6: Intensity and asymmetry spectra of the 15 ML Ni$_{83}$Pd$_{17}$ film on Cu$_3$Au(100) substrate from magnetic circular dichroism in valence band photoemission [18]. Solid (dashed) lines indicates parallel (antiparallel) alignment of magnetization and helicity.

et al.[18]. In order to describe and manipulate the electronic structure of the alloy, two spin-dependent interactions, exchange- and spin-orbit interactions, should be taken into account and tuned by varying the stoichiometry. Both interactions vary throughout the Brillouin zone and depend on the band symmetry and the degree of hybridization. Ni shows an average experimental exchange splitting of 0.3 eV and Pd is known to have a comparable value along $\Gamma - X$ direction [43],[44]. The energy splittings ΔE_{SO} of Ni and Pd by spin-orbit interaction along $\Gamma - X$ are 0.1 eV and 0.3 eV [44],[45].

Figure 2.6 shows intensity and asymmetry spectra of 15 ML Ni$_{0.83}$Pd$_{0.17}$ alloy from the magnetic circular dichroism in valence band photoemission (MCDAD) [18]. This Figure indicates that the increasing photon energy leads to the minus asymmetry peak

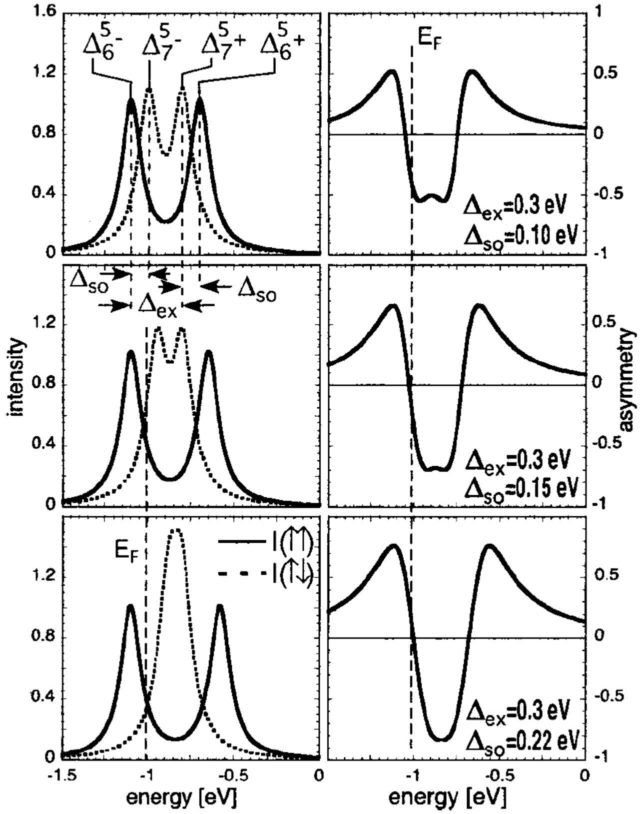

FIGURE 2.7: Influence of increasing spin-orbit interaction on ΔE_{ex} and ΔE_{SO} leading to change of intensity and asymmetry spectra [18].

broadening and movement of the peak to higher binding energy as a verification of band dispersion. At higher photon energies, asymmetry shows plus feature which is missed at initial states of interband transition from Δ^5_{-6} and Δ^5_{-7} (see Figure 2.7). Appearance of plus asymmetry can be interpreted by suppression of initial state Δ^5_{-6}.

The authors of [18] suggest and evaluate three possible effects, spin-orbit coupling, structural effect (like a rigid band shift) and hybridization effect, to explain the band dispersion.

Figure 2.7 shows influence of increasing SOC on intensity and asymmetry. The top figure shows initial states (ΔE^5_{-6}, ΔE^5_{-7}, ΔE^5_{+6}, ΔE^5_{+7}) which split due to the combination of exchange interaction and SOC. In the spectra, ΔE^5_{-6}, ΔE^5_{+6} stand for positive feature of asymmetry and ΔE^5_{-7}, ΔE^5_{+7} for negative feature. As SOC increases, the ΔE^5_{-7}, ΔE^5_{+7} contributing minus feature become dominant in the asymmetry and shift to higher binding energies close to E_F. In contrast, the plus feature by ΔE^5_{-6} shows weakened

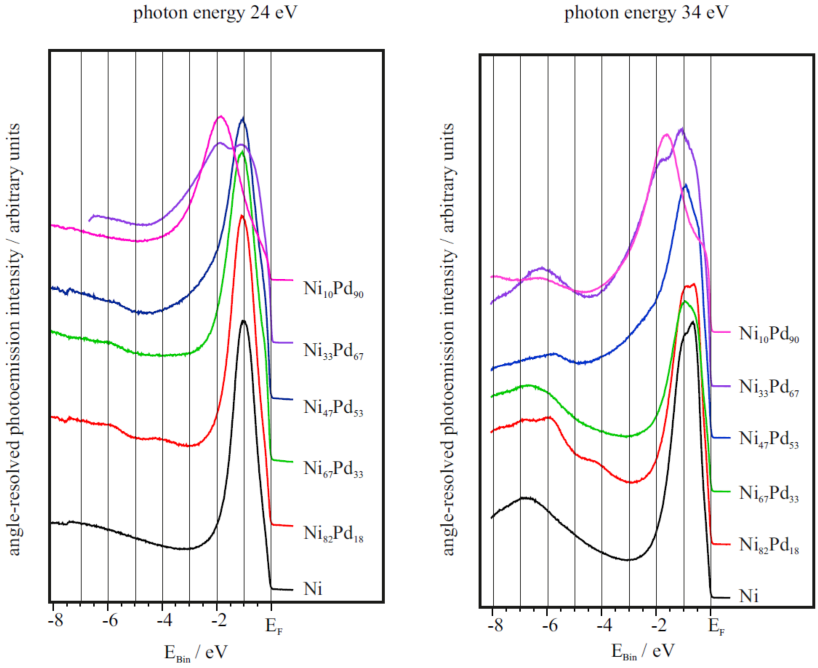

FIGURE 2.8: Photoemission spectra of Ni$_x$Pd$_{1-x}$ alloys shows peak shift and broadening with increasing Pd content (Courtesy of F. Matthes from Forschungszentrum Jülich).

spectral weight by the band dispersion.

Structural effects on the band dispersion can be also taken into account. As the thickness of NiPd film increases, its structure relaxes to a face-centered-cubic (fcc) determining the energetic position of d-band. The film thickness is kept constant as 20 nm in this study, the effect of structure on the band dispersion will not be considered in this study. The final possible explanation could be electronic hybridization between Ni and Pd. The band dispersion of Ni$_{83}$Pd$_{17}$ as shown in Figure 2.6 is similar to that of pure Ni since the mixing effects for low Pd content do not make a considerable effect on the electronic band structure. For higher Pd content such as Ni$_{0.5}$Pd$_{0.5}$ alloy, the band structure of the alloy is no longer Ni like and the stronger band dispersion comes from the mixing and hybridization effect of Δ^5-like states with Δ^1 and Δ^2 states in the energy range between Fermi level and 2.5 eV binding energy.

The Figure 2.8 shows stoichiometry-dependent photoemission spectra for fixed excitation energies (Courtesy of F. Matthes from Forschungszentrum Jülich). For Pd-rich alloys, intensity contribution from the peaks with energy dispersion becomes more dominant due to the lower Δ^1 symmetry band. The broadening of the spectral weight of the main peak just below Fermi level observed for all composition comes from chemical disorder of the $\mathrm{Ni}_x\mathrm{Pd}_{1-x}$ alloys.

There is no clear theoretical explanation for composition-dependent change in the magnetic asymmetry of $\mathrm{Ni}_x\mathrm{Pd}_{1-x}$ alloys (see Figure 5.4 in Section 5.1). The composition-dependent band dispersion due to the SO interaction and electronic hybridization of Ni and Pd in the alloys could be a possible explanation.

2.3 Ultrafast Magnetization Dynamics

In this section, we discuss ultrafast magnetization dynamics in ferromagnetic materials. We give a short description of the three temperature model (3TM) that had been also used for description of the ultrafast dynamics in Ni thin films done by Beaurepaire in 1996. Furthermore, the 3TM model is expanded to a microscopic three-temperature model (M3TM) to explain the demagnetization via Elliot-Yafet spin-flip scattering processes. Finally, we briefly discuss the superdiffusive spin transport model for spin dynamics in magnetic multilayer and alloy system.

2.3.1 Elliot-Yafet mechanism and the Three Temperature Model

In 1996, Beaurepaire et al. observed optically induced untrafast magnetization dynamics in a Ni film [6]. For analysis of the spin dynamics with a sufficient temporal resolution, a magneto-optical pump-probe experiment using femtosecond pulse laser was performed. To explain the spin dynamics in Ni film, Beaurepaire et al. introduced a phenomenological three temperature model (3TM), where the electon-, the lattice- and the spin subsystems, interact with each other. Energy exchange between these so-called baths is described by means of heat transfer with the exchange constants (G_{el}, G_{ls}, and G_{es}) between the baths and specific heats, C_i, assigned for each bath. The modeling was done by tracing the temperature change of the baths for varying temporal delay between the pump- and the probe pulse. The temperature evolution of the baths can then be described by the three coupled differential equations as follows:

$$\begin{aligned}
C_e(T_e)\frac{dT_e}{dt} &= -G_{el}(T_e - T_l) - G_{es}(T_e - T_s) + P(t) \\
C_s(T_s)\frac{dT_s}{dt} &= -G_{es}(T_s - T_e) - G_{sl}(T_s - T_l) \\
C_l(T_l)\frac{dT_l}{dt} &= -G_{el}(T_l - T_e) - G_{sl}(T_l - T_s)
\end{aligned} \tag{2.25}$$

The ultrafast process starts from interaction between the laser pulse and the electron bath by which the energy of the pulse, P(t), is deposited into the electron bath leading

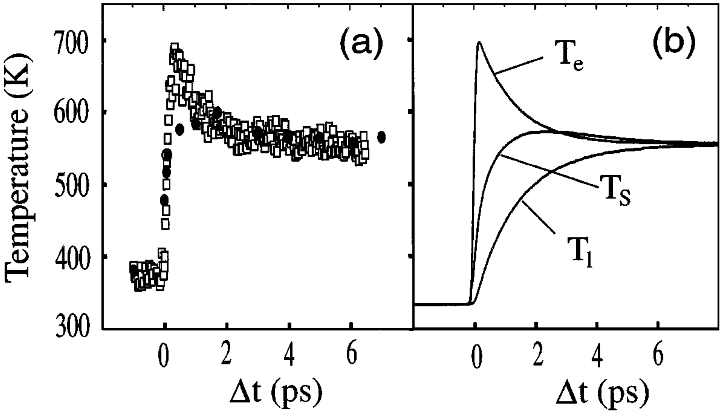

FIGURE 2.9: The figure on the left shows the experimental observation of the electronic- (empty squares) and the spin temperature (solid circles) on the femtosecond time scale after optical excitation. On the right, the calculated temperature evolution of electron- (T_e), spin- (T_s) and lattice baths (T_l) after excitation as predicted by 3TM is shown based on Equation 2.25 [6].

to an increase of the temperature in the electron bath. From there, the deposited energy is then transferred to the other baths as heat, mediated by the interaction constants, G, until the temperatures of all baths are stabilized at a common value (see Figure 2.9). Please note that the 3TM only considers the heat transfer between the three heat baths, and no transfer of angular momentum, which is essential to describe the demagnetization process. Koopmans et al. expanded the 3TM including a channel for angular momentum transfer - the microscopic three temperature model (M3TM)[3].

In this model, the dissipation of angular momentum is achieved through Elliot-Yafet type spin-flip scattering processes between the electron and phonon(lattice) subsystems with the spin-flip scattering probability, a_{sf}. During the scattering process, schematically shown in Figure 2.10, the angular momentum of the spin is transferred to the lattice and simultaneously the spin of electron is flipped. Energy exchange between the baths and the channel for angular momentum dissipation are shown in the Figure 2.11.

Koopmans et al. modified the Equations 2.25 introducing the Elliot-Yafet spin-flip scattering probability, a_{sf}, and the new equations can be given as:

$$\begin{aligned}
&C_e(T_e)\frac{dT_e}{dt} = \nabla_z(\kappa\nabla_z T_e + g_{ep}(T_p - T_e)) \\
&C_p(T_s)\frac{dT_s}{dt} = g_{ep}(T_e - T_p) \\
&\frac{dm}{dt} = Rm\frac{T_p}{T_C}\left(1 - mcoth(\frac{mT_C}{T_e})\right) \\
&\text{where R}= \frac{8a_{sf}g_{ep}k_bT_C{}^2V_{at}}{(\mu_{at}/\mu_B)E_D{}^2}.
\end{aligned} \tag{2.26}$$

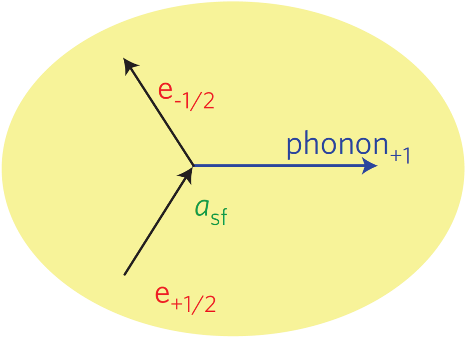

Figure 2.10: The spin-flip scattering process results in the scattered spin flipped and angular momentum transferred from electron to lattice [3].

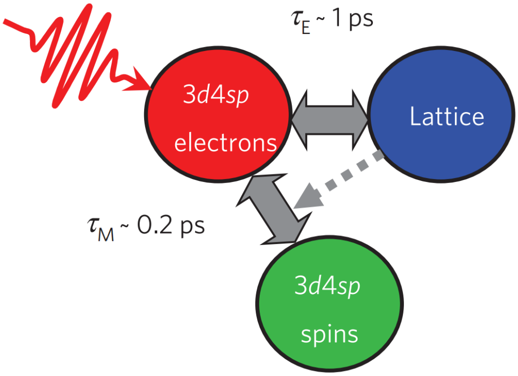

Figure 2.11: Schematic diagram for the three temperature baths (3TM) indicates laser-induced demagnetization in the 3d4sp band of 3d transition metals [3]. The full arrows indicate the energy exchange between the baths. The dashed arrow indicates the channel for angular momentum dissipation.

Here, κ is the (electronic) thermal conductivity, a$_{sf}$ the spin-flip scattering probability, V$_{at}$ the atomic volume, E$_D$ the Debye energy, and μ_{at} the atomic magnetic moment. To characterize the magnetization dynamics of a material, series of data points with varying time delay between pump- and probe pulses are fitted by a double exponential fitting function [38],[46]:

$$m(t) = 1 - \Delta m \cdot (1 - e^{-\frac{t-t_0}{\tau_M}}) \cdot e^{-\frac{t-t_0}{\tau_E}} \tag{2.27}$$

where t$_0$ indicates zero-delay, where the pump- and the probe pulses completely overlap in time at the sample surface. The amount of quenching Δm, the demagnetization time τ_M and the relaxation time τ_R are extracted. The demagnetization time τ_M and the relaxation time τ_R quantify, how fast the magnetic material loses and recovers its

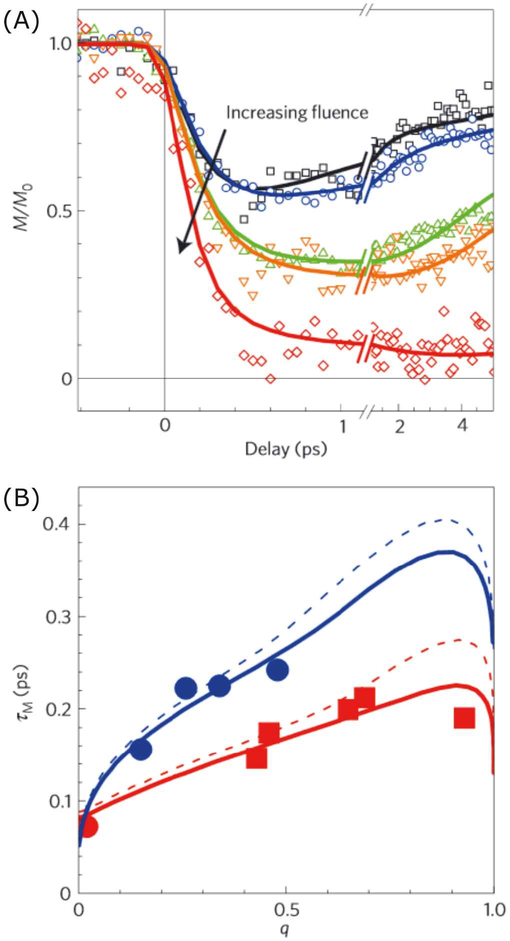

Figure 2.12: Magnetization quenching dependent demagnetization time τ_M [3]. (A) Demagnetization of pure Ni film (10 nm) with increasing pump fluence brings the higher magnetization quenching q. (B) Higher magnetization quenching gives rise to increase of the demagnetization time τ_M. A drop of the demagnetization time appears at very high magnetization quenching.

magnetization as a response to the optical excitation. It was experimentally shown in pure Ni [3] that the higher quenching due to higher pump fluence leads to an increase of τ_M and that τ_M starts to decrease at very high quenching as shown in Figure 2.12.

A number of experiments and theoretical studies have been done to understand the optically induced demagnetization process in magnetic materials, especially concerning the underlying physical mechanisms of the spin dynamics. Our current understanding suggests that more than one physical mechanism is responsible for the spin dynamics in magnetic materials. The following section covers the mechanisms, which are the most actively pursued to describe the spin dynamics in magnetic materials.

2.3.2 Superdiffusive Spin Transport

Superdiffusive spin transport is also one of the mechanisms involved to explain experimental results. As shown in Figure 2.13, Rudolf et al. measured the magnetization dynamics of Ni/Ru/Fe trilayer system with element-selectivity by employing extreme ultraviolet light [5]. After optical excitation, the magnetization of a Fe film in a trilayer system was surprisingly enhanced when the Ni- and Fe film have a parallel alignment of the magnetization. In contrast, the magnetizations of both films are quenched after optical excitation when the magnetization vectors of the films are aligned in antiparallel direction. The dynamics in the multilayer system as stated above cannot be explained by the Eliott-Yafet type scattering alone, but instead superdiffusive spin transport model has to be applied.

Superdiffusive spin transport, which was introduced by Battiato et al.[4] in 2010 is an intermediate process connecting the diffusive- and ballastic regime. Considering the spin-resolved density of states for 3d transition metals, the excited majority spin can only occupy the 4sp-states, since 3d-states are not available for the majority spin (see Figure 2.14). The 4sp-states are less localized than 3d-states, in consequence the majority spin electrons have a higher mobility. The majority spin electrons of 3d transition metals are excited to more than 1 eV above the Fermi level with the 1.5 eV photon energy of the pump beam [46],[5],[11]. In this energy regime, the motion of the majority spin electrons has a longer mean free path so that the electrons can travel from one layer to the neighboring layer in a multilayer thin film system in the ballastic regime. After some time the majority spin electrons start to scatter with other electrons and thermalize to the Fermi level by diffusive spin transport. The total process is thus named as superdiffusive spin transport. Rudolf et al. have shown that there is an upper limit of pump fluence, which induces superdiffusive spin transport. There are more publications, which experimentally confirm the superdiffusive spin transport within magnetic multilayer systems. In 2008, G. Malinowski et al. measured the magnetization dynamics in a $[Co/Pt]_N$ multilayer system with out-of-plane magnetization. For antiferromagnetic spin alignment between the Co and Pt layers, optical excitation leads to higher demagnetization and shorter demagnetization time τ_M that can be ascribed to direct spin momentum transfer [8]. In 2013, the validity of supersiffusive spin transport within Ni/Ru/Fe was experimentally confirmed by Mathias et al. [46]. The authors of [46] also include the effect of exchange coupling on the dynamics of Ni-Fe and Ni-Fe-Cu alloy systems in 2013. In the same year, T. Kampfrath et al. theoretically and experimentally

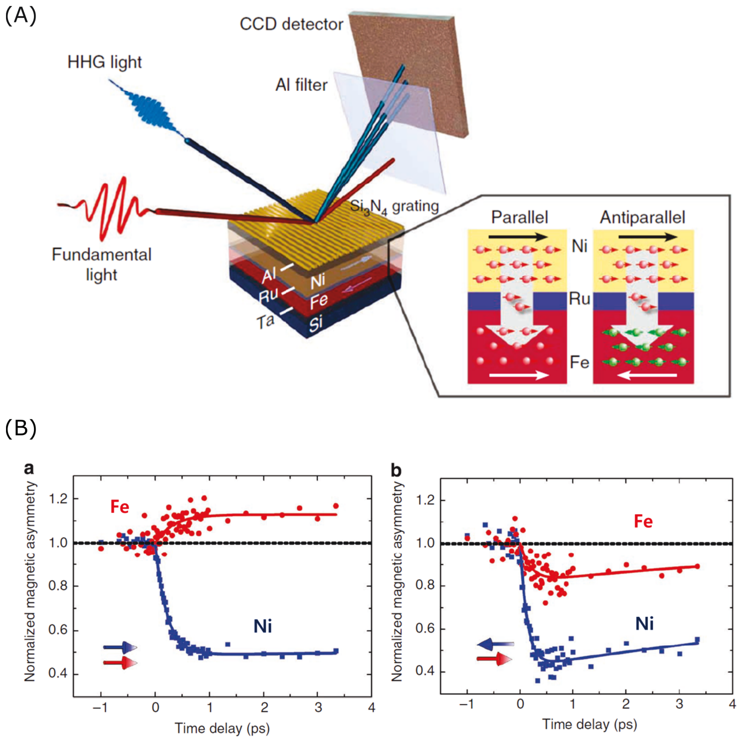

FIGURE 2.13: Element selective magnetization dynamics in Ni/Ru/Fe trilayer employing XUV light source by D. Rudolf [5]. (A) Experimental scheme for element selective magnetization dynamics of Ni/Ru/Fe with different magnetization alignment between Ni and Fe. (B) As response to optical excitation, **a**. the magnetization of the Fe layer is enhanced for parallel magnetization alignment due to superdiffusive spin transport from Ni layer. **b**. In contrast, the magnetizations in both Ni and Fe layers are quenched for antiparallel magnetization alignment.

observed extraction of terahertz spin currents from optically excited Fe/Ru and Fe/Au multilayers [47]. E. Turgut et al. confirmed that both super diffusive spin transport and spin-flip scattering are required to explain optically induced magnetization dynamics in a Ni/Fe multilayer system with various nonmagnetic interlayers between Ni and Fe films in 2013 [11].

Apart from the superdiffusive spin transport between layers in a multilayer system, a different representation of superdiffusive spin transport was observed by Graves et al. [14]. The authors experimentally confirmed the spin transport between adjacent magnetic nanoregions in inhomogeneous ferrimagnetic GdFeCo alloy. The alloy shows chemical and magnetic inhomogeneity on the nanoscale resulting in Fe- and Gd-rich nanoregions with antiparallel alignment of magnetic moments. By the optical excitation with the same pulse laser, both Fe- and Gd-rich regions are initially demagnetized. After about

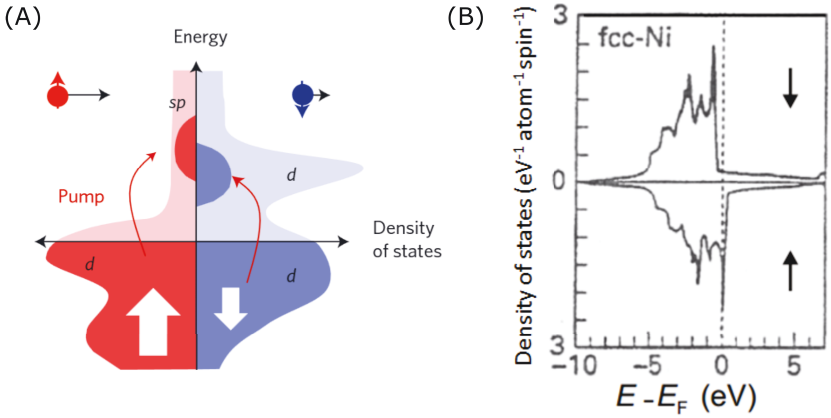

FIGURE 2.14: Density of states for ferrromagnetic 3d transition metals (A) Density of states for both majority (red) and minority (blue) electrons in 3d transition metal with the energy shift is shown. Most of the 3d-states are occupied by the hot majority spin electrons, the majority electrons in the 3d-states are thus excited into 4sp-states. In contrast, the excited hot minority-spin electrons are still in the 3d-states. (B) Density of states for spin-up and -down electrons of fcc-Ni [19]

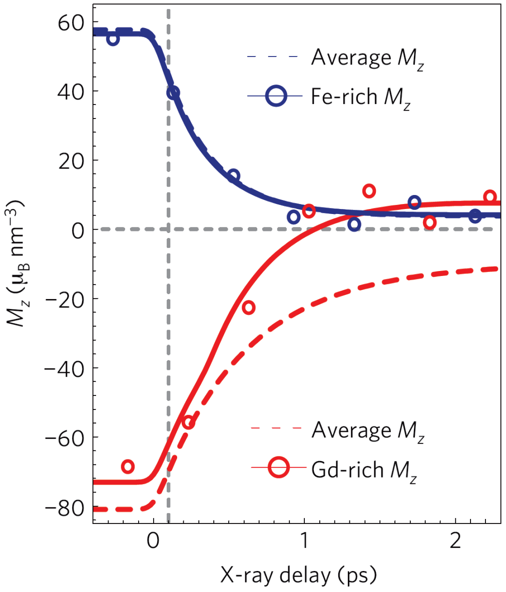

FIGURE 2.15: Initially magnetizations of Fe-rich and Gd-rich region are quenched by optical excitation and the Gd-rich region shows reversed magnetization after about one picosecond [14].

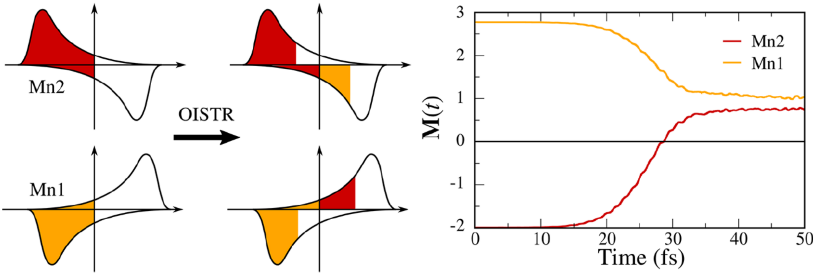

FIGURE 2.16: Magnetization switching of Mn layers in Mn(2ML)/Co(4ML)/Cu(001) multilayers by optical excitation. Upper Mn layer (Mn1) and bottom Mn layer (Mn2) have initially antiferromagnetic (AFM) order and Co layers have parallel magnetization direction with that of Mn1. Optical excitation changes the AFM magnetic order of Mn layers into transient FM state as a consequence of magnetization switching in Mn2 layer. The change of magnetization takes place via optically-induced intersite spin transfer (OISTR) that charge with majority spin states of Mn1 excites into minority states of Mn2 and vice versa [17].

1 picosecond, the magnetization of the Gd-rich region is reversed by angular momentum transfer from the Fe-rich region, which turned out to act as spin source.

2.3.3 Optically-induced Intersite Spin Transfer

In 2018, Dewhurst et al. introduced another mechanism for optically induced change in the magnetic structure including magnetization switching from antiferromagnetic(AFM) to ferromagnetic(FM) in multilayers and alloy systems based on density functional theory (DFT) for ground-state magnetic order and time-dependent DFT (TD-DFT) [17]. The Figure 2.16 shows optically-induced magnetization switching in multilayer system which consists of 2 monolayers (ML) of Mn and 4 ML of Co on Cu(001) substrate. All the Mn and Co layers have in-plane magnetization direction. In the initial states, upper Mn layer referred to as Mn1 and bottom Mn layer as Mn2 have AFM magnetic order, and the magnetization of the Co layers are parallel to that of Mn1. After optical excitation by pump pulse with pulse duration of 25 fs and fluence of 16 mJ/cm^2, the AFM magnetic order of Mn layers becomes FM state by switching of Mn2 layer at around 29 fs. As authors in Ref. [17] explain, within the time scale below 40 fs, the magnetization dynamics is not governed by spin-orbit induced spin-flip scattering. The process is explained in terms of the optically-induced intersite spin transfer (OISTR). Here the majority spin charge excitation occurs from majority states of Mn2 to minority states of Mn1 and majority spin charge flows from majority states of Mn1 to minority states of Mn2. The OISTR also holds for bulk materials such as FePt with 33% Mn and CoPt with 33% Mn as main mechanism applied to the case of multilayers. Since the OISTR depends only on the optical excitation of charge between sublattices, the excitation by the pulse with shorter pulse duration and higher fluence might result in faster change of magnetization. The sample systems treated above belong to the range of magnetic materials with uncompensated AFM magnetic order. In the case of fully compensated AFM materials such as NiO, the materials will show symmetric demagnetization in both magnetization directions. For FM materials, optical excitation will bring a magnitude change of the local magnetic moment keeping its magnetic order.

It remains an open question whether similar physical pictures can be applied to homogeneous multicomponent alloys like $\mathrm{Ni}_x\mathrm{Pd}_{1-x}$ alloy assuming that the $\mathrm{Ni}_x\mathrm{Pd}_{1-x}$ alloy is homogeneous. Another possible way of spin angular momentum transfer in multicomponent alloys was proposed by Bar'yakhtar and collaborators, who predicted that an exchange interaction related spin relaxation could cause longitudinal spin dissipation of atomic moments leading to local spin currents between atoms [15],[16]. In the present study, the magnetization dynamics in $\mathrm{Ni}_x\mathrm{Pd}_{1-x}$ alloys is investigated to understand more about spin dynamics between the Ni- and Pd subsystems in homogeneous $\mathrm{Ni}_x\mathrm{Pd}_{1-x}$ alloys in Section 5.2.

2.4 Magneto-Optical Kerr Effect(MOKE)

An experimental technique based on the magneto-optical Kerr effect (MOKE) can be employed to measure the magnetic properties of ferromagnetic materials including the magnetic anisotropy. In our experiment, the transversal magneto-optical Kerr effect(T-MOKE) has been employed for the measurement of the magnetization dynamics in $\mathrm{Ni}_x\mathrm{Pd}_{1-x}$ alloys. This chapter gives an explanation of the theoretical origin of T-MOKE.

2.4.1 General Description

The magneto-optic effect is a phenomenon in which an electromagnetic wave (light) propagates through (or reflects from) a magnetic material in the presence of a magnetic field. The magnetic field could be externally applied or the medium has its own magnetization (as in case of ferromagnetic material). The presence of the magnetic field or the magnetization in the magnetic material brings a change in the permittivity tensor (dielectric tensor) ϵ of the material. Off-diagonal components of the permittivity tensor ϵ are related to both the Faraday effect and the Kerr effect. The change leads to a rotation of the polarization or a change of the intensity of the incident light. When the light transmits through the material, the polarization of the light rotates (Faraday rotation) as discovered by Michael Faraday in 1846[48]. When linearly polarized light reflects from a magnetic material's surface, the polarization and/or the intensity of the light changes. The effect is called magneto-optical Kerr effect (MOKE) discovered by John Kerr in 1877[49]. According to the magnetization direction of the material with respect to the plane of incidence and the material surface, the MOKE can be categorized into three different types as shown in Figure 2.17. In the polar-MOKE (P-MOKE) geometry, the magnetization direction of the sample is perpendicular to the sample surface and parallel to the plane of incidence. Almost normal incidence of the light on the sample surface is employed for a simple analysis. P-MOKE leads to the change in the polarization of the light upon reflection from an out-of-plane magnetized material. In the case of longitudinal MOKE (L-MOKE), the direction of magnetization is parallel to both the plane of incidence and the sample surface. In L-MOKE, the rotation of the polarization of the reflected light upon its reflection gives information about an in-plane magnetized material. In contrast to both L-MOKE and P-MOKE, a change of intensity is measured in the transversal-MOKE(T-MOKE) geometry. Here the magnetization is perpendicular to the plane of incidence and parallel to the sample surface. To detect T-MOKE, light with p-polarization parallel to the plane of incidence is employed. The incidence angle is close to 45 degree to enhance the magnetic asymmetry. However, the 45 degree of incidence angle is very close to the Brewster angle for XUV light leading to a low reflectivity of p-polarized light. Thus, long acquisition time is required for T-MOKE measurement. To measure the magnetization change of the material in T-MOKE geometry, the magnetic asymmetry A is determined from the reflected intensities with two opposite directions of the magnetization by applying external magnetic field. The magnetic asymmetry is given by:

$$A = \frac{I^{\uparrow} - I^{\downarrow}}{I^{\uparrow} + I^{\downarrow}} \tag{2.28}$$

where I indicates the reflected intensity, ↑ and ↓ indicate opposite directions of the magnetization in the sample. Both intensities can be defined as

$$I^{\uparrow\downarrow} = |r \pm k|^2 \tag{2.29}$$

where r indicates the Fresnel amplitude vector and k indicates the Kerr vector. The Kerr vector gives rise to a difference between the reflected intensities. For all the geometries, the change of MOKE is linearly proportional to the magnetization of the material.

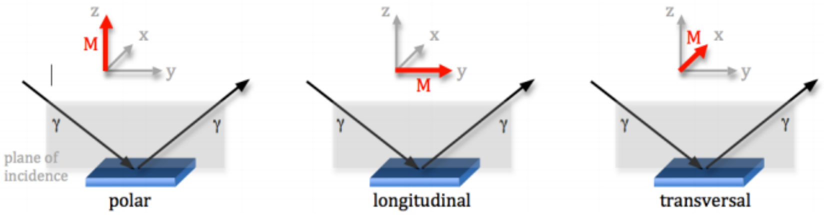

FIGURE 2.17: Three different geometries of MOKE. Red arrow in the inset indicates the direction of magnetization (Courtesy of Moritz Plötzing [50]).

2.4.2 Transversal MOKE (T-MOKE)

This chapter covers the theoretical description of the magneto-optic (MO) effects focusing on the transversal magneto-optical Kerr effect based on [51]. Magneto-optics describes the propagation of an electromagnetic wave in a magnetic material. The change of the light after its reflection from a magnetic material is a consequence of the Kerr effect and the propagation of the light can be expressed by Maxwell's equations. The Maxwell's equations for the interaction of the electric and magnetic fields in a material are given as:

$$\vec{\nabla} \cdot \vec{D} = 4\pi\rho \tag{2.30}$$

$$\vec{\nabla} \cdot \vec{B} = 0 \tag{2.31}$$

$$\vec{\nabla} \times \vec{H} = \frac{4\pi}{c}\vec{j} + \frac{1}{c}\frac{\partial \vec{D}}{\partial t} \tag{2.32}$$

$$\vec{\nabla} \times \vec{E} = -\frac{1}{c}\frac{\partial \vec{B}}{\partial t} \tag{2.33}$$

with $\vec{D}$ the electric displacement, $\vec{B}$ the magnetic induction, ρ the charge density and $\vec{j}$ the current density. The relations between the displacement field $\vec{D}$, the magnetic field $\vec{B}$ in a medium, the electric field $\vec{E}$, and the magnetic field $\vec{H}$ are expressed by materials equations:

$$\vec{D} = \vec{\epsilon} \cdot \vec{E} \tag{2.34}$$

$$\vec{B} = \vec{\mu} \cdot \vec{H} \tag{2.35}$$

and Ohm's law can be written as:

$$\vec{j} = \vec{\sigma} \cdot \vec{E} \tag{2.36}$$

where $\vec{\epsilon}$, $\vec{\mu}$, $\vec{\sigma}$ are the dielectric tensor, magnetic permeability tensor, and conductivity tensor. One solution of Maxwell's equations for monochromatic light in vacuum is a plane wave given by:

$$\vec{E}\,(\vec{r}, t) = \vec{E_0}\, e^{i\vec{k}\cdot\vec{r} - i\omega t} = \vec{E_0}\, e^{i\omega\vec{n}\cdot\vec{r}/c - i\omega t} \tag{2.37}$$

with the complex refractive index $\vec{n} \equiv c\,\vec{k}\,/\omega$. Maxwell's equations are continuity equations and are valid only if the wavelength of the light is much larger than the lattice constant. Then the material appears homogeneous with an averaged lattice constant. In our case, the highest energy limit of 72 eV from the HHG source corresponds to the shortest wavelength of 17.2 nm, which is much longer than the lattice constant. Thus, the dependence of the electric field on the wavevector $\left|\vec{k}\right| = \frac{2\pi}{\lambda}$ is negligible in our case. With this approximation, $\vec{\epsilon}$, $\vec{\mu}$, $\vec{\sigma}$ including all the field quantities depend only on the frequency ω. Thus, the electric displacement and Ohm's law in reciprocal space can be written by Fourier transform as:

$$\vec{D}\,(\vec{k}, \omega) \approx \vec{D}\,(\omega) = \vec{\epsilon}\,(\omega) \cdot \vec{E}\,(\omega) \tag{2.38}$$

$$\vec{j}\,(\vec{k}, \omega) \approx \vec{j}\,(\omega) = \vec{\sigma}\,(\omega) \cdot \vec{E}\,(\omega). \tag{2.39}$$

For a ferromagnetic material, the magnetic permeability tensor can be set as $\vec{\mu} = \mathbf{1}$, the unity matrix, in the macroscopic description, and therefore classical optics can be described by the relation between the dielectric tensor and the conductivity tensor given by:

$$\vec{\epsilon}\,(\omega) = \mathbf{1} + \frac{4\pi i}{\omega}\,\vec{\sigma}\,(\omega) \tag{2.40}$$

A combination of the time derivative of the Maxwell's equation 2.32 and the Equation 2.33 leads to the differential equation:

$$-\vec{\nabla}^2 \vec{E} + \vec{\nabla}\,(\vec{\nabla} \cdot \vec{E}) = -\frac{1}{c}\frac{\partial^2 \vec{D}}{\partial t^2} \tag{2.41}$$

By substituting the material equation for $\vec{D}$ and the electric wave field (Equation 2.37) in the medium into the equation above, the Fresnel equation:

$$[n^2\mathbf{1} - \overrightarrow{\epsilon} - \overrightarrow{n}{:}\overrightarrow{n}] \cdot \overrightarrow{E} = 0 \tag{2.42}$$

can be obtained, where $(\overrightarrow{n}{:}\overrightarrow{n})_{ij} = n_i n_j$ stands for the refractive index of vacuum$(n \approx 1)$ and the material in the T-MOKE case. The dielectric tensors of most materials are known, thus the refractive index $\overrightarrow{n}$ can be obtained from $det[n^2\mathbf{1} - \overrightarrow{\epsilon} - \overrightarrow{n}{:}\overrightarrow{n}] = 0$.

The dielectric tensor ϵ of a magnetized material has a particular form depending on the crystal symmetry and the magnetization direction with regard to the crystal axes. The magnetization in the material results in the occurrence of off-diagonal elements in the tensor ϵ. In the case of T-MOKE, an in-plane magnetized material has the dielectric tensor of the form:

$$\epsilon = \begin{pmatrix} \epsilon_{xx} & 0 & \epsilon_{xz} \\ 0 & \epsilon_{yy} & 0 \\ -\epsilon_{xz} & 0 & \epsilon_{zz} \end{pmatrix} \equiv \begin{pmatrix} \epsilon_1 & 0 & \epsilon_2 \\ 0 & \epsilon_1' & 0 \\ -\epsilon_2 & 0 & \epsilon_1 \end{pmatrix}. \tag{2.43}$$

Here, the magnetization is parallel to the x-axis and the z-axis is normal to the sample surface. The consequence of the in-plane magnetization is the presence of off-diagonal elements in the tensor 2.43. The off-diagonal elements of the tensor have the same absolute value with opposite signs due to symmetry. These off-diagonal elements (magneto-optical constants) are linearly proportional to the transverse magnetization, which is perpendicular to the plane of incidence in first approximation[46]. The solutions of the Fresnel equation for T-MOKE are:

$$n_s^2 = \epsilon_1, n_p^2 = \epsilon_1 + \frac{\epsilon_2^2}{\epsilon_1} \tag{2.44}$$

where n_s and n_p are the refractive indices for s- and p-polarized light. n_s has no coupling with the magnetization, in contrast, n_p is coupled to the magnetization. This means that only the p-polarized light shows a magneto-optical effect in T-MOKE geometry, but there is no effect for s-polarization. The Fresnel coefficients can be used to describe the reflection and transmission of s- and p-polarized light. The magnetic Fresnel reflection coefficients are:

$$\overleftrightarrow{r} = \begin{pmatrix} r_{ss} & r_{sp} \\ r_{ps} & r_{pp} + \Delta r_{pp} \end{pmatrix}. \tag{2.45}$$

For the transverse magnetization, the two reflection coefficients of p-polarized light for two opposite orientations of the magnetization are given by:

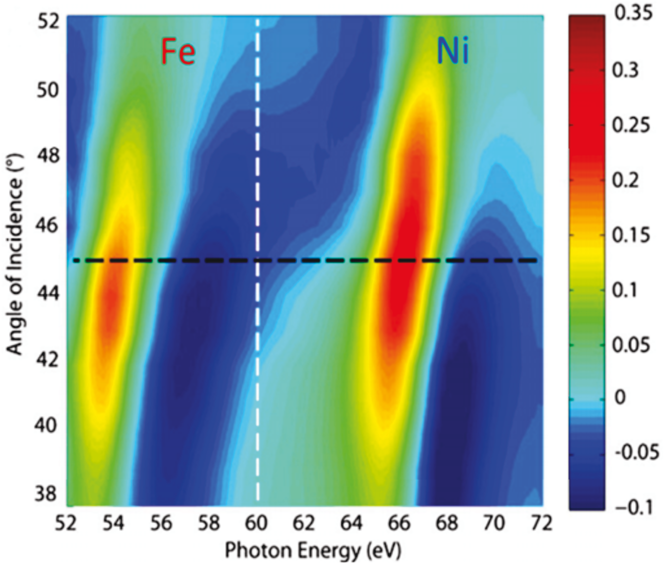

Figure 2.18: Magnetic asymmetry of a Permalloy sample as a function of the incidence angle and photon energy. The magnetic asymmetry is enhanced at the absorption edge of the element [46].

$$r_{pp}(M^{\pm}) \approx \bar{r}_{pp}\left[1 \pm \frac{\epsilon_0\epsilon_2 sin2\phi_i}{\epsilon_1^2 cos^2\phi_i - \epsilon_0\epsilon_1 + \epsilon_0^2 sin^2\phi_i}\right] \tag{2.46}$$

where $\bar{r}_{pp}$ is the non-magnetic reflection coefficient of p-polarization with the assumption of $\epsilon_1' \approx \epsilon_1$, and ϵ_0 is the vacuum permittivity. For the T-MOKE case, the cross-mode reflection coefficients are zero, $r_{sp} = r_{ps} = 0$ and $\Delta r_{pp} \neq 0$. With the fact that the reflected intensity is proportional to the square of the absolute value of the reflectivity, the magnetic asymmetry can be defined as

$$A = \frac{|r_{pp}(M^+)|^2 - |r_{pp}(M^-)|^2}{|r_{pp}(M^+)|^2 + |r_{pp}(M^-)|^2} = Re\left[\frac{2\epsilon_0\epsilon_2 sin(2\phi_i)}{\epsilon_1^2 cos^2(\phi_i) - \epsilon_0\epsilon_1 + \epsilon_0^2 sin^2(\phi_i)}\right]. \tag{2.47}$$

As given in Equation 2.47, the magnetic asymmetry for T-MOKE depends on the incident angle ϕ_i of the light and the magneto-optical constants. The magneto-optical constants also depend on the wavelength of the incident light and show resonant enhancement at the absorption edges of the involved elements in the material[46]. Experimental data for the incident angle dependence of the magnetic asymmetry enhanced at the absorption edges of the involved elements is shown in Figure 2.18.

2.5 Laser-Based High-Order Harmonics Generation

As explained above, in order to measure magnetization dynamics of magnetic materials with element selectivity in sub-picosecond scale, an ultrafast source of light from extreme ultraviolet (XUV) to soft X-ray spectral range is needed. There are several approaches to achieve short pulse duration and high energy from XUV to X-ray regime.

A first approach is to change the time structure of electron bunches in large scale facilities such as synchrotron and free-electron laser (FEL). A laser-induced energy modulation, the so-called femtoslicing [52], is one example, which generates X-ray pulses with sub-100 fs pulse duration with tunable energy and polarization. This technique can be achieved by copropagating a strong femtosecond laser pulse and electron bunch in an undulator, which is a periodic structure of magnets. Using femtoslicing, the time-resolved magnetization dynamics were performed at synchrotron facilities [12]. Another example for time-resolved measurements is using free electron lasers(FELs) [53].

Another approach for ultrashort light pulses is to convert fs laser pulses to higher photon energy by high harmonic generation (HHG) [54]. XUV sources by laser-based HHG can be produced on the table-top scale. Each source has its own properties, such as the achievable shortest pulse duration and the photon flux. The pulse duration from laser-based high harmonic sources is typically on very short time scales from femtoseconds down to attoseconds compared to FELs and the synchrotron femtoslicing [50]. A femtosecond pulse laser should be employed to generate the XUV radiation in energy range of 10 eV to 120 eV with much shorter pulse duration than that of the driving laser pulse. This chapter provides insight into the HHG process and properties of the generated XUV radiation based upon Ref. [55].

High-order harmonics of laser light can be generated during nonlinear interaction between the electric field of an intense laser pulse and a conversion medium. The process gives rise to laser light conversion into integer multiples of the fundamental frequency. Electrons of the conversion medium are first ionized by the intense electric field of the laser pulse. After the ionization, the electrons are considered as free electrons and they are accelerated away from the atomic core by the electric field of the laser in the first quarter of an optical period and slow down. During the second quarter of the period, the electrons approach the parent ions again and gain considerable kinetic energy, which exceeds the fundamental photon energy. The electrons may recombine with the parent ions resulting in emission of high-order harmonics. This process modelled by the so-called 'three-step model' describes the ionization of atom, propagation of electrons in the electric field, and recombination of the electrons with the parent ions emitting radiation in the XUV spectral range. Figure 2.20 shows the spectrum of the generated harmonics. In the 'perturbative' regime, the intensity of the harmonics decreases exponentially for low harmonic orders as expected from perturbation theory. In the 'plateau'

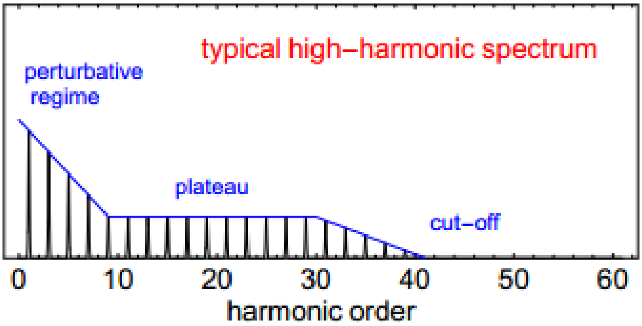

FIGURE 2.19: Typical spectrum of high-order harmonics. The harmonic spectrum as a function of the harmonic order displays three different regimes according to intensity distribution. In the perturbative regime, the intensity of the harmonics is rapidly decreasing for low harmonic orders. After the intensity decrease, the intensity stays almost constant with the increasing harmonic order in wide energy range, so called plateau regime, and the harmonics vanishes at the cut-off [56].

region, the intensity of the harmonics remains constant and the harmonics finally decay at the 'cut-off' energy.

2.5.1 Three-Step Model

XUV light can be generated by focusing an intense laser pulse into a waveguide filled with noble gas. In our experiment, the laser with 780 nm central wavelength and about 40 femtosecond pulse duration was employed. Neon gas was used as conversion medium and confined in a narrow glass capillary. As a consequence of the HHG process, XUV light in the energy range from 20 to 72 eV is obtained. In this section, the process of the HHG with three different steps (ionization, acceleration and recombination), so called 'three-step model', is described in detail.

The high harmonics are generated from the interaction between the electric field of an intense laser pulse and electrons in a spherical potential. In order to describe the process, one can start with ionization of an electron bound in the core potential of an atomic medium (see step 1 in Figure 2.20). Due to the electromagnetic field of the laser light, the core potential becomes time-dependent and will be distorted significantly giving rise to a reduced potential barrier. The electron is ionized by tunneling through the lowered barrier. Here, the core potential V can be described as sum of the potentials due to the electric field of the laser, $e\,\vec{E}\,(t)\,\vec{r}$, and the Coulomb potential of the ion as follows:

$$V(\vec{r},t) = -\frac{e^2}{4\pi\epsilon_0 r} + e\,\vec{E}\,(t)\,\vec{r}, \tag{2.48}$$

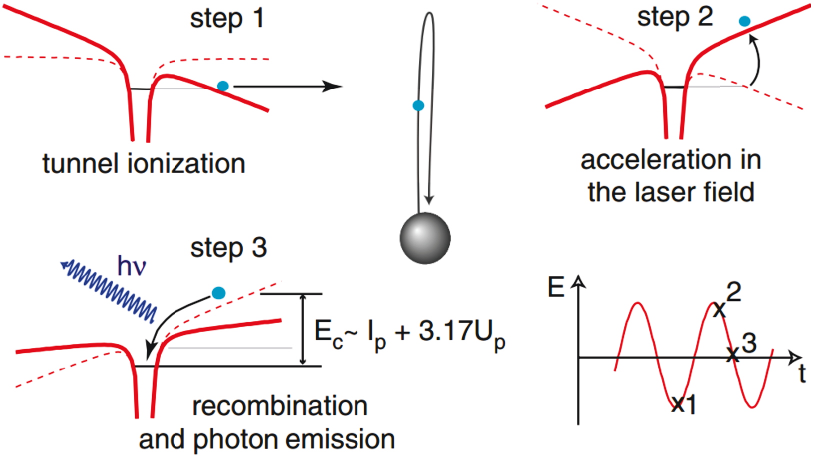

FIGURE 2.20: Three-step model for high-order harmonic generation. First, the core potential of the noble gas atom is distorted by the electric field of the intense laser pulse and the electron is ionized by tunneling (step 1). The ionized electron is then accelerated and gains kinetic energy by the electric field of the laser pulse (step 2). Afterwards, the electron recombines with the parent ionized atom while emitting the photon with an energy, which is sum of the ionization energy of the noble gas and the kinetic energy of the electron (step 3) [55].

where $\vec{r}$ stands for the relative distance of the electron from the atomic nucleus, and e is the electron charge. After the ionization, the ionized electron is considered as free electron and the motion of the electron is driven by the electric field, $E(t) = E_0 cos(\omega t + \varphi)$, of the laser. Here, E_0 is the amplitude of the electric field, ω the laser frequency and φ an arbitrary phase of the electric field at the time of the ionization. The time dependent position $x(t)$ of the ionized electron in the electric field can be expressed as:

$$x(t) = \frac{eE_0}{m_e \omega^2}(cos(\omega t + \varphi) - cos(\varphi)) + sin(\varphi)t. \tag{2.49}$$

where e is the electron charge and m_e is the electron mass. By considering the time derivative of the Equation 2.49 and the electron kinetic energy $E_{kin} = mv^2/2$, the ponderomotive potential, which is the cycle-averaged energy of the electron with a harmonic motion in the intense sinusoidal electric field, can be determined as:

$$U_p = \frac{e^2 E_0^2}{4 m_e \omega^2}. \tag{2.50}$$

The maximum kinetic energy of the electron by the ponderomotive potential, U_p, of the laser pulse can be obtained as $8U_p$[57].

The ionization of the electron can happen in two different regimes, multiphoton ionization or tunnel ionization, according to the 'Keldysh parameter' defined as:

$$\gamma = \sqrt{\frac{I_p}{2U_p}} \tag{2.51}$$

where I_p and U_p represent the ionization potential energy and the ponderomotive potential of the laser light. By considering γ, the ionization regime can be determined as the tunnel ionization for $\gamma << 1$ or the multiphoton ionization for $\gamma >> 1$.

After ionization and acceleration of the electron in the electric field, the electron recombines with an atomic level emitting a high harmonic photon with an energy which is the sum of the kinetic energy of the electron, E_{kin}, obtained from the laser field and the ionization potential, I_p:

$$\hbar\omega_{HHG} = E_{kin} + I_p \tag{2.52}$$

The HHG process from the ionization to recombination happens twice in every optical cycle of the laser field leading to a separation of the harmonics, $\Delta f = 2\omega$ in the spectral distribution of the harmonics as revealed by Fourier transform.

At $x = 0$ from Equation 2.49, the electron recombines with the parent ion. Here, the maximum photon energy can be determined by the maximum kinetic energy of the electron, which depends on the trajectory of the electron with varying phase, φ. By considering both the equation $x(t) = 0$ and the kinetic energy of the electron for various phases, $E_{kin}(\varphi)$, the maximum kinetic energy of the electron can be calculated as $3.17U_p$ at the phase of $18°$. Thus, the maximum energy of the high harmonic source referred to as 'cut-off' (see Figure 2.20) can be defined as:

$$\hbar\omega_c = 3.17U_p + I_p. \tag{2.53}$$

2.5.2 Phase-Matching

While the fundamental laser light propagates through the hollow capillary filled with noble gas, the photons with higher energies are generated along the capillary. For the efficient HHG, phases of the fundamental laser light and the XUV radiation should match and consequently both wavelengths should interfere constructively. Phase-matching between the fundamental laser and m-th harmonic order can be achieved by minimizing the wavevector mismatch defined as:

$$\Delta k = mk(\omega_f) - k(m\omega_f) \tag{2.54}$$

where ω_f indicates the fundamental laser frequency. The wavevector depends on the frequency and this dependence comes from several factors.
First, the refractive index of the neutral atomic gas used as conversion medium for HHG depends on ω by the dispersion, which brings a change Δk_{disp} in the wavevector. The wavevector depending on the refractive index can be written as:

$$k_{disp}(\omega) = (n(\omega) - 1)\frac{\omega}{c} \tag{2.55}$$

and the wavevector mismatch by the dispersion can be expressed by:

$$\Delta k_{disp}(\omega) = mk_{disp}(\omega_f) - k_{disp}(m\omega_f) = (n(\omega_f) - n(m\omega_f))\frac{m\omega_f}{c}. \tag{2.56}$$

The mismatch only depends on the difference of the refractive indices for the fundamental light and the m-th harmonic. The refractive index n for the fundamental light (780nm of the central wavelength) is generally larger than 1 (n>1), in contrast to the refractive index in the XUV regime, which is smaller than 1 (n<1). Therefore, the dispersion of neutral atomic gas, $\Delta k_{disp}(\omega) > 0$, is obtained.
Secondly, the majority of the ionized electrons by the electric field cannot recombine with the parent ion, but they compose a plasma, whose influence on the wavevector depending on ω is defined as:

$$k_{plasma}(\omega) = (n_{plasma}(\omega) - 1)\frac{\omega}{c} = -\frac{w_p^2}{2c\omega} \tag{2.57}$$

and the wavevector mismatch is given by:

$$\Delta k_{plasma}(\omega) = mk_{plasma}(\omega_f) - k_{plasma}(m\omega_f) = \frac{\omega_p^2(1 - m^2)}{2mc\omega_f}. \tag{2.58}$$

where

$$\omega_p = \sqrt{\frac{e^2 N_e}{\epsilon_0 m_e}} \tag{2.59}$$

ω_p denotes the plasma resonance frequency. According to the Equation 2.58 and the high harmonic order, $\Delta k_{plasma} < 0$ can be obtained.

The final factor for the wavevector mismatch, Δk_{geom}, is induced by the light focused and confined in the capillary. By solving Maxwell's equations with appropriate boundary conditions for the capillary waveguide, the solution is given as the series of the modes with wavevectors below:

$$k_{geom}(\omega) = \frac{u_{nl}^2 c}{2a^2\omega} \tag{2.60}$$

where a is the inner radius of the capillary, u_{nl} the l-th zero of the Bessel function $J_{n-1}(u_{nl}) = 0$. The wavevector mismatch by the capillary becomes:

$$\Delta k_{geom}(\omega) = m k_{geom}(\omega_f) - k_{geom}(m\omega_f) = \frac{u_{nl} c(1-m^2)}{2ma^2\omega_f}. \tag{2.61}$$

As in the case of the plasma dispersion, $\Delta k_{geom}(\omega) < 0$ is also obtained by the factor $(1-m^2)$ in Equation 2.61.

Finally, the total wavevector mismatch is defined as:

$$\Delta k = \Delta k_{disp} + \Delta k_{plasma} + \Delta k_{geom}. \tag{2.62}$$

Since Δk_{disp} has opposite sign with respect to Δk_{plasma} as well as Δk_{geom}, the phase matching can be achieved by tuning the plasma density (with the intensity and duration of the laser) and the density of the conversion medium.

Chapter 3

Sample Preparation and Characterization

3.1 Sample Fabrication

$Ni_xPd_{1\text{-}x}$ alloys form a solid solution over almost the entire range of Pd concentration and the alloys exhibit ferromagnetic properties up to 98% of Pd [58]. For the present studies we fabricated a range of $Ni_xPd_{1\text{-}x}$ thin films by molecular beam epitaxy (MBE) at a base pressure of $5x10^{-11}$ mbar. The film thickness of all films and for all stoichiometries was fixed at 20 nm. This thickness corresponds to the second maximum of the oscillatory reflectivity versus thickness curve for XUV light as calculated using the IMD software package [59]. The XUV light from the high-harmonic generation setup covers the energy range from 20 to 75 eV. For the present experiments we use photons in the energy range from 40 to 75 eV. The attenuation length of XUV light in this energy range in $Ni_{0.5}Pd_{0.5}$ was calculated using the CXRO software [60], and was found to lie between 7.8 to 8.5 nm, which is much shorter than the film thickness. Therefore, the influences of the film-substrate interface and the thickness dependence of the transverse Kerr effect are rather small and have not been taken into account in this study to keep the arguments as simple as possible. As Ni and Pd are in the same group of the Periodic Table, their isoelectronic properties allow for a homogeneous mixing as well as Curie temperature (T_C) tuning by varying the Ni-to-Pd mixing ratio in a broad range of temperatures, in this study from $T_C \sim 450$ K ($x \sim 0.5$) to $T_C \sim 630$ K ($x = 1.0$, pure nickel) [41]. Furthermore, Pd is easily polarizable and thus readily acquires a magnetic moment when exchange coupled to Ni [40]. The latter accounts for the fact that even though the Pd concentration can increase from 0 to 45%, the magnetic moment in the alloy at the same time decreases only by less than 10% [41].

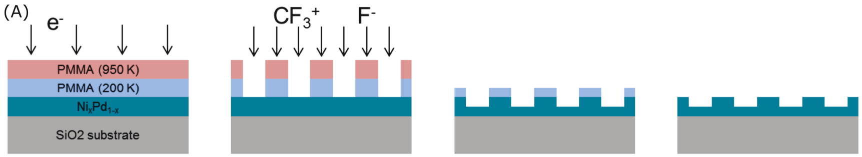

(a) Spin coating and e-beam lithography

(b) Development and CF_4 etching

(c) Lift-off

(d) Grating into sample

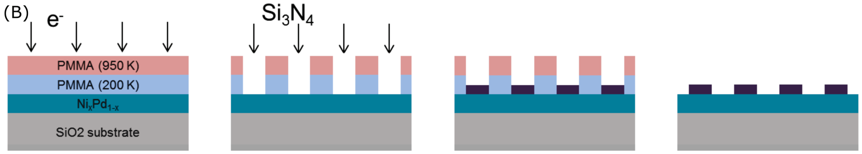

(a) Spin coating and e-beam lithography

(b) Development and Si_3N_4 coating

(c) Lift-off

(d) Si_3N_4 grating on sample

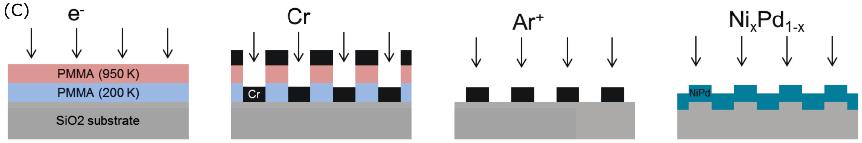

(a) Spin coating and e-beam lithography

(b) Development and Cr coating

(c) Lift-off and Ar etching

(d) Epitaxial growth on a grating substrate

FIGURE 3.1: Three different methods of Ni_xPd_{1-x} sample preparation with integrated grating (A) The grating sample is prepared by etching the sample surface. (B) A grating structure of Si_3N_4 is deposited on the flat sample surface. (C) The sample is deposited on the substrate patterned as grating.

In this study Ni_xPd_{1-x} thin film alloys with Pd concentration ranging from 0 to 50% have been examined using element-selective transversal MOKE (T-MOKE) measurements, probing excitations at the $N_{2,3}$-edges of Pd and the $M_{2,3}$-edges of Ni. For Pd concentrations exceeding 50% ($x < 0.5$), the magnetic moment of the alloys turns out-of-plane, thus making the T-MOKE measurements impossible due to the geometry requirements (see Chapter 4).

For an energy-resolved analysis of the light reflected from Ni_xPd_{1-x} alloys, an optical grating should be employed on top of the sample surface. In order to introduce a grating structure on the sample surface, electron beam (e-beam) lithography was employed. The details of the process are given below. The surface of the SiO_2/Si substrate or Ni_xPd_{1-x} thin film is first coated with electron beam resist by spin coating. The resist changes its solubility in a solvent when it is exposed to energetic electrons. In our case, two different types of resist are used, AR 649.04 (200 K) and AR 679.02 (950 K) from the company ALLRESIST. These resists consist of polymethyl methacrylate (PMMA) with different molecular weights and sensitivities. They both are positive type of resists, which becomes soluble when exposed to the e-beam. AR 649.04 (200 K) being more sensitive to e-beam is first coated on the sample surface with the speed of 300 rpm for

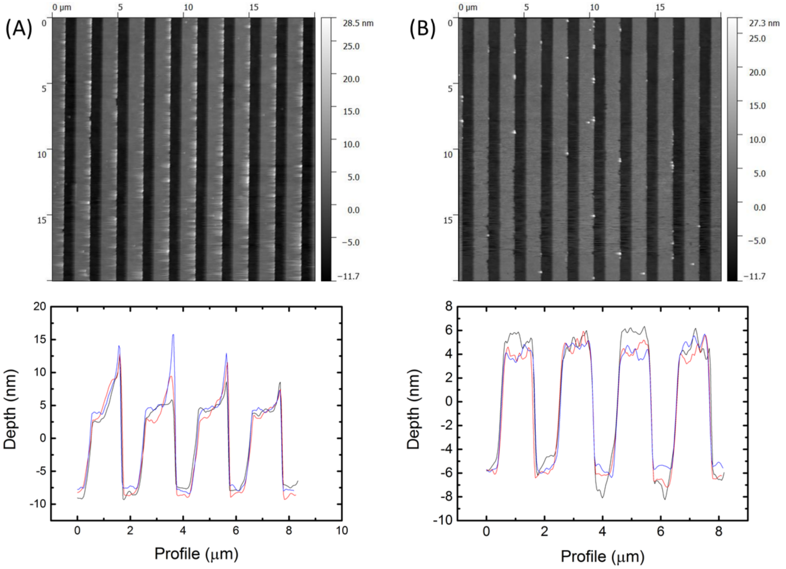

Figure 3.2: (A) AFM image of grating substrate on which PMMA is not completely removed (upper) and the grating surface shows fence-shape structures of PMMA at the edges of the grating (lower) (B) AFM image of grating after proper removal of PMMA (upper) and the grating surfaces show better quality without the fences (lower)

60 seconds, and baked at 180°C for 2 minutes for hardening the PMMA. Afterwards the less sensitive AR 679.02 (950 K) is coated on it and baked under the same condition. The resulting thicknesses of 200 K and 950 K PMMA would be between 150 to 200 nm and 70 to 100 nm, respectively. The grating pattern is written into the PMMA resist films by e-beam lithography and the exposed part becomes soluble. Because of the different sensitivities, larger part of 200 K PMMA is removed than from 950 K PMMA resulting in 'mushroom-like' cross section of the PMMA structure after development in the developer AR 600.55 from the company ALLRESIST.

Three different approaches to make the grating sample (see Figure 3.1) were composed to find the best quality. In the case of Figure 3.1 (A), we deposit the $\mathrm{Ni}_x\mathrm{Pd}_{1-x}$ alloy on the substrate and structure the PMMA grating as decribed above. The $\mathrm{Ni}_x\mathrm{Pd}_{1-x}$ with PMMA grating is etched in Tetrafluoromethane (CF_4) by reactive ion beam etching (RIBE). Then, the PMMA is removed by a lift-off method. The grating structure is thus fabricated into the sample surface.

In the case of Figure 3.1 (B), the PMMA grating is made on the sample, and Si_3N_4 is deposited on the PMMA grating and the $\mathrm{Ni}_x\mathrm{Pd}_{1-x}$ sample. The PMMA is removed by placing the sample into dimethylsulfoxide (DMSO) heated up to 70°C. Finally, the Si_3N_4 grating is structured on the sample.

The last approach is to etch a grating into the substrate and deposit the $\mathrm{Ni}_x\mathrm{Pd}_{1-x}$ thin film on the structured substrate (see in Figure 3.1 (C)). The process in Figure 3.1 (A) does not guarantee a high quality of the grating down into the substrate. To improve the quality, we added one more process, chromium lift-off. A Cr thin film with few nm thickness is placed on the substrate with the resist and the resist is removed by acetone. In consequence, we have a Cr grating on the flat substrate and etch the Cr grating. The depth can be controlled by considering the Cr thickness and etching ratio difference between Cr and SiO_2. The Cr coated substrate is etched by Ar ion beam etching. This process results in about 10 nm depth of the grating etched into the SiO_2 substrate and the sample reflects an acceptable spectrum at the end. All the fabricated substrates were investigated by AFM to check the quality of surface before the Ni_xPd_{1-x} thin films were deposited on the surface. Examples of the AFM images are given in Figure 3.2. The quality of the substrate depends on how well the PMMA is removed. If the PMMA is removed by just stirring the sample in acetone for a couple of minutes, the sample still has PMMA at the edge of the grating with 'fence' shape (see Figure 3.2 (A)). To remove the remaining PMMA, the surface was wiped by a piece of cotton with acetone leading to better surface quality (see Figure 3.2 (B)).

3.2 Longitudinal MOKE of Ni_xPd_{1-x} Alloys

To characterize the magnetic properties of Ni_xPd_{1-x} films we recorded magnetization hysteresis curves using longitudinal MOKE (L-MOKE) using a 780 nm laser, for pure Ni and three different Ni_xPd_{1-x} stoichiometries (x = 0.8, 0.7, and 0.5). The L-MOKE geometry is shown in Figure 2.17.

The L-MOKE measurements in Figure 3.3 reveal a clear in-plane component of the magnetization for the Ni_xPd_{1-x} alloys with x = 1.0, 0.8, and 0.7, with $H_C \sim 10$ mT. For x = 0.5 the magnetization saturates only at a much higher field of $H_C \sim 40$ mT and, in addition, the very gradual magnetization increase suggests a magnetization rotation along the increasing external field from the in-plane to slightly out-of-plane configuration. The rotation of magnetization could be interpreted as spin reorientation transition(SRT) due to the increasing contribution of Pd-mediated spin-orbit interaction in Ni_xPd_{1-x} alloys as discussed in the Section 2.2.

3.3 Sample Reflectivity

In order to measure the magnetic response of Ni_xPd_{1-x} alloys with element selectivity, employing a grating is essential to spatially separate the high harmonics by wavelength(energy) on a CCD detector. In our case, we employed a laminar grating on top

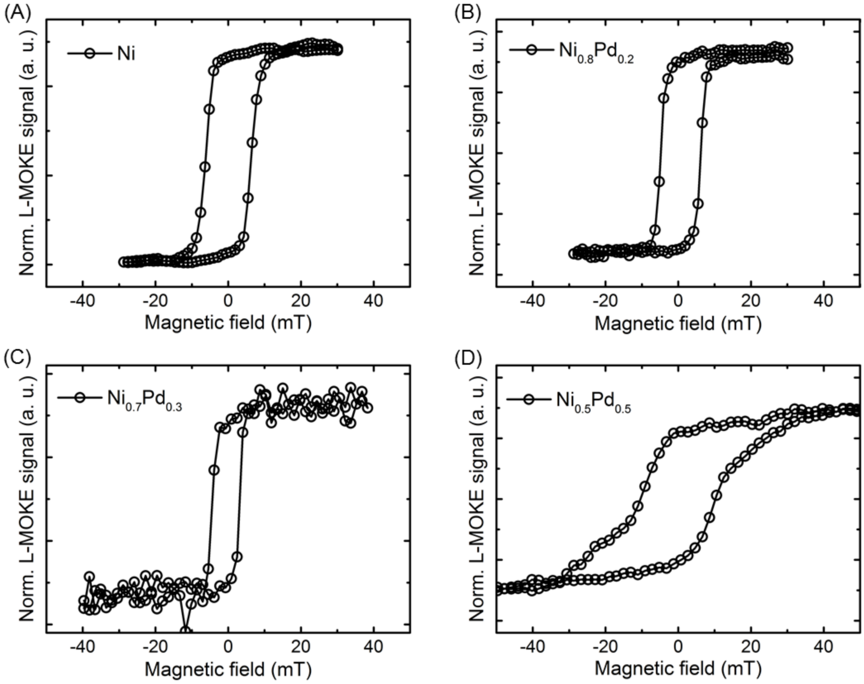

FIGURE 3.3: In-plane magnetization loops of (A) pure Ni and Ni_xPd_{1-x} with (B) $x = 0.8$, (C) $x = 0.7$, and (D) $x = 0.5$ measured using L-MOKE, indicating predominantly in-plane magnetization orientation for lower concentrations of Pd ((1-x)≤0.4)

of the sample surface and the incident angle of the XUV light on the grating sample is very close to the Brewster angle to enhance magnetic asymmetry from the samples [61]. This chapter describes the reflectivity of the samples, which depends on the grating depth and sample thickness.

3.3.1 Grating Reflectivity

In this study, a laminar grating onto the sample surface is employed for element-selective measurements and optimized for enhanced reflectivity of HHG at the absorption edges of the constituents (Ni, Pd) in Ni_xPd_{1-x} alloys. The reflectivity of the high harmonics depends on the geometrical parameters of the grating, such as the groove depth d, the line width a and the groove width b, which are shown in Figure 3.4. In our grating, the lines and grooves have same width, $a = b$, which determine the separation of the diffracted orders. To simplify our calculation, some approximations were adopted. First, the optical influence of the grating material is not considered. Second, the groove depth, d, is normally tens of nanometers and much smaller than the grating line width (a $\sim$

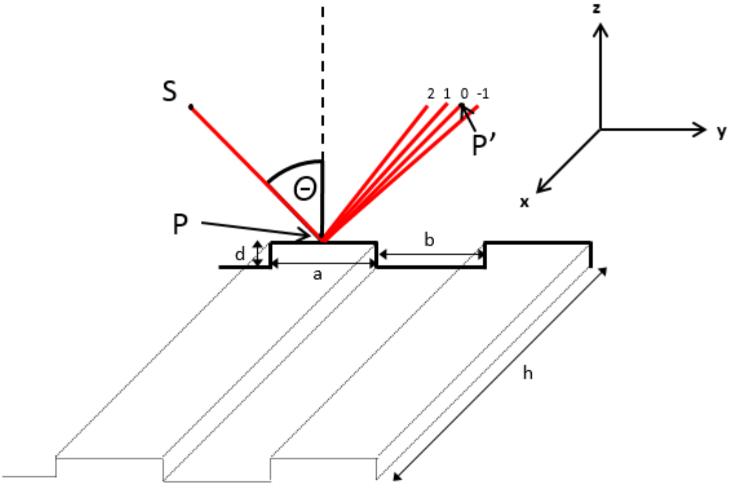

FIGURE 3.4: Laminar reflection grating. Geometrical parameters a, b, d and h indicate the line width, the groove width, the grating depth and the length of the lines. Θ is the incidence angle, which is about $\Theta \sim 45°$ in the measurement. S, P(x,y), P'(x',y') indicate the source of the light, the position on the grating and the position on the detector. The numbers above the reflected lights are the orders of diffraction [62],[63].

1um), i.e. d $\ll$ a. The loss of intensity by the reflection of the XUV light on the side wall of the groove is therefore not considered. Finally, for instance, at normal groove depth of about 20 nm and incidence angle of 45°, the optical path difference between pulses reflected on the upper lines and lower lines is 56.6 nm. With the relatively long difference in the optical path, the interference between pulses reflected from upper- and lower lines of the grating can be neglected, since the pulse duration of high-harmonic pulses is in the range of tens of femtoseconds. In Ref. [64], the reflection from the laminar grating is considered to be a combination of two gratings, which consist of the surfaces of the upper lines and grooves, respectively. After reflection of the light from the laminar grating, the intensity distribution is described by Kirchhoff's diffraction law [65]. We start the interference of two light beams reflected from adjacent surfaces of a line and a groove by considering the surfaces as two single slits. Here we assign the cordinates (x', y', z') and $(x^{"}, y^{"}, z^{"})$ for the upper single slit and lower single slit given by:

$$x^{"} = x', y^{"} = y' - a, z^{"} = z' + d. \tag{3.1}$$

The aperture size A of the both slits can be neglected in the Fraunhofer far field approximation due to the enormous difference between 2 μm of the grating spacing and about L = 50 cm of the distance between the sample and the detector satisfying the far field condition, $A^2/L\lambda \ll 1$. The reflected intensity amplitude ψ can be defined by a sum of the solutions for the both slits.

$$\begin{aligned}\psi = -\frac{-ikcos(\Theta)}{2\pi}\cdot(&\frac{e^{ik(L_0^{'}+L^{'}+(x^{'2}+y^{'2})/2L^{'})}}{L_0^{'}\cdot L^{'}}\int_{-h/2}^{h/2}\int_{-a/2}^{a/2}e^{ik\Phi(\xi^{'},\eta^{'},z^{'})}d\xi^{'}d\eta^{'}+\\ &\frac{e^{ik(L_0^{"}+L^{"}+(x^{'2}+y^{'2})/2L^{"})}}{L_0^{"}\cdot L^{"}}\int_{-h/2}^{h/2}\int_{-a/2}^{a/2}e^{ik\Phi(\xi^{"},\eta^{"},z^{"})d\xi^{"}d\eta^{"}})\end{aligned} \tag{3.2}$$

where k is the wavevector of the incoming light, Θ the incidence angle and $\Phi(x,y,z)$ the distance of the light on the grating from its source. Because the cordinates (x', y') are already used for the position of the light on the detector, (ξ,η) are used as the integration variables instead of (x,y). The distances $L_0^{'}$ and $L^{'}$ indicate the distance from the upper slit $P(x,y)$ to the source S and the detector $P'(x',y')$ respectively. The distances $L_0^{"}$ and $L^{"}$ are counterparts of $L_0^{'}$ and $L^{'}$ for the lower slit.

The solution of the integration of the amplitude ψ and intensity $I = |\psi|^2$ by considering N pairs of slits over the surface of the grating gives the intensity distribution written as:

$$\begin{aligned}I(\phi) = I_0\cdot&\overbrace{\frac{sin^2\left(\frac{a\cdot k(sin(\theta-\phi)-sin(\theta))}{2}\right)}{\left(\frac{a\cdot k(sin(\theta-\phi)-sin(\theta))}{2}\right)^2}}^{f_{slit}}\cdot\overbrace{\frac{sin^2(N\cdot(sin(\theta-\phi)-sin(\phi)}{sin^2(a\cdot(sin(\theta-\phi)-sin(\phi)))}}^{f_N}\\ &\underbrace{\cdot\, cos^2\left(\frac{\pi}{\lambda}(d(cos(\theta-\phi)+cos(\theta))-a(sin(\theta-\phi)-sin(\theta)))\right)}_{f_{geo}(a,d)}\end{aligned} \tag{3.3}$$

under the consideration that the distances from the gratings to the source and the detector are much larger than grating width a and depth d.

From the Equation 3.3, the factor f_{geo}(a,d) is introduced as the geometrical grating efficiency. The geometrical grating efficiency for our experiments can be calculated with given parameters from the experimental and the sample system, such as the grating line width a = 1 μm (500 lines/mm), and the incidence angle $\theta = 45°$. The wavelength of the XUV was chosen as 21.02 nm, corresponding to 59 eV which is the average value of the Ni $M_{2,3}$-edge near 68 eV and the Pd N_2-edge around 51 eV. The diffraction angle ϕ can be calculated by

$$d(sin\theta_m + sin\theta_i) = m\lambda \tag{3.4}$$

where d is the distance between adjacent grooves ($d = 2a$), θ_i is the incidence angle, θ_m indicates the angles, where the maximum intensities are found after diffraction, and m

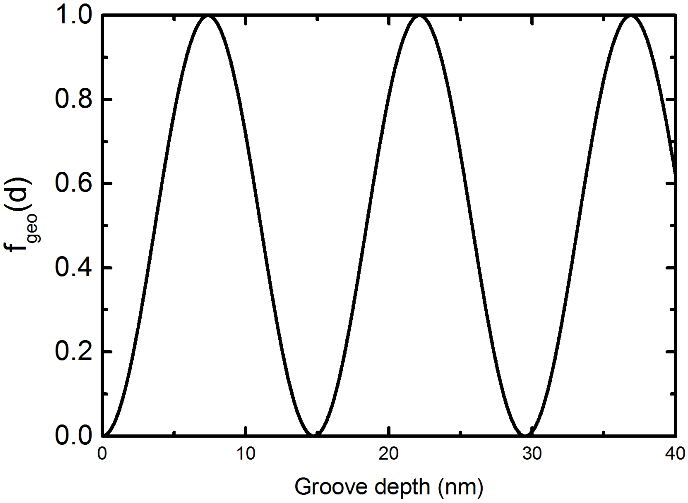

Figure 3.5: The groove depth-dependent grating efficiency f_{geo}. The maximum efficiencies are observed from 7.375 nm with 14.755 nm of periodicity.

is the order of diffraction. By considering the given condition and the Equation 3.4, the calculated θ_m for the first diffraction order (m=1) is -44.1547°, which is used for the calculation of the grating depth, since the magnetic asymmetry was measured from the first order diffraction.

With the values given above, the groove depth-dependent grating efficiency was calculated to get the optimal groove depth as shown in Figure 3.5. The grating reflectivity efficiency shows periodic minima and maxima with 14.755 nm of the periodicity. In the Figure 3.5, the first and second maxima are at 7.375 nm and 22.13 nm.

In addition, the energy-dependent reflectivity of HHG from the grating sample is calculated by considering a grating depth d = 10 nm, a grating line width $a = 1\mu$m, an incidence angle $\theta = 45°$, and an angle deviation by diffraction ϕ in Figure 3.6. The reflectivity shows higher values at the lower energy range. We note that the reflectivity optimization serves solely to increase the signal-to-noise ratio and does not affect the magnetic asymmetry.

3.3.2 Thin-Film Reflectivity

Ni_xPd_{1-x} alloy samples were prepared on the grating substrate as thin films, which brings interference of beams reflected on the sample surface and the interface of the

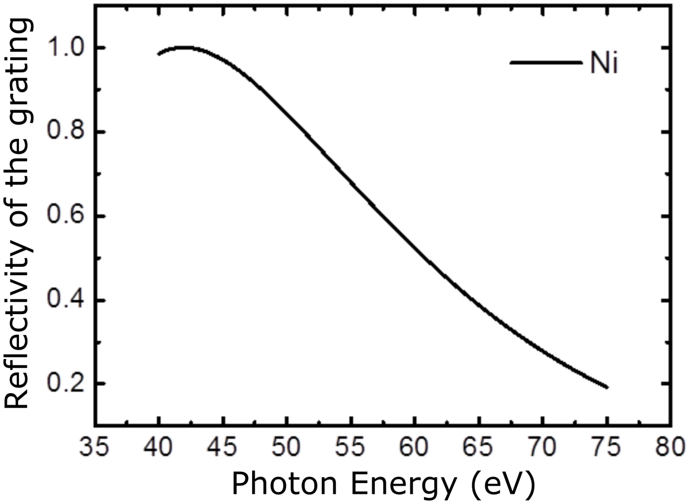

Figure 3.6: Energy-dependent reflectivity of the laminar grating after reflection in the energy range from 40 to 75 eV. Here, the grating depth $d = 10nm$, the grating line width $a = 1\mu$m were chosen for the calculation using f_{geo} from Equation 3.3.

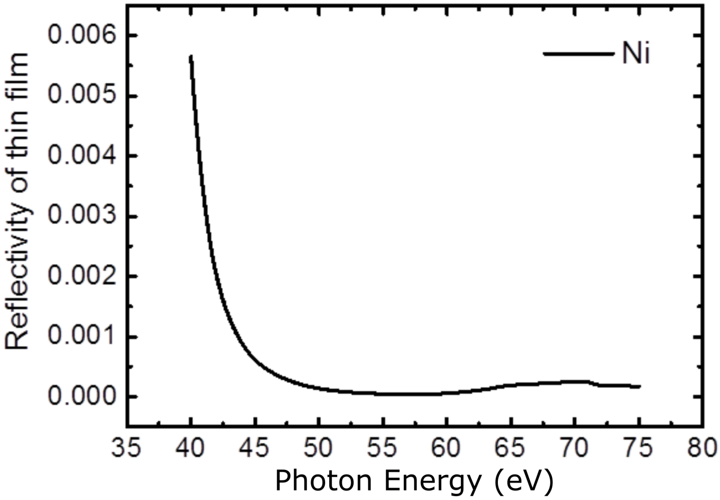

Figure 3.7: Energy dependent thin film reflectivity of the sample, Al(3 nm)/Ni(20 nm)/SiO$_2$, from 40 to 75 eV simulated using the software 'IMD_XOP'[59].

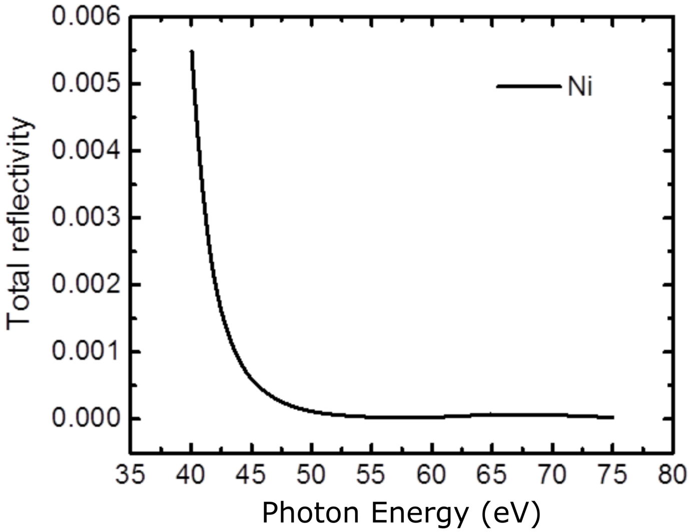

FIGURE 3.8: Total reflectivity of the sample obtained as a product of the grating reflectivity and the thin film reflectivity.

sample and substrate. The Ni_xPd_{1-x} film thickness is about 20 nm, which is even larger than the depth of the grating, thus we can also ignore the interference effect due to extremely short pulse duration as we assumed in the case of the grating reflectivity. Then we checked the energy-dependent reflectivity $R_{thinfilm}$ of the thin film within an energy range between 40 eV to 75 eV using the software 'IMD-XOP'[59]. In the Figure 3.7, the reflectivity of a thin film with 20 nm thickness is simulated and the reflectivity of the film at low photon energy is about two-order of magnitude higher than the reflectivity at high energy. The energy-dependent total reflectivity of the thin film samples on the grating substrate were deduced as:

$$\mathrm{R}_{total} = R_{grating} * R_{thinfilm} = f_{geo}(a, d) * R_{thinfilm} \tag{3.5}$$

which is a product of the reflected intensity from the grating geometry, $f_{geo}(a, d)$ from Equation 3.3, and the reflectivity of the thin film obtained from the software in Figure 3.7. The total reflectivity is most likely determined by the factor of the thin film rather than the grating (see Figure 3.8).

In addition, the XUV light from the high-harmonic generation setup covers an energy range from 20 to 72 eV. The attenuation length of such XUV light in $Ni_{0.5}Pd_{0.5}$ ranges from 7.8 to 8.5 nm, corresponding to the energy range from 40 to 75 eV, which is much

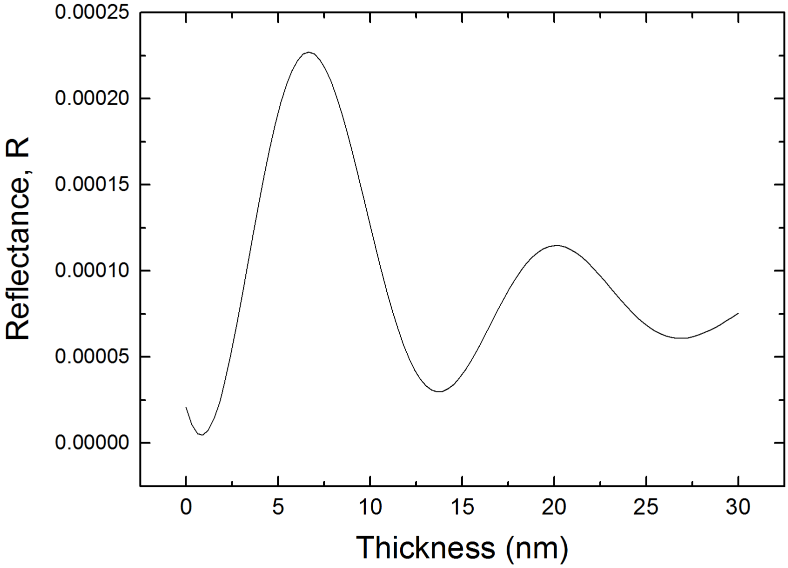

FIGURE 3.9: Thickness-dependent reflectivity of the XUV radiation with energy of 67 eV on a pure Ni thin film. The second highest reflectivity is expected around 20 nm of thickness, where effect of the interface and the thickness-dependence of the T-MOKE signal can be ignored.

less than the 20 nm of sample thickness (the calculation was done using CXRO software [60]). The 20 nm of film thickness was chosen from the thickness-dependent reflectivity of the XUV radiation with energy of 67 eV (see Figure 3.9). The influence of the interface and the thickness dependence of the transverse Kerr effect have therefore not been taken into account at this point, in order to keep the arguments simple.

Chapter 4

Experimental Setup

This chapter describes the experimental setup for the elemental-selective T-MOKE measurement. The setup consists of four different parts as shown in Figure 4.1. Ultrashort intense light pulses with a pulse duration on the femtosecond time scale can be generated from Ti:Sapphire laser systems coupled with chirped pulse amplification (CPA) (Figure 4.1 (A)). The XUV light is generated with the HHG process by focusing the laser into a capillary filled with noble gas (Figure 4.1 (B)). The XUV light is separated from the fundamental light by a Si wafer and Al filters. The beamline can be set in two different configurations, a pair of Bragg mirrors, which reflect a narrow spectral range or by a toroidal mirror, which reflects the entire spectrum (Figure 4.1 (C)). In order to measure the T-MOKE signal, external magnetic fields with opposite directions are applied. The

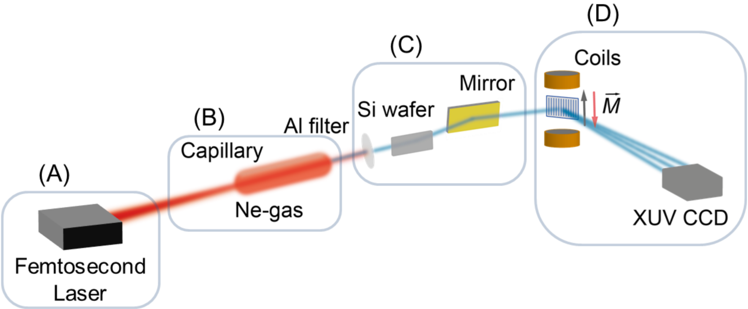

FIGURE 4.1: Schematic drawing of the experimental setup for T-MOKE measurement. (A) The laser system generates intense femtosecond pulses. (B) XUV light source is generated by focusing the laser into a capillary filled with noble gas. (C) The XUV light is separated from the fundamental beam by a Si wafer and Al filters, and focused on the $\mathrm{Ni}_x\mathrm{Pd}_{1-x}$ alloy sample by Bragg mirrors or a toroidal mirror. (D) A grating on the sample spatially expands the high harmonics after reflection and the harmonics are measured by a CCD camera. The T-MOKE signal is measured by applying magnetic fields in opposite directions.

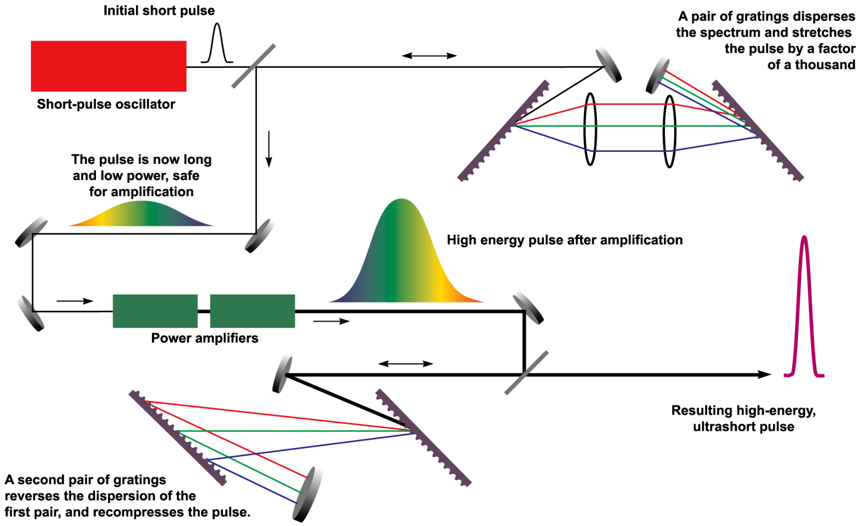

FIGURE 4.2: Scheme of the chirped pulse amplification (CPA) system using two pairs of gratings [66]. The first pair of the gratings stretches the seed laser to tens of picoseconds pulse duration. After stretching the pulses are amplified in the Ti:Sapphire crystal, which is optically pumped by the pump laser. Finally, the amplified laser pulses proceed to the compressor, which compensates the dispersion from the stretcher.

reflected XUV can be measured by a CCD camera (Figure 4.1 (D)). More details of the experimental setup are given in following sections.

4.1 Laser System

In this study, the ultrashort intense pulse laser employs a CPA system, which has been developed by the company KMLabs (see Figure 4.2)[1]. The laser system has three main parts, the oscillator (Griffin), the pump laser (Lee), and the multipass laser amplifier. The oscillator produces laser pulses by mode-locking within a titanium-doped-sapphire crystal. Such a system can generate nearly bandwidth-limited pulses with short pulse duration. The theoretical lower limit of the pulse duration can be attained by the time-bandwidth product (TBP) for a given spectral bandwidth. The TBP for a Gaussian pulse is defined as [67]

$$c/\lambda^2 \cdot \delta\lambda \cdot \delta\tau > 0.441 \tag{4.1}$$

---

[1] Figure of CPA is from `https://en.wikipedia.org/wiki/Chirped_pulse_amplification`

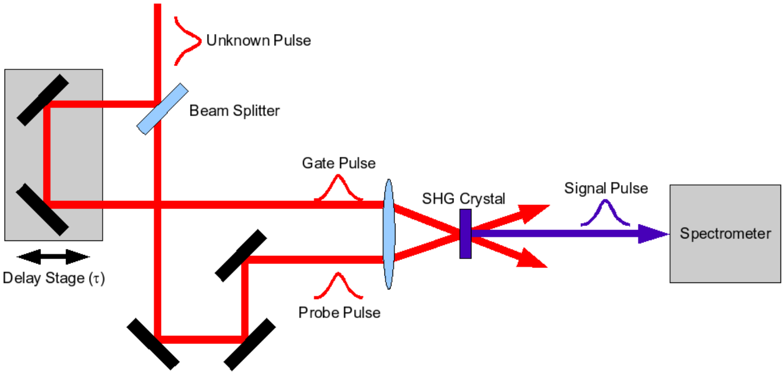

FIGURE 4.3: A schematic of the FROG setup using a SHG crystal and autocorrelation of the pulse with another identical pulse [64],[68].

With the central wavelength of the oscillator, $\lambda_G\sim$ 800 nm, and its bandwidth $\Delta\lambda_G\sim$ 60 nm, the lower limit of pulse duration is theoretically $\Delta\tau_{min,G}\sim$ 15.7 fs. The measured pulse duration is between 20 and 30 fs. The repetition rate, the average output power and the energy per pulse of the laser oscillator are 84 MHz, 180 mJ and 2.1 nJ respectively. The Griffin oscillator is also referred to as 'seed laser' providing pulses to the Dragon amplification system. The Dragon amplifier is a Ti:sapphire-based CPA system, which consists of two pairs of gratings : the stretcher and the compressor (see Figure 4.2). In the stretcher, the femtosecond seed pulses are temporally expanded to several tens of picoseconds to avoid the effect of peak power damage prior to amplification.

The repetition rate of the seed laser is about 84 MHz as measured by an oscilloscope. The repetition rate of the final output laser is controlled by a Pockels cell from 1 to 10 kHz. We normally used 3 kHz for the measurements. After the Pockels cell, the stretched pulse is amplified by a multipass amplification (see Appendix) through the Ti:Sapphire crystal, which is excited by the pump laser (pump power $>$ 50 W) causing population inversion in Ti:Sapphire (laser medium) and amplification of the seed laser. The Ti:Sapphire is the material with the broadest bandwidth leading to short pulse durations below 10 femtosecond compared to other solid-state lasers, e.g. Nd- or Yb-doped crystals (1 to 10 ps) or glasses (50 to 500 fs) [69],[70]. By placing a pick-up mirror in the 14th beam path, the amplified pulse is sent to the compressor. The compressor is designed to compensate the dispersion of the stretcher and to produce intense femtosecond pulses. The amplified laser has approximately 6 W of output power and 3 kHz repetition rate leading to 2 mJ of pulse energy.

The pulse duration of the Dragon amplifier output was checked by Frequency-Resolved Optical Gating (FROG, see Figure 4.3) [64],[68]. In a FROG measurement, the output pulse is separated into two identical pulses by a beam splitter. One of the pulses is

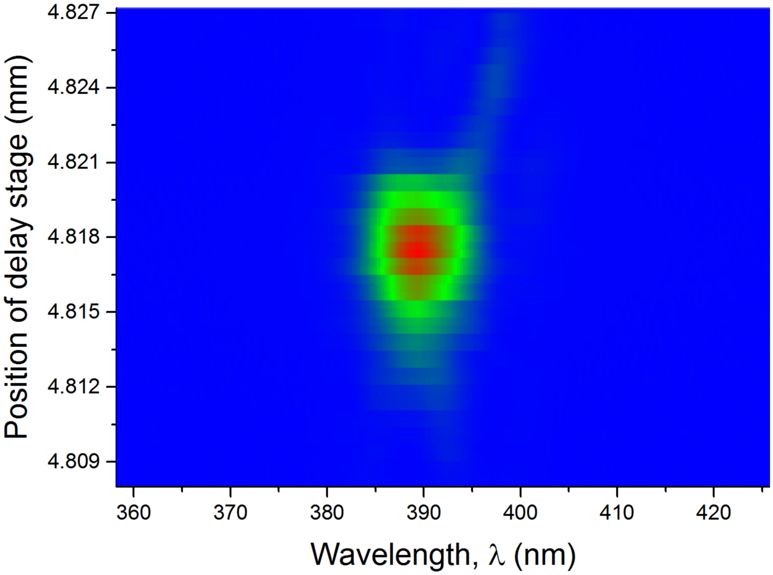

FIGURE 4.4: One of the results recorded by FROG. The Y-axis is the position of the delay stage (mm) indicating the time delay between pulses, and the x-axis is the wavelength. The FROG measurement provides information of the pulse duration and dispersion after compression.

reflected by mirrors on a delay stage to control the time difference between the pulses passing through a second harmonic generation (SHG) crystal. When the pulses are temporally overlapping on the SHG crystal, the crystal generates second harmonic radiation of the incoming pulse by a nonlinear sum frequency generation process. By measuring the spectrum of the harmonic signal, which is recorded in time- vs. wavelength graph with varying time delay between the pulses (Figure 4.4), we can deduce the pulse duration and dispersion after compression. Optimum alignment resulted in a pulse duration between 30 to 40 fs. The ultrashort pulse is split into two beam paths by a beam splitter, which reflects 90% of the output for the probe beam by HHG and transmits 10% for the pump beam.

4.2 XUV Beamline

4.2.1 Beam Stabilization System

The time required for spin dynamics measurements depends on how many demagnetization curves are measured and averaged. It takes normally a couple of hours to get one curve. Thus, the experimental system should have a stable laser pointing for hours,

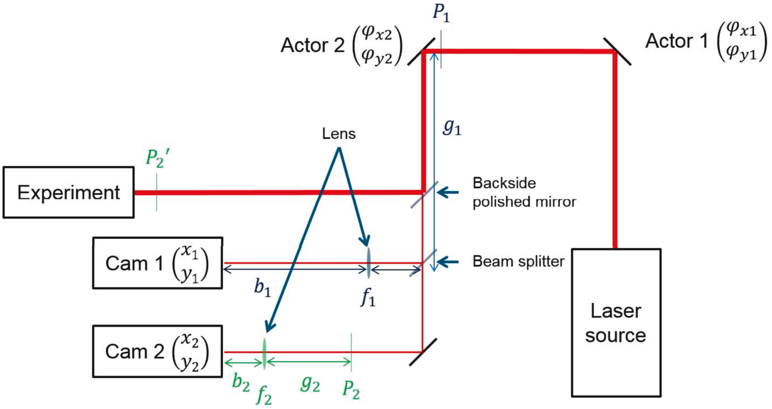

FIGURE 4.5: Beam stabilization system with two motorized mirrors, Actor1 and Actor2, and two cameras, Cam1 and Cam2 [64]. The laser beam with weak intensity passes through a backside polished dielectric mirror and the laser is monitored by the cameras. The Cam1 records the beam position on the Actor2 (marked as P_1) and the movements of the Actor2 do not make any change of the beam position on the Cam1. Similarly, Cam2 records the beam position at P_2. Since the distance between P_2 and the dielectric mirror is the same as the distance between the dielectric mirror and P_2' at the entrance of the capillary, Cam2 indirectly records the laser drift at the capillary (P_2).

which can be maintained by a beam stabilization system. The description of the beam stabilization system given in this section is mostly based on Ref.[64]. Laser propagation can move by two parameters, laser pointing and laser position, and each parameter can move in horizontal and vertical directions. Such movements of the laser beam are called drift. Thus, the laser propagation can be described by these four parameters, and the drift of the laser beam should be compensated by tuning the parameters. The beam stabilization system consists of two CCD cameras, which detect the beam position at two different positions in real time, and two motorized mirrors. These mirrors are also called actuators and Actor1 and Actor2 refer to these mirrors in the following. The actuators can steer the laser propagation direction in horizontal- and vertical directions by adjusting their angle ϕ_{ij}, where $i = x, y$ indicates the horizontal(x)- and vertical(y) direction and $j = 1, 2$ is for Actor1 and Actor2. Cam1 and Cam2 refer to the cameras for laser beam detection. The configuration of the system is shown in the Figure 4.5. To record the laser propagation direction by the cameras, a small part of the laser first passes through a backside-polished mirror with high reflectivity and a beam splitter. Then the laser is aligned and focused onto the cameras by focusing lenses. The beam position on the camera is defined by the center of mass algorithm:

$$\vec{R} = \frac{\sum_i^N m_i \cdot \vec{r_i}}{\sum_i^N m_i} \tag{4.2}$$

where m_i indicates the intensity (instead of mass) on pixel position $\vec{r_i}$ of the camera. The positions of the beam on the Cam1 and the Cam2 are assigned as (x_1, y_1) and (x_2, y_2). The focusing lenses are placed considering the lens equation given by:

$$\frac{1}{f} = \frac{1}{b} + \frac{1}{g} \tag{4.3}$$

where f is the focal length of the lens, b the image distance between the lens and the camera, and g the object distance between the lens and the object (P_1, P_2) (see Figure 4.5). Then the angles of the actuators and the beam position on the cameras can be defined as the following vectors:

$$\vec{\phi} = \begin{pmatrix} \phi_{x1} \\ \phi_{y1} \\ \phi_{x2} \\ \phi_{x1} \end{pmatrix}, \vec{r} = \begin{pmatrix} x_1 \\ y_1 \\ x_2 \\ y_2 \end{pmatrix}. \tag{4.4}$$

The angle of the actuators $\vec{\phi}$ and the position of the laser on the cameras $\vec{r}$ should be coupled using a transformation matrix T. The deviation of the laser propagation direction $\Delta \vec{r}$ can result in a corresponding angle change $\Delta \vec{\phi}$ by the relation:

$$\Delta \vec{\phi} = T \Delta \vec{r} \,. \tag{4.5}$$

The equation can be rewritten as:

$$\Delta \vec{r} = T^{-1} \Delta \vec{\phi} \,. \tag{4.6}$$

where T^{-1} can be determined as:

$$T^{-1} = \begin{pmatrix} t'_{11} & 0 & t'_{13} & 0 \\ 0 & t'_{22} & 0 & t'_{24} \\ t'_{31} & 0 & t'_{33} & 0 \\ 0 & t'_{42} & 0 & t'_{44} \end{pmatrix} \tag{4.7}$$

with the fact that the horizontal (vertical) axis of the actuator has no influence on the vertical (horizontal) axis. Then Cam1 and focusing lens should be properly placed considering the lens equation, consequently the Cam1 records the beam position on the

Actor2. As a result, Actor2 and Cam1 are decoupled, so that Actor2 does not have any effect on Cam1. The decoupling leads to the new expression of T^{-1} as:

$$T^{-1} \sim \begin{pmatrix} t'_{11} & 0 & 0 & 0 \\ 0 & t'_{22} & 0 & 0 \\ t'_{31} & 0 & t'_{33} & 0 \\ 0 & t'_{42} & 0 & t'_{44} \end{pmatrix}. \tag{4.8}$$

By inverting the Equation 4.8, T is given by:

$$T \sim \begin{pmatrix} t_{11} & 0 & 0 & 0 \\ 0 & t_{22} & 0 & 0 \\ t_{31} & 0 & t_{33} & 0 \\ 0 & t_{42} & 0 & t_{44} \end{pmatrix}. \tag{4.9}$$

By considering the Equation 4.5 and calculating T in Equation 4.8, the drift of the laser beam at the entrance of the capillary can be compensated by adjusting the angle of the actuators in real time.

4.2.2 XUV Light Source

As stated in Section 2.5, XUV light is generated by HHG. In the process, the intense ultrashort pulse laser is focused into a narrow capillary waveguide with 150 μm of inner diameter filled with noble gas (Ne or Ar). The laser is focused by a plano-convex lens, which reduces spherical aberration and has a focal length of 50 cm. The best focusing of the lens can be achieved by placing the curved surface of the lens oriented towards the laser source. The capillary is a part of a vacuum beamline to avoid the absorption of the XUV light in air. The laser beam is coupled into the beamline through a window placed under the Brewster angle with respect to the beam propagation to minimize the reflection of the laser light. Both sides of the capillary are evacuated to keep a pressure below 10^{-3} mbar inside the chamber. To reduce the loss of the Ne gas from the evacuation at both ends of the capillary and keep a uniform pressure of the gas in the capillary, the Ne gas is continuously filled through the small holes drilled in the sides of capillary, with constant tunable pressure using a flowmeter. Figure 4.6 shows the capillary waveguide during HHG operation with shining in orange color, which is characteristic for the plasma discharge in Ne gas.

XUV light resulting from the interaction of the laser pulse with Ne gas has the energy range from 20 to 72 eV covering the $M_{2,3}$-edges of the ferromagnetic materials and Pd

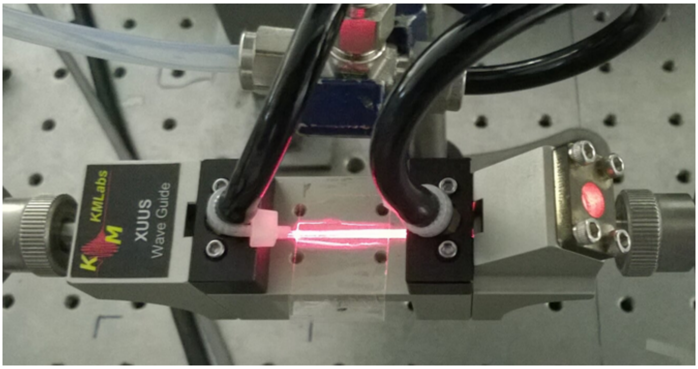

FIGURE 4.6: Capillary waveguide filled with the neon gas during high harmonic generation.

$N_{2,3}$-edge (see Table 4.2.2). The XUV source is employed for element-selective studies of $\mathrm{Ni}_x\mathrm{Pd}_{1-x}$ magnetic alloys using the T-MOKE geometry.

Element, absorption edge	Fe, $M_{2,3}$	Co, $M_{2,3}$	Ni, $M_{2,3}$	Pd, $N_{2,3}$
Energy	54 eV	60 eV	68 eV	51 eV

TABLE 4.1: Absorption edges of ferromagnetic elements and palladium within the energy range of the HHG source from Ne gas

4.2.3 Beamline Configurations

After the HHG stage, the fundamental light is filtered out from the high harmonics by reflection from a Si wafer plate and an Al filter. There are two different beamline geometries for pump-probe experiments in this study. (see Figure 4.7) First, monochromatized XUV light probes the magnetic response of a specific element of a sample by a pair of Bragg mirrors, which are specially fabricated to reflect in a narrow range of wavelengths. Second, a toroidal mirror, which has two different focal lengths, is employed to focus the entire spectrum of harmonics onto a grating sample and subsequently a CCD camera. This configuration enables us to measure magnetization dynamics of the involved elements with element selectivity by integrating an energy range in the spectra corresponding to the absorption edges of the elements. The example for magnetic asymmetries of $\mathrm{Ni}_{0.8}\mathrm{Pd}_{0.2}$ and pure Ni from the different configurations is shown in Figure 4.8.

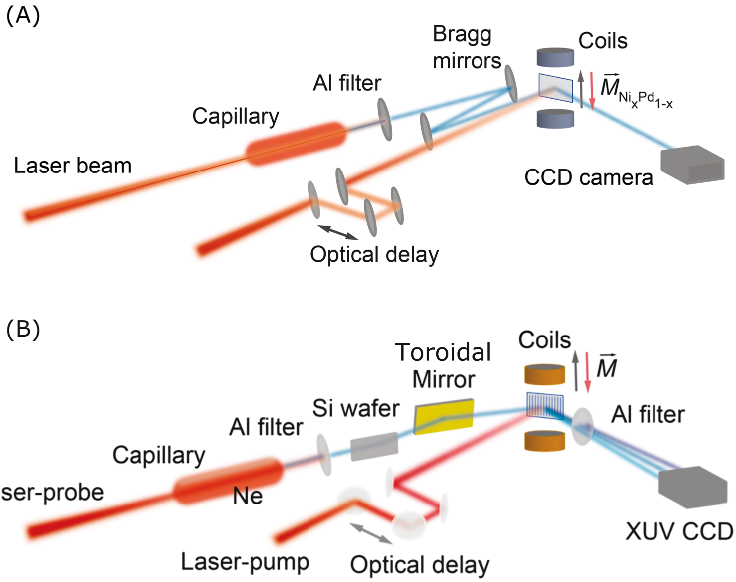

FIGURE 4.7: Two different T-MOKE configurations (A) A schematic of T-MOKE setup with a pair of Bragg mirrors. One is a curved mirror and the other one has a flat surface. Both mirrors are designed to reflect the same narrow energy range. One spot with Gaussian shape of XUV is recorded by the CCD. (B) A schematic of the T-MOKE setup with a toroidal mirror. All the high harmonics are focused on a grating sample and spectrum after reflection is recorded by CCD.

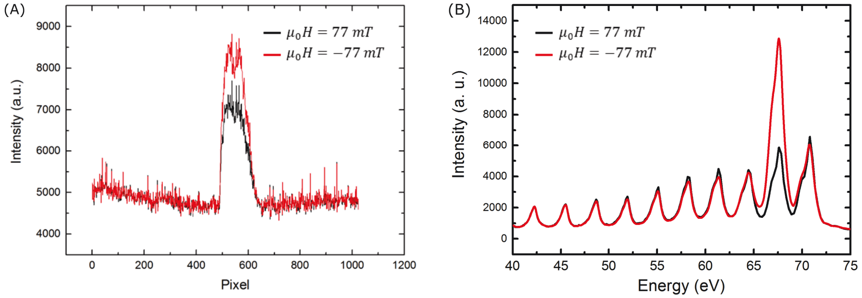

FIGURE 4.8: Magnetic asymmetries of (A) $Ni_{0.8}Pd_{0.2}$ with Bragg mirrors designed for 66 eV and (B) pure Ni grating sample with toroidal mirror.

4.2.4 Bragg mirror

A bragg mirror (dielectric mirror) is composed of multiple dielectric thin layers. The Bragg mirrors used for our measurements are made of a Mo/Si multilayer and the recommended incidence angle for the best reflectivity is 5° close to normal incidence. By controlling the material and thickness of the dielectric layer, the reflectivity can be tuned to a certain energy range[71]. A pair of Bragg mirrors were used to measure the dynamics of specific elements in a sample in T-MOKE geometry. In our case, the Bragg mirrors designed for 66 eV corresponding to the Ni $M_{2,3}$-edge were used. One has a curved surface to focus the XUV source on the sample surface and the other one has a flat surface. Since only one element is observed by the monochromatic light, samples with a flat surface instead of a grating were studied. Figure 4.8(A) shows intensities of monochromatized light reflected from $\mathrm{Ni}_{0.8}\mathrm{Pd}_{0.2}$ in external magnetic fields of opposite directions measured with the Bragg mirrors. Magnetic asymmetry can be simply obtained by integrating intensities over all pixels showing the intensity difference.

4.2.5 Toroidal mirror

As shown in Figure 4.7(B), a toroidal mirror is used for element-selective measurements with grating samples. The toroidal mirror has a curved surface with two different focal lengths and the surface is coated with gold (Au) to enhance the XUV reflectivity. In our experimental setup, the toroidal mirror (R_h=10500 mm, R_v=65.4 mm) was designed to have focused XUV light on the sample surface and the CCD detector. Regarding focus of the XUV source as a probe beam on the sample surface, the size of the XUV spot should be smaller than that of the pump beam on the surface, to see a proper demagnetization of the sample without any disturbance by probing an unexcited part. In Chapter 5.2.4, all the samples are completely demagnetized for comparison and analysis of the demagnetization. Therefore, the smaller focus size of the probe beam by the toroidal mirror is favored keeping the smaller pump beam with higher fluence on the sample surface. In the case of the XUV focusing on the CCD, the focus is related to the energy resolution of the spectra, which is important for the dynamic analysis with element selectivity. Figure 4.8(B) shows intensities of all harmonics reflected from the grating Ni sample measured with the toroidal mirror. In the case of using the toroidal mirror with a grating sample, the magnetic asymmetry of a specific element can be obtained by integrating the energy range of spectrum corresponding to the absorption edge of the element.

Introducing a grating on each sample surface leads to a difficult data analysis, since a precise energy calibration must be assigned to the spectrum from each grating sample. A new toroidal mirror is required for the next generation of the T-MOKE experiment,

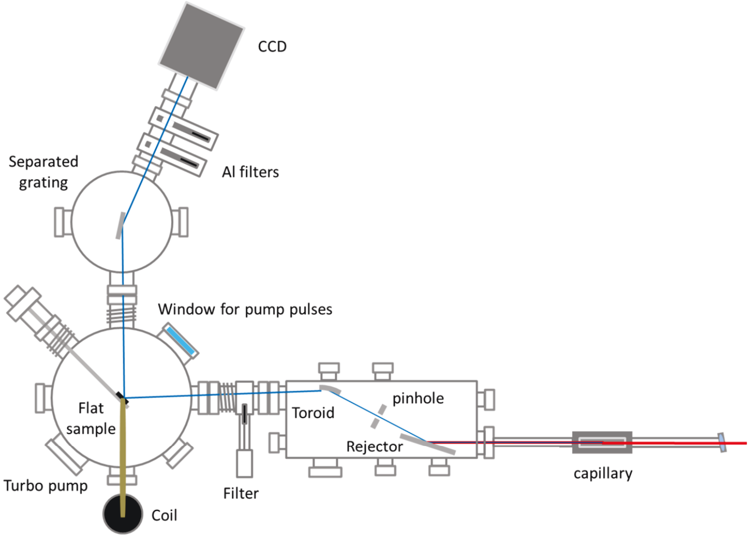

FIGURE 4.9: A schematic of the new T-MOKE setup with a separated grating.

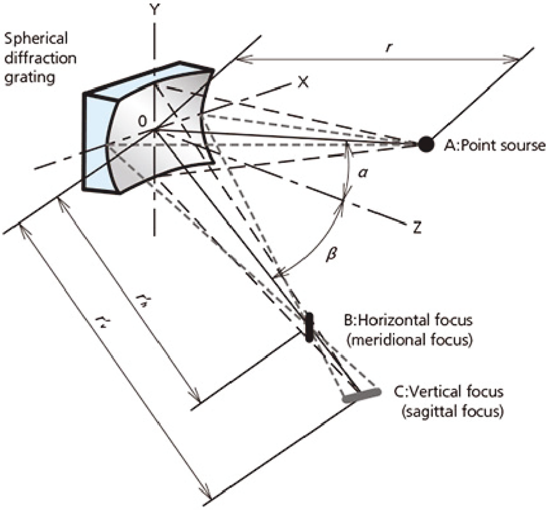

FIGURE 4.10: A toroidal mirror has two different radii leading to two different focal points. The focal points have linear shape and form a right angle [72].

with a separated grating and flat samples to avoid such difficulties (see Figure 4.9). Prior to making a toroidal mirror, the curvature radii of the toroidal mirror should be calculated by optical formalisms [72].

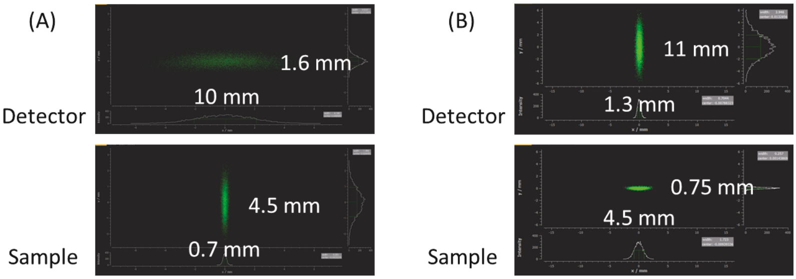

FIGURE 4.11: Profiles of the XUV light spot on the sample and the CCD from RAY-UI simulations of two different toroidal mirrors for the new T-MOKE configuration in Figure 4.9. (A) Results for the old toroidal mirror (R$_h$ = 10500 mm and R$_v$ = 65.4 mm) (B) Results for the new toroidal mirror with calculated radii (R$_h$ = 6768.1 mm and R$_v$ = 94.8 mm)

$$\frac{cos^2\alpha}{r} + \frac{cos^2\beta}{r'_h} - \frac{cos\alpha + cos\beta}{R_h} = 0 \tag{4.10}$$

$$\frac{1}{r} + \frac{1}{r'_v} - \frac{cos\alpha + cos\beta}{R_v} = 0 \tag{4.11}$$

According to Figures 4.9 and 4.10, α (β) is the angle between normal axis on the toroidal mirror and the incident (reflected) XUV beam. The distance, r, between the point source and the toroidal mirror corresponds to the distance between the capillary and the toroidal mirror in our experimental setup. The distance, r'$_h$ (r'$_v$), between the toroidal mirror and the horizontal focus B (the vertical focus A) corresponds to the distance between the toroidal mirror and the sample (the CCD). The given parameters of the new setup are $\alpha = 84.4°$, $\beta = 84.4°$, r=750 mm, r'$_h$=590 mm, and r'$_v$=1380 mm. By substitution of these parameters in Equations 4.10 and 4.11, the desired values for the curvature radii of the toroid for the new setup are obtained as R$_h$ $\sim$ 6768.1 mm and R$_v$ $\sim$ 94.8 mm. These values are confirmed by the simulation package 'RAY-UI'[2]. Using the simulation in 'RAY-UI', the intensity and profile of the light beam passing through or reflecting on the optics can be traced for all optical elements such as mirrors, focusing lens, sample surface and the CCD. A screenshot of the 'RAY-UI' is given in the Appendix. Parameters of the light source and the optics can be tuned and the optics can be placed into the beam path. With the software, the intensities upon transmission and reflection of the light, as well as beam profiles can be simulated. The simulated results for the new T-MOKE configuration in Figure 4.9 are shown in Figure 4.11. Figure 4.11 (A) represents simulated results for the old toroidal mirror with the curvature radii, R$_h$ = 10500 mm

---

[2] The simulation software is available on `https://www.helmholtz-berlin.de/forschung/oe/fg/nanometeroptik/science/layout/ray_en.html`.

and $R_v = 65.4$ mm, and Figure 4.11 (B) shows results for the new toroidal mirror with the calculated curvature radii, $R_h = 6768.1$ mm and $R_v = 94.8$ mm. The new toroidal mirror is expected to have better focusing on both the sample and the detector with 90° rotation compared to the case of the old toroidal mirror.

4.3 Experimental Chamber and Signal Detection

4.3.1 Sample and Detector

Depending on the beamline geometry, the sample will have a flat or a grating surface. The Ni_xPd_{1-x} magnetic alloys with a grating surface spatially separates the reflected high harmonics with different diffraction angles. First-order diffraction is normally identified due to the high intensity and geometrical accessibility with the small diffraction angle near zeroth order. The T-MOKE signal can be measured on the sample by applying a magnetic field into two opposite orientations, which are parallel to the sample surface and perpendicular to the plane of incidence. The magnetic field is generated by applying currents into coils placed nearby the sample using a bipolar power supply (Kepko BOP 20-20D). The strength and direction of the magnetic field can be tuned by varying the current in the range of $\pm 5A$ corresponding to a magnetic field of $\pm 77mT$. Upon sample magnetization, the XUV light is reflected from the samples (45° incident angle) and its spectrum is recorded by the CCD (Andor Newton 920) at two opposite aligned magnetic fields. To increase the signal-to-noise ratio, the CCD chip is cooled down to $-30°$C.

4.3.2 Subpixel Shift Correction

Stable XUV light is required during the T-MOKE measurements for precise data analysis. In our experiments, a beam stabilization system with two piezo-driven mirrors and two CCD cameras has been installed in order to trace and compensate the long term laser pointing drift[64]. However, there is still small shift in the spectrum between each static measurement. A technical detail to compensate such a shift, the so-called Subpixel Shift Correction, is described below.

Although the beam stabilization system operates all the time during the measurement, there is still a small shift of the spectra along the energy axes for the magnetic fields, I(↑) and I(↓). The shift is normally smaller than the pixel size ($2.6*2.6\ \mu m^2$) of the CCD and frequently results in undesired sharp spikes in the magnetic asymmetry (See Figure 4.12).

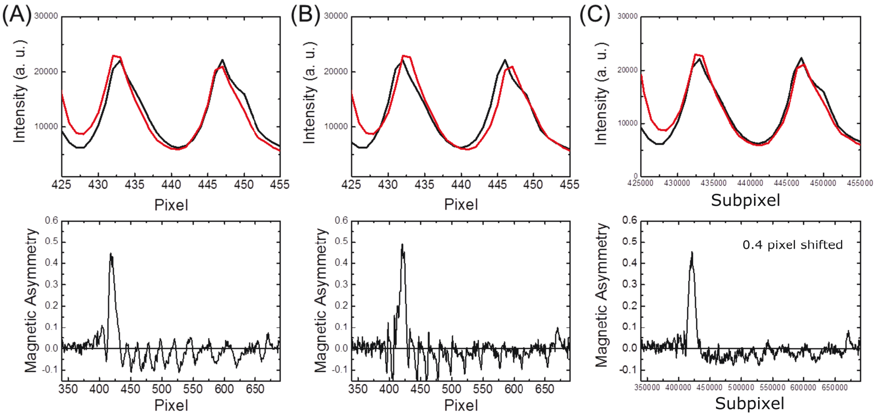

FIGURE 4.12: (A) Part of original spectra of I(↑) and I(↓) with subpixel shift (top) and asymmetry shows sharp spikes (bottom). (B) Spectra with 1 pixel shift correction and resulting asymmetry with sharp spikes. (C) Spectra and asymmetry with subpixel shift correction. The asymmetry becomes smoother.

In addition, the measured spectra often display narrow peaks and therefore a small shift is likely to result in a considerable distortion of the magnetic asymmetry (Figure 4.12(A)). As shown in Figure 4.12, a relative shift of the spectra leads to sharp peaks in the magnetic asymmetry that cannot be compensated simply by moving the spectra by 1 pixel as shown in Figure 4.12(B). Thus, a subpixel shift correction is employed for the static T-MOKE analysis, in which neighboring pixels are connected by a linear fit and the fitted line is divided into 1000 subsegments. For a static magnetic asymmetry from two spectra with subpixel size shift, the correction can be performed by the energy axis of one spectrum being shifted by subsegments, until both spectra overlap properly. As a result, the magnetic asymmetry becomes smoother with lower spikes (see Figure 4.12(C)). The MATLAB codes used for the subpixel shift correction can be found in the Appendix. The subpixel shift correction is applied to the static T-MOKE analysis for a smoother magnetic asymmetries of $\mathrm{Ni}_x\mathrm{Pd}_{1-x}$.

4.3.3 Pump-Probe Technique

In this study, the pump-probe technique has been employed in order to investigate the spin dynamics in $\mathrm{Ni}_x\mathrm{Pd}_{1-x}$ alloys. The laser output from the amplification system is split into two parts, pump and probe. The probe pulse is used to generate XUV light from HHG process as discussed in Section 2.5, and the pump pulses are used to excite the $\mathrm{Ni}_x\mathrm{Pd}_{1-x}$ samples. An optical delay stage controls the time interval between the pump pulse and the probe pulse by varying the optical path of the pump pulse.

All dynamics data were measured by the following procedure. First, we made sure that the pump- and probe beams have the same optical path length and the pulses propagating along either of the two paths reach the sample at the same time (so-called zero-delay time). The zero-delay is checked by passing the both pulses through a BBO crystal at the sample position. At the complete spatial and temporal overlap of the pump- and probe pulse, additional radiation with sum-frequency of the pump- and the probe pulse is generated. After finding the zero-delay, the demagnetization is expected to happen from the zero-delay position in that the excited sample exhibits a steep initial decrease of the magnetic asymmetry (demagnetization) followed by a recovery of the magnetization (relaxation). The time axis of the demagnetization process is given from the travel distance of the delay stage divided by the speed of the light. One millimeter of the stage movement corresponds to 2 mm of the travel distance of the pump beam due to the beam reflection at the folding mirrors. This results in 6.6 femtosecond time difference. As the time interval between the pump and the probe varies by the delay stage, two intensity profiles of the XUV spectra are measured by the CCD camera for magnetic fields with two opposite orientations. Normally, 30 seconds exposure time is taken for each spectrum. The magnetic asymmetry is calculated by Equation 2.28 for every pixel column from the background subtracted intensity profiles, where the minimum value of the intensity profiles is taken as the background value. Then, the asymmetry of $\mathrm{Ni}_x\mathrm{Pd}_{1-x}$ alloys is determined from an integration of the asymmetry over the energy range corresponding to the absorption edges of Ni at 67±2 eV and Pd at 51±2eV. Several cycles of demagnetization are measured and averaged for precise data analysis with small error values. The series of averaged asymmetries for the whole range of delay stage are fitted by a double exponential function 2.27, which was phenomenologically introduced to describe the time evolution of the magnetization after optical excitation. As a result, the demagnetization curve with dynamic parameters such as the degree of magnetization quenching (Δm), zero delay time (t_0), demagnetization time (τ_M) and relaxation time (τ_E) is obtained. The demagnetization time τ_M and the relaxation time τ_E quantify how fast the sample loses and recovers the magnetization after excitation by the pump pulse. In Chapter 5, we mainly focus on the demagnetization time τ_M, for which the M3TM of the Ref.[3] predicts a dependence on the atomic magnetic moment μ_{AT}, the Curie temperature T_C, and the spin-flip scattering probability a_{sf}.

Chapter 5

Experimental Results: Element Selective Investigation of Dynamics in $\mathrm{Ni}_x\mathrm{Pd}_{1-x}$ Alloys

In Chapter 5, the magnetic properties and spin dynamics of the $\mathrm{Ni}_x\mathrm{Pd}_{1-x}$ alloys are investigated element selectively using resonant reflectivity of XUV light. As discussed in the Chapter 2, elemental paramagnetic Pd almost fulfills the Stoner criterion. By alloying with Ni, Pd atoms are expected to magnetically couple to adjacent ferromagnetic Ni atoms leading to induced magnetization in the Pd subsystem. In Section 5.1, we observed a magnetic signature of the Pd subsystem due to the induced magnetization. Calculated magneto-optical asymmetries based on the density functional theory (DFT) show close agreement with the measured results. In Section 5.2, element-selective dynamics in the Ni- and Pd subsystems of $\mathrm{Ni}_x\mathrm{Pd}_{1-x}$ alloys are presented. Femtosecond spin dynamics measured at the Ni absorption edge indicates that increasing the Pd concentration, which causes a decrease of Curie temperature T_C, results in a drop of the demagnetization time τ_M, contrary to the $\tau_M \sim (1/T_C)$ scaling expected for single-species materials. This observation is ascribed to the increase of the Pd-mediated spin-orbit coupling (SOC) in the alloy.

5.1 Static Magnetic Asymmetry of $\mathrm{Ni}_x\mathrm{Pd}_{1-x}$ Alloys

In order to experimentally prove the induced magnetization of the Pd subsystem in $\mathrm{Ni}_x\mathrm{Pd}_{1-x}$ alloys, static magnetic asymmetries of the alloys were measured by T-MOKE geometry using XUV light. The samples with grating surface spatially separate high harmonics after XUV light reflection and the resultant spectrum is recorded by CCD.

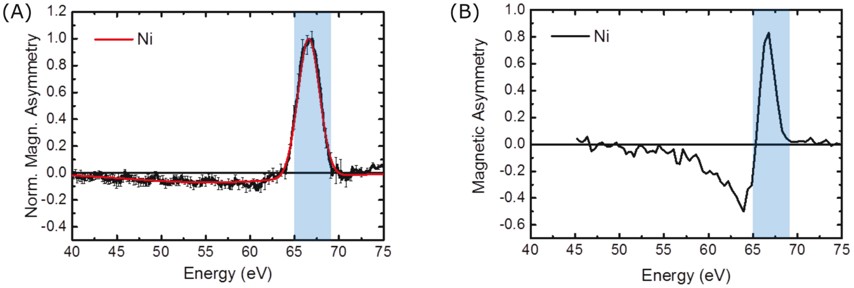

FIGURE 5.1: (A) Measured magnetic asymmetry of pure Ni with relatively weak negative part reaching to lower than 40 eV in the static T-MOKE. (B) Simulated magnetic asymmetry of pure Ni done by the Yeh-MOKE program [75],[76].

Magnetic asymmetries of the Ni_xPd_{1-x} alloys with element selectivity can be measured at the parts of the XUV spectrum corresponding to the absorption edges of the Ni and Pd elements. In the experiment, the reflected XUV spectra have been measured 4 times with external magnetic fields in sequence $\uparrow$, $\downarrow$, $\downarrow$, $\uparrow$ in order to reduce the drift resulting in a slight shift of the spectra. Assuming that Pd is magnetically coupled to Ni in the alloy, the induced magnetic asymmetry of paramagnetic Pd is expected to show up for high Pd concentration. This section presents magnetic asymmetries of Ni_xPd_{1-x} alloys with varying stoichiometry.

In previous studies, $M_{2,3}$ absorption edges of magnetic transition metals have been observed in a relatively broad energy range extending a few eV around the corresponding tabulated absorption energies [5],[73],[74],[1]. XUV light tuned to an absorption edge of a particular element shows a strong reflection dependence upon magnetic field changes in T-MOKE measurement, thus allowing element-selectivity in the observation of a strongly increased magnetic asymmetry. To have a clear access to the elemental subsystems in multi-element compounds, the elements should have their resonant energies clearly separated to avoid spectral overlap. In static T-MOKE of Ni_xPd_{1-x} alloys, magnetic asymmetry in energy range from 40 to 75 eV covering the Nickel $M_{2,3}$- and Palladium N_3-edges was obtained from recorded spectra using Equation 2.28.

5.1.1 Magnetic Asymmetry of Pure Ni

In order to see the effect of Pd on the magnetic asymmetries of Ni_xPd_{1-x}, the magnetic asymmetry of pure Ni should be first checked in our T-MOKE measurement. Figure 5.1 compares the magnetic asymmetry of pure Ni measured by the static T-MOKE setup and simulated magnetic asymmetry of pure Ni using the Yeh-MOKE program[1] based on

---

[1] The program is available on `http://juser.fz-juelich.de/record/135891/files/`

[75],[76]. The static T-MOKE result has some evident features. First, the negative part of the Ni asymmetry is relatively weak compared to the positive part. The next feature is the long tail of the negative asymmetry which extends to below 40 eV. Therefore, the asymmetry of pure Ni may show some overlap with Pd N_3 edge around 51 eV. In Ref. [5],[38],[36], the magnetic asymmetry of the Ni in a Permalloy or a Ni/Ru/Fe multilayer system has been shown with recognizable differences as compared to the simulated asymmetry of Ni by Yeh-MOKE. One of the reason for such difference in the magnetic asymmetry could be the incident angle dependent reflection coefficient of p-polarized light as discussed in the Section 2.4.2. This leads to incident angle dependence of magnetic asymmetry as shown in Figure 2.18. Magnetic asymmetry of Permalloy exhibits change of magnitude and width of the asymmetry for varying incident angle.

5.1.2 Magnetic Asymmetry of $Ni_{0.8}Pd_{0.2}$

Figure 5.2(A) shows the XUV spectra after reflection from a $Ni_{0.8}Pd_{0.2}$ film with 20 nm of thickness deposited on top of the SiO_2 substrate with prepatterned grating. The external magnetic fields, $\mu_0 H = \pm 77$ mT, were applied to saturate the magnetization of $Ni_{0.8}Pd_{0.2}$ in two opposite orientations. As shown in Figure 5.2(B), the magnetic asymmetry for this particular sample stoichiometry yields $A \sim 33.7$ % and -4.6 % at the Ni $M_{2,3}$- and Pd N_3-edges, with opposite signs for A_{Ni} and A_{Pd}. The Pd N_2 edge at 55.7 eV is not visible due to short core hole lifetime [77]. This is one of our first experimental evidences for the induced magnetic asymmetry of the Pd subsystem by coupling with ferromagnetic Ni subsystem in the alloy. The magnetic asymmetry between 56 and 61 eV shows a weak negative value, which is related to the negative part of the bipolar signal at the Ni absorption edge [73].

5.1.3 Static Measurements of Induced Magnetization in Pd

Magnetic asymmetries of Ni_xPd_{1-x} with varying stoichiometry were measured by static T-MOKE. As the Pd content in the alloy increases, the magnetic asymmetry near the Pd N_3-absorption edge becomes more pronounced. Figure 5.3(A) shows the magnetic asymmetry of the pure Ni film with grating on the surface, which exhibits a pronounced peak at a resonant energy of 68 eV. The negative part of the asymmetry extends in the energy range down to 43.5 eV. As shown in the magnetic asymmetry of the $Ni_{0.5}Pd_{0.5}$ alloy (see Figure 5.3(C)), the asymmetry of Pd also has a bipolar shape in the energy range from about 55 eV to below 40 eV. This is our first experimental observation of the induced magnetic asymmetry at the absorption edge of an intrinsically non-ferromagnetic material measured by laser-based XUV T-MOKE. Due to the negative

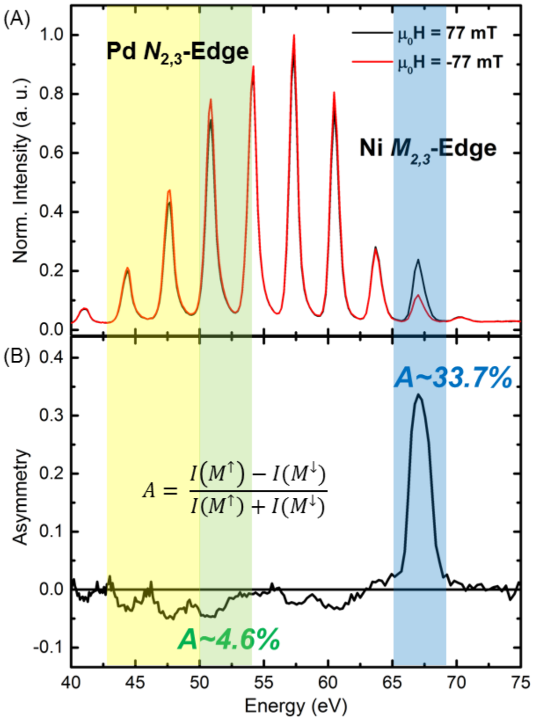

FIGURE 5.2: (A) Normalized XUV reflectivity spectra of $Ni_{0.8}Pd_{0.2}$ alloy, recorded in static T-MOKE setup at a magnetic field oriented 'up'(black) and 'down' (red), with respect to the plane of incidence, covering both the Ni $M_{2,3}$-edge (67 eV, blue area) and the Pd N_3-edge (51 eV, green area). The yellow field marks the energy interval below the tabulated Pd N_3-edge. (B) Magnetic asymmetry of $Ni_{0.8}Pd_{0.2}$ calculated from the above spectra.

part of the Ni asymmetry, the negative part of the Pd signal is expected to be slightly enhanced and the positive part to be suppressed. The Pd signal is assumed to be dominant in the energy range below 55 eV in the Ni_xPd_{1-x} alloys with higher Pd content. As shown in Figure 5.3 (B) and (C), a higher Pd concentration results also in the appearance of an additional resonance peak close to the Ni absorption edge (near 70 eV). The interpretation of this spectral feature is still under debate.

The measured magnetic asymmetries of Ni and Ni_xPd_{1-x} alloys were compared with calculated magneto-optical permittivity spectra based on density functional theory (DFT). (See Figure 5.3) The magneto-optical off-diagonal dielectric tensor element $\epsilon_{xy}(\omega)$, which is related to the magnetic response and the diagonal dielectric tensor element $\epsilon_{xx}(\omega)$ were calculated using the linear response theory; the *ab initio* calculated relativistic electronic structure including the splitting of the semi-core levels due to spin-orbit and exchange

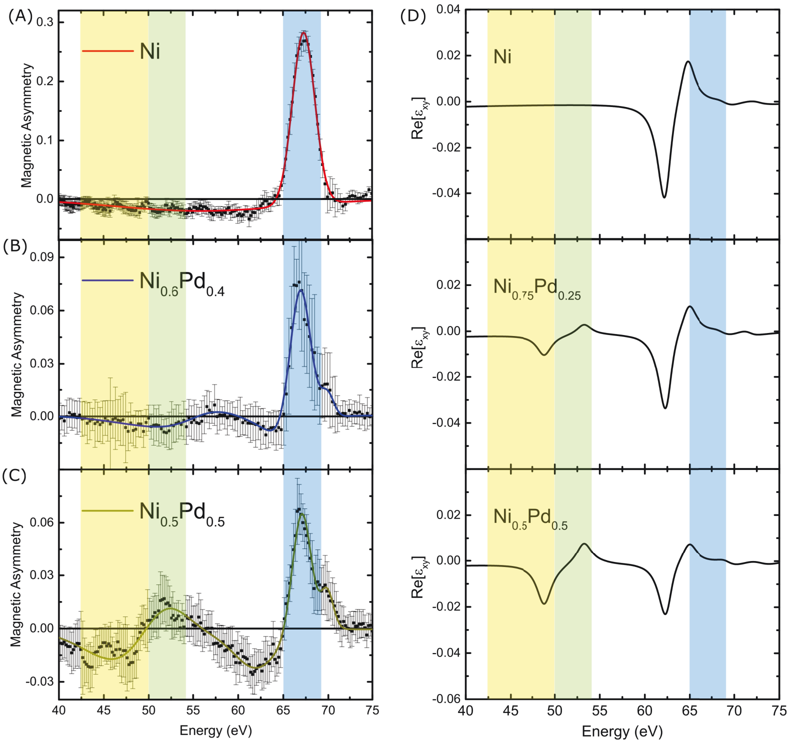

FIGURE 5.3: Magnetic asymmetries of (A) pure Ni, (B) $Ni_{0.6}Pd_{0.4}$, and (C) $Ni_{0.5}Pd_{0.5}$ from static T-MOKE measurements are compared with (D) the calculated absorptive part of the magneto-optical permittivity, $Re[\epsilon_{xy}(\omega)]$, of Ni (top) and $Ni_{0.75}Pd_{0.25}$ (middle) and $Ni_{0.5}Pd_{0.5}$ (bottom), based on the density functional theory (DFT). The Ni $M_{2,3}$-edge is located around 65 eV (near blue) and the Pd $N_{2,3}$-edge around 51 eV (green and yellow). Pure Ni shows a bipolar asymmetry with stronger amplitude in the negative part compared to the positive part. Similar to the experiment the calculated spectra show a bipolar magnetic asymmetry at the Pd $N_{2,3}$-edge that increases in amplitude with the Pd content.

interactions. The lifetime broadening of the spectra was taken to be 1 eV. Details of the method can be found in [1]. The measured magnetic asymmetry at the Ni $M_{2,3}$-edge shows a bipolar shape with higher absolute value at the positive part compared to that of negative part. If we compare this experimental asymmetry with the computed absorptive part of the magneto-optical response (i.e. the $Re[\epsilon_{xy}(\omega)]$ spectra in Figure 5.3(D)), the calculation shows the opposite relation of the amplitudes with respect to the positive- and negative parts of the Ni asymmetry. The reason for this can be that the T-MOKE asymmetry A depends on the magneto-optical permittivity $\epsilon_{xy}(\omega)$ as well as on the XUV index of refraction, specifically,

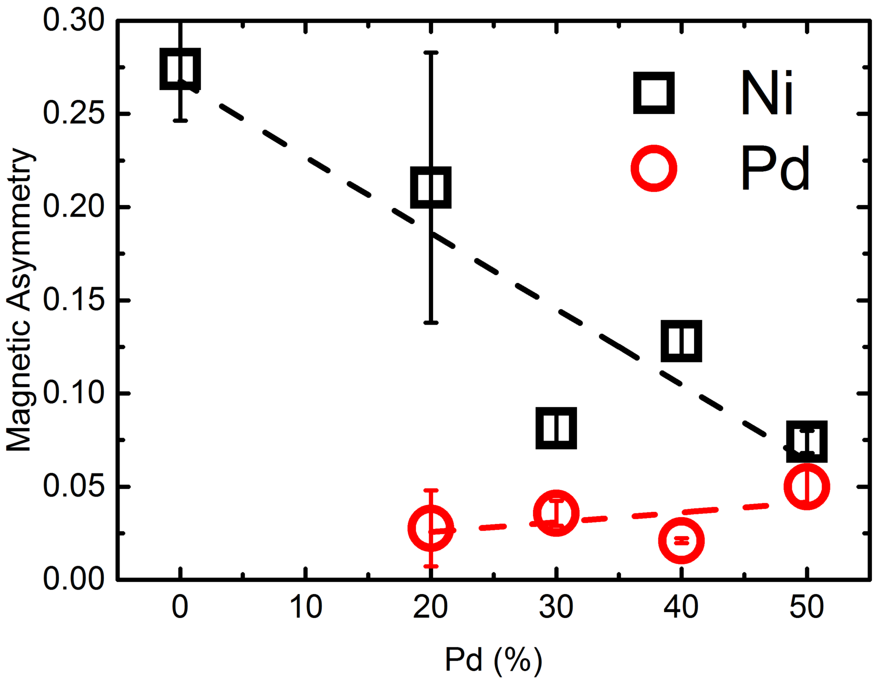

FIGURE 5.4: Increasing Pd content results in an increase (decrease) of the Pd (Ni) asymmetry. Dashed lines are guides for the eye.

$$A = 2Re\left[\frac{sin2\theta}{n^4cos^2\theta - n^2 + sin^2\theta}\epsilon_{xy}\right] \tag{5.1}$$

with n the complex refractive index and θ the angle of incidence relative to the film normal [51]. Hence, the T-MOKE asymmetry can be modified by the prefactor. In addition, there can be multiple reflections occuring in the thin film. The *ab-initio* calculated magneto-optical spectrum of Ni is at a slightly lower energy (positive peak at 65 eV) than the measured T-MOKE asymmetry (peak at 67 eV). This is due to the calculated $3p$ semi-core level energies, which can differ somewhat from the measured energy positions. The computed energy position of the Pd $4p$ states ($N_{2,3}$-edge) compares quite well with the measured energy showing the magneto-optical signal at the Pd $N_{2,3}$-edge around 50 eV in Figure 5.3(D). For Pd, the computed magneto-optical bipolar shape agrees well with the measured magnetic asymmetry. Similar to the experiment, the calculated N-edge magneto-optical signal increases with increasing Pd content.

In order to obtain a sufficient signal-to-noise ratio for the magnetic asymmetry we average over several (up to 10) $I(H^{\downarrow,\uparrow})$ spectra before calculating the asymmetry A according to Equation 2.28. After plotting the resulting magnetic asymmetry spectrum, we define

±2 eV energy intervals around the resonance energies shown by the colored rectangles (blue for Ni and green for Pd) and a 7.5 eV energy interval below the tabulated Pd edge (yellow rectangle). We add all asymmetry data points in such an interval and divide the sum by the number of data points to calculate the average magnetic asymmetry of the given interval. Figure 5.4 shows the averaged asymmetry values, which are lower than the measured peak asymmetry in Figures 5.2(B) and 5.3(A)-(C). For example, Ni shows a magnetic asymmetry of up to 33.7% in Figure 5.2(B), but the average asymmetry plotted in Figure 5.4 is only about 22%. Figure 5.4 shows the effect of increasing the Pd content on the averaged magnetic asymmetries recorded from pure Ni and a set of four $\mathrm{Ni_xPd_{1\text{-}x}}$ alloys. While the positive part of the Ni asymmetry (blue rectangle) continuously drops from $A \sim 27.4\%$ to 7.4%, the Pd signal (yellow rectangle) grows in magnitude from ∼ 2.76% to 5% upon increasing the Pd concentration from 10 to 50%. The magnetic asymmetries of $\mathrm{Ni}_x\mathrm{Pd}_{1-x}$ in Figure 5.4 shows stoichiometry-dependent magnetic asymmetries of Ni and Pd subsystems and the change of magnetic asymmetries could come from the stoichiometry-dependent band dispersion of $\mathrm{Ni}_x\mathrm{Pd}_{1-x}$ alloys. The increased Pd-mediated SOC and electronic hybridization of Ni and Pd are the most reasonable explanation for the band dispersion as discussed in the Section 2.2. According to Jan Rusz and Peter Oppeneer from Uppsala university in Sweden (personal communication, June, 2018), two possible effects can be considered with assumption that the background signal does not make considerable effects on the magnetic asymmetry. First, decrease of Ni leads to decrease of Ni magnetic moment contributing to total magnetization of the alloy, and analogically for Pd. According to the definition of magnetic asymmetry given by Equation 2.28, the magnetic asymmetry is the *relative* quantity. This means that decrease (increase) of Ni (Pd) does not make any effect on the magnetic asymmetry of the alloys due to the normalization. Instead band dispersion related to stoichiometry-dependent SOC and hybridization of valence bands of Pd and Ni can be an appropriate interpretation for the stoichiometry-dependent change in magnetic asymmetries. As Pd content in $\mathrm{Ni}_x\mathrm{Pd}_{1-x}$ alloy increases, average SOC in the alloy also increases due to higher atomic number of Pd(Z=46) compared to Ni(Z=28). While Ni and Pd are magnetically coupled via complex exchange interaction in the $\mathrm{Ni}_x\mathrm{Pd}_{1-x}$ alloy, the valence bands of the Ni and the Pd are hybridized resulting in the band dispersion and the change of magnetic properties such as coercivity and magnetization. These effects consequently lead to the stoichiometry-dependent change of magnetic asymmetries in Ni and Pd subsystems in the alloys as shown in the Figure 5.4.

5.2 Spin Dynamics in $\mathbf{Ni}_x\mathbf{Pd}_{1-x}$ Alloys

After the static characterization of $\mathrm{Ni}_x\mathrm{Pd}_{1-x}$ alloys, stoichiometry-dependent transient magnetization dynamics in the alloys were measured by the pump-probe technique to understand more about Pd-mediated effects on the dynamics of the $\mathrm{Ni}_x\mathrm{Pd}_{1-x}$ alloys. A unique feature of the laser-based probing employing the entire XUV spectrum is that the response of both the Ni and Pd elemental subsystems can be monitored simultaneously. In particular, this parallel recording of the spin dynamics allows for testing of the presence of spin currents between the elemental subsystems, i.e., whether or not one of the subsystems can act as spin source and the other as a spin sink [5],[78],[14].

Regarding the stoichiometry-dependent dynamics in $\mathrm{Ni}_x\mathrm{Pd}_{1-x}$ alloys, as discussed in Section 2.2, the demagnetization time based on M3TM scales with the atomic moment μ_{AT}, spin-flip scattering probability a_{sf} and Curie temperature T_C as $\tau_M \sim \mu_{AT}/\mathrm{a}_{sf}\mathrm{T}_C$, if we assume that the phonon bath temperature T_p is constant in the considered time interval. While with increasing amount of Pd in the $\mathrm{Ni_xPd_{1\text{-}x}}$ alloy, the slowly varying μ_{AT} is expected to have negligible effect on τ_{M}, the sizable decrease of T_{C} is expected to lead to a τ_{M} *increase*, if we assume a constant a_{sf}. However, because a_{sf} scales with the nuclear charge (Z) as $a_{\mathrm{sf}} \propto Z^4$ and $Z_{\mathrm{Pd}} = 46$ is almost twice as large as $Z_{\mathrm{Ni}} = 28$, τ_{M} is expected to be strongly affected by a_{sf} as well, depending thus again on the $\mathrm{Ni_xPd_{1\text{-}x}}$ stoichiometry [3],[79]. In particular, for increasing Pd content the increasing a_{sf} can (over)compensate the effect of the decreasing T_{C} on τ_{M}, and, thus, drive the $\mathrm{Ni_xPd_{1\text{-}x}}$ dynamics into a completely opposite dependence on composition resulting in a τ_{M} *decrease* with increasing Pd content. We note that the a_{sf} variation is predominantly governed by the increasing amount of Pd. Therefore, measuring the τ_{M} variation in the Pd subsystem might be a more direct signature of this tendency. However, at low Pd concentrations, the T-MOKE signal at the Pd absorption edge is weak, resulting in a signal-to-noise ratio too small to determine τ_{M} values with the required precision. The fact that the magnetic moment of Pd is induced due to the proximity of Ni implies a strong coupling between the Pd and Ni subsystems. Hence, an a_{sf} variation is expected to affect the Ni response, too. Therefore, we focus exclusively on the *dynamics of the Ni elemental subsystem* in the following. Note, that the Ni-Pd exchange coupling is assumed constant at this time, although it may vary with stoichiometry as well.

In the Section 5.2.1, we first compare dynamics of $\mathrm{Ni}_{0.8}\mathrm{Pd}_{0.2}$ in two different pump-probe configurations for the flat sample surface and a grating surface to confirm that the state of the sample surface does not make any effect on the spin dynamics. Afterward, the spin dynamics in the Ni- and Pd subsystems of the $\mathrm{Ni}_{0.5}\mathrm{Pd}_{0.5}$ alloy are compared (see Section 5.2.2).

In the following part, the stoichiometry-dependent dynamics of the $\mathrm{Ni}_x\mathrm{Pd}_{1-x}$ alloys are measured in the Ni subsystem, because the magnetic signal from the Pd subsystem is

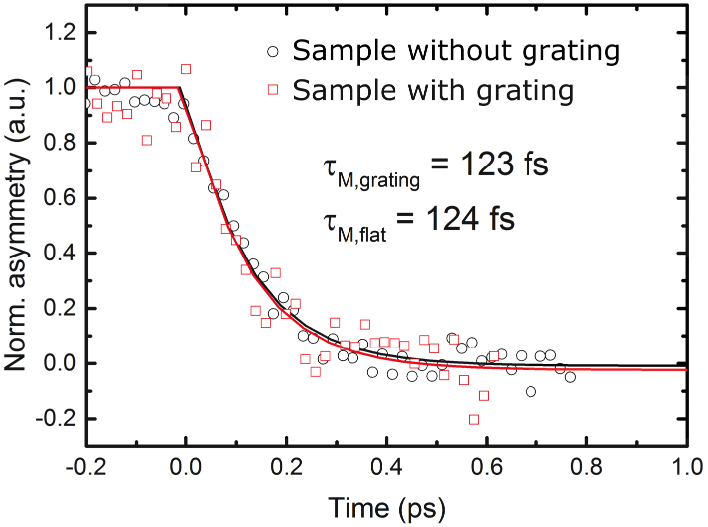

FIGURE 5.5: Demagnetization curves of $Ni_{0.8}Pd_{0.2}$ with different types of sample surface, flat and grating, being compared. Both samples exhibit almost identical demagnetization curves showing negligible difference.

weak with low signal-to-noise ratio compared to that of the Ni subsystem at low concentration of the Pd (0 to 40%). There are two main topics in spin dynamics. We first investigate the response of the Ni subsystem to a constant pump fluence in samples with different compositions(see Section 5.2.3). In the Section 5.2.4, the pump fluence was adjusted to reach full quenching for all samples to investigate the stoichiometry-dependent demagnetization times.

5.2.1 Dynamics Comparison for Two Different Experimental Configurations

As discussed in Section 4.2.3, there are two different T-MOKE configurations to measure magnetic asymmetries (see Figure 4.8). One uses a monochromatized light source by a pair of Bragg mirrors for studying the dynamics in only one particular elemental subsystem of the sample with flat surface. This approach provides experimental simplicity without fabrication of grating and simple analysis of the data by integration of entire intensity. The other one uses a toroidal mirror, which focuses the entire XUV spectrum on the sample with grating and the CCD camera. This approach gives the opportunity of a simultaneous dynamic measurement in multi-element compounds or multilayers with element selectivity. In Section 5.2.3, the dynamics of Ni_xPd_{1-x} was measured in T-MOKE geometry with a pair of Bragg mirrors. In Section 5.2.2 and 5.2.4, the dynamic measurements of the alloys were performed in T-MOKE geometry with a toroidal mirror and grating samples. To make sure that the results from one sample with flat surface and grating are the same, the dynamics of $Ni_{0.8}Pd_{0.2}$ in both experimental configurations are compared, when the sample magnetization is fully quenched in both cases (see Figure 5.5). No evident effect of the type of the sample surface on dynamics was observed and both show almost identical demagnetization curves. We experimentally confirmed that the patterned grating on the sample surface does not affect the spin dynamics in the Ni_xPd_{1-x} alloys.

5.2.2 Element Selective Dynamics of the Ni and Pd Subsystems

In order to compare the spin dynamics in Ni- and Pd subsystems in an alloy and experimentally confirm a possible spin angular momentum transfer between the subsystems, we measured the element-selective dynamics in a $Ni_{0.5}Pd_{0.5}$ alloy. In this measurement, the only positive part of the Ni asymmetry and the only negative part of the Pd asymmetry, which might be enhanced by the negative part of the Ni edge were integrated to get the magnetic asymmetry.

All measured stoichiometries ($x = 1.0 \ldots 0.5$) show qualitatively the same spectral behavior with the Pd (Ni) signal continuously increasing (decreasing) with increasing Pd concentration (see Figure 5.4). For Pd concentrations above 50% the T-MOKE signal drops again, now due to the fact that the magnetization of the alloy films rotates out-of-plane [50]. Variations of the magnetic asymmetry of the samples with Pd content less than 50%, triggered by the optical excitation, are therefore in the first approximation assumed to represent the dynamics of the Pd elemental subsystem. Our time-resolved data in Figure 5.6 show that both the Ni and the Pd subsystems demagnetize, with the Ni showing an about 30% faster demagnetization time compared to Pd. This fact may lead to the conclusion that the Pd subsystem is slower and 'follows' the spin dynamics of Ni. However, for Pd concentrations below 50%, the Pd signal is weak, which leads to an appreciable scattering of the τ_M values making it difficult to confirm the slower Pd response and possible stoichiometry dependence. On the other hand, all measured transients consistently show a demagnetization of both Ni and Pd subsystems in the entire concentration range, which may again lead to the conclusion that, for the chosen laser fluence, there is *no clearly detectable spin-rearrangement between the Ni and Pd subsystems induced by spin currents.*

Previously, spin currents arising from ultrafast laser induced demagnetization have been observed between laterally separated sample areas [12], between adjacent metallic layers [5],[9], and between different sublattices in ferrimagnetic rare-earth-transition metal films [78],[80]. In the latter observation, it was shown that the total angular momentum

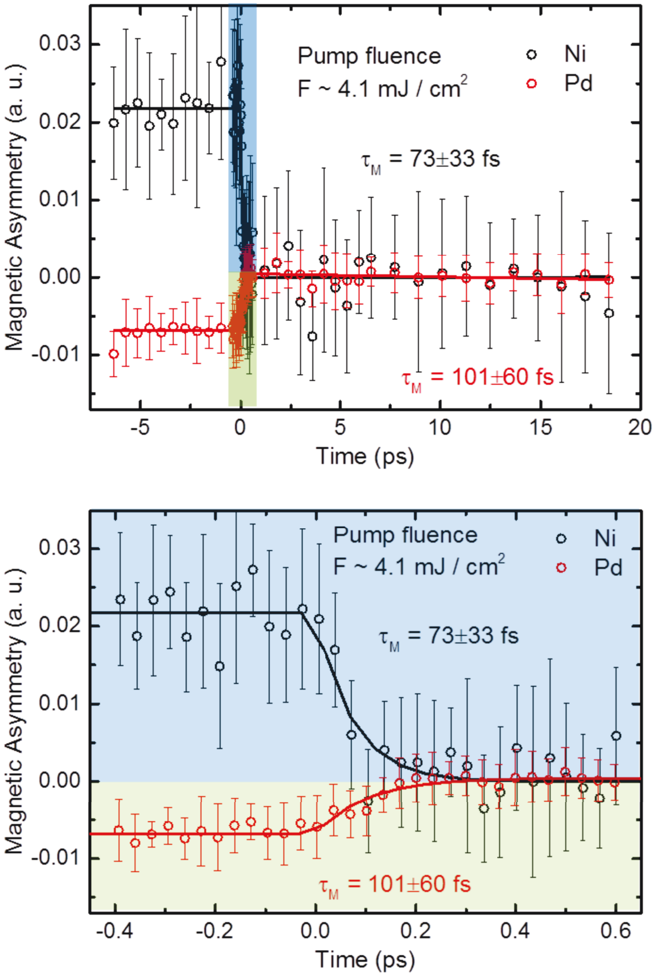

FIGURE 5.6: Spin dynamics measured at the Ni and Pd absorption edges in the $Ni_{0.5}Pd_{0.5}$ alloy. Black and red symbols represent experimental values for Ni and Pd, respectively, which are simultaneously obtained from the measured XUV spectra. Solid lines are the double-exponential fits from which τ_M values were extracted. The lower figure is a magnification of the colored time interval around $t = 0$ marked in the left graph. The $Ni_{0.5}Pd_{0.5}$ alloy was pumped with the laser fluence $F \sim 4.1$ mJ/cm^2. Both Ni and Pd subsystems show a complete demagnetization with Ni demagnetizing faster than Pd. Slow recovery times τ_R in the range of hundreds of ps to several ns have been observed for both subsystems in a separate measurement (not included).

of the two sublattices stays constant in the initial phase after the laser excitation, due to transfer of angular momentum from the transition metal atoms, where the spin-polarized $3d$ states are strongly excited by the laser, to the lanthanide atoms, where the deep-lying $4f$ states are not immediately excited by the laser. After the initial conservation of angular momentum, thermally dominated demagnetization sets in. For our $\mathrm{Ni_xPd_{1\text{-}x}}$ alloys, however, we cannot confirm a similar effect. In the presence of *ferromagnetic* coupling expected from the less than 10% decrease of the magnetic moment up to 45% of Pd content in the alloy [41], similar to Ref. [5], a spin current would result in an *enhancement* of the magnetic signal at one of the absorption edges. Even by lowering the laser fluence up to a complete disappearance of the Pd signal (results not shown), we did not observe this effect. We conclude that an optically triggered spin current between the subsystems, if the spin current presents in the $\mathrm{Ni}_x\mathrm{Pd}_{1-x}$ alloys, is not dominating the spin dynamics in $\mathrm{Ni}_x\mathrm{Pd}_{1-x}$ alloys. Rather, the demagnetization of Pd closely follows the Ni demagnetization, possibly with a slower demagnetization rate. This suggests that a local demagnetization mechanism on both Ni and Pd plays an important role.

Regarding spin transfer between Ni and Pd subsystems as discussed in Section 2.3.3 [17], the OISTR has not been observed in the dynamics of $\mathrm{Ni_{0.5}Pd_{0.5}}$ since the demagnetization times of Ni and Pd subsystems are slower than 40 fs in which OISTR is valid. Instead, in our analysis we show that the dynamics of $\mathrm{Ni}_x\mathrm{Pd}_{1-x}$ alloys is governed by the spin-orbit induced spin-flip scattering. In order to elucidate the effect of OISTR on the dynamics in the $\mathrm{Ni}_x\mathrm{Pd}_{1-x}$ alloys, the pump pulse with short pulse duration and higher fluence should be employed as addressed in Ref. [17].

5.2.3 Spin Dynamics in the Ni Subsystem with Constant Pump Fluence

In this section, we measured the dynamics of $\mathrm{Ni}_x\mathrm{Pd}_{1-x}$ alloys with constant pump fluence. Figure 5.7 shows the corresponding demagnetization curves for Pd contents of 0%, 10%, and 20%. The magnetic asymmetries were calculated using Equation 2.28. The curves were then normalized by setting the initial asymmetries (before zero time delay) of all the samples to unity in order to trace the dynamics as a function of the alloy composition (the same procedure was used to obtain Figure 5.8 in Section 5.2.4). With increasing Pd content, the optically-induced transients show both a higher quenching (arrow a) and a slower relaxation (arrow b) of the magnetization. This observation can be interpreted as a consequence of the increase of the relative temperature T/T_C, as was shown by Roth et al. [2]. In our case, the Curie temperature T_C is decreased instead of increasing the ambient temperature T as in Ref. [2]. Nevertheless, the relaxation time and quenching appear to scale with the T/T_C ratio in a similar manner as reported

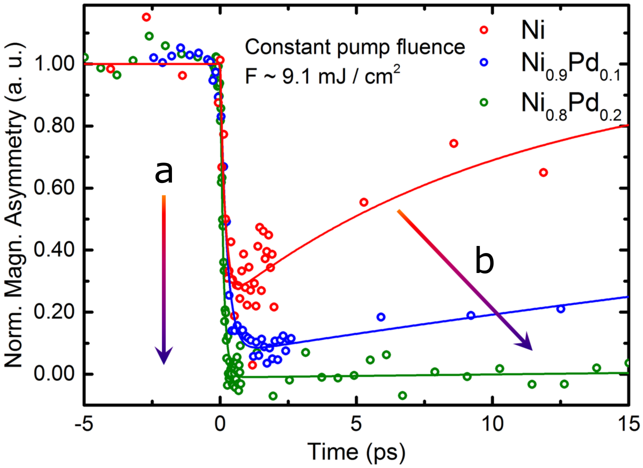

FIGURE 5.7: Spin dynamics of the Ni subsystem for two different Ni_xPd_{1-x} alloys compared to the dynamics of pure Ni. The data is recorded in the T-MOKE geometry by integrating across Ni $M_{2,3}$-edge with constant pump fluence of F $\sim 9.1 mJ/cm^2$.

Stoichiometry	Reflected Power (mW)	Reflectance (%)
Ni	6.400	73.06
$Ni_{0.9}Pd_{0.1}$	6.335	72.32
$Ni_{0.8}Pd_{0.2}$	6.250	71.35
$Ni_{0.7}Pd_{0.3}$	6.325	72.20
$Ni_{0.6}Pd_{0.4}$	6.350	72.49
$Ni_{0.5}Pd_{0.5}$	6.290	71.86

TABLE 5.1: Stoichiometry-dependent absorption of the pump energy is measured from reflectance of 800 nm on Ni and Ni_xPd_{1-x} alloys. The laser power before reflection is 8.76 mW.

in Ref. [2]. Mueller et al. investigated these results considering the influence of the ambient temperature on the demagnetization dynamics [81]. They concluded that as ambient temperature increases near Curie temperature, less energy is consumed for the same amount of quenching compared to room temperature. In our case, higher magnetic quenching for increasing Pd content can be explained by decreasing Curie temperature.

In order to exclude an argument that a stoichiometry-dependent absorption of the pump energy gives rise to the observed changes, the reflectance of pure Ni as well as Ni_xPd_{1-x} alloys ($x = 0.5, 0.6, 0.7, 0.9$) was measured at a wavelength of 800 nm (1.55 eV) (see Table 5.1). Due to the very thick substrate we can safely assume that there is no transmission, and therefore the light is mostly absorbed and reflected by the samples. The reflectance measurements were performed at room temperature and in ambient atmosphere (not in vacuum). The power of the incoming light was 8.76 mW and the angle of incidence was 45°, similar to the T-MOKE configuration. The reflectance of the measured alloys ranges

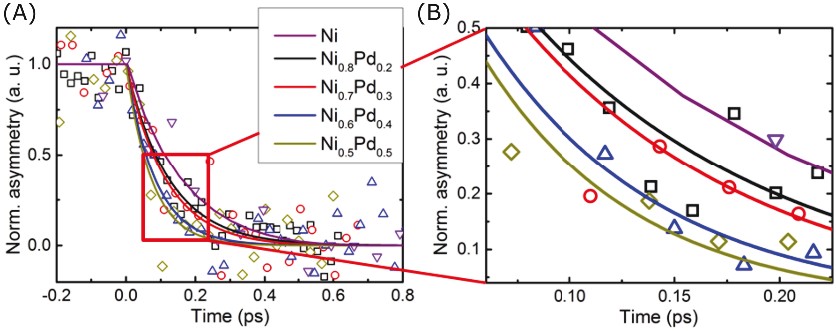

FIGURE 5.8: (A) Normalized demagnetizations from zero to one at Ni $M_{2,3}$-edge in alloys with varying compostion for comparison. Laser pump fluence for each measurement (excluding pure Ni) was adjusted to trigger full quenching. (B) Demagnetization curves near zero delay for comparison.

from 71.35 to 73.06% and seems to decrease slightly with increasing Pd content. Thus, the stoichiometry-dependent variation of the reflectance is less than 2%, i.e. relatively small compared to the 30% decrease of the Curie temperature from Ni to $Ni_{0.5}Pd_{0.5}$ [41]. Therefore, we conclude that the demagnetization of Ni and $Ni_xPd_{1\text{-}x}$ alloys is not affected by a stoichiometry-dependent light absorption.

5.2.4 Spin Dynamics in the Ni Subsystem with Constant Quenching

In order to investigate the ultrafast demagnetization regime, we performed a series of measurements where we increased the laser pump fluence for each alloy composition individually, until *full quenching* was reached. This was done in order to minimize the effect of the quenching amplitude on the demagnetization time constant (see Figure 2.12(B)) [3]. In case of the pure Ni film, however, due to its higher T_C, we reached only 70% quenching with the maximum available pump intensity.

Figure 5.8 shows transient dynamics measurements performed at the Ni absorption edge for different compositions. Open symbols show the experimental data and solid curves represent double-exponential fits to the function given in Equation 2.27, from which τ_M values have been extracted. In order to compare the responses for different compositions we normalized the demagnetization curves to be equal to 1 for the signal before the excitation and 0 for the complete demagnetization. The experimental data show scattering causing some errors, thus minimum values of the double-exponential fits for all Ni_xPd_{1-x} alloys close to zero are set to zero. The demagnetization curve for pure Ni with just 70% of quenching is also normalized from zero to one, as done for all the alloys for comparison. We note that the demagnetization time for the fully-quenched pure Ni is expected to be slightly longer than the one presented thus for 70% quenching

Stoichiometry	Demagnetization time τ_{M}
Ni	177±56 fs
$\mathrm{Ni_{0.8}Pd_{0.2}}$	123±85 fs
$\mathrm{Ni_{0.7}Pd_{0.3}}$	115±41 fs
$\mathrm{Ni_{0.6}Pd_{0.4}}$	82±41 fs
$\mathrm{Ni_{0.5}Pd_{0.5}}$	73±33 fs

TABLE 5.2: Stoichiometry-dependent demagnetization times τ_{M} measured at the Ni absorption edge.

(see Figure 2.12) [3], thus, complying with the observed dependence of τ_{M} on varying $\mathrm{Ni_xPd_{1\text{-}x}}$ composition [3],[79]. As shown in Figure 5.8(B), the curves show a consistent decrease in the demagnetization time with increasing Pd concentration. The measured stoichiometry dependent τ_{M} values are plotted in Figure 5.9 as red squares and compiled in Table 5.2.

To the best of our knowledge, this measurement is one of the first experimental confirmations of the fact that SOC has to be taken into account when discussing τ_M variations on femtosecond time scales. We stress again that considering exclusively variations of T_{C} with the alloy stoichiometry without SOC would lead to a completely opposite τ_{M} dependence. This is indicated in Figure 5.9, where the red open symbols represent our experimental results, black open circles show a qualitative prediction made on the basis of the microscopic three-temperature model (M3TM) without SOC (only μ_{AT}/T_C scaling), and blue circles indicate the τ_M variation with stoichiometry taking SOC into account ($\mu_{AT}/\mathrm{a}_{sf}\mathrm{T}_C$ scaling including a_{sf} variation). The solid lines in Figure 5.9 are guides for the eyes. As shown in Figure 5.9, the dynamic response of the Ni subsystem in $\mathrm{Ni}_x\mathrm{Pd}_{1-x}$ alloys with varying stoichiometry shows nice agreement with the prediction based on M3TM considering a_{sf}, owing to Pd-mediated SOC. The measured stoichiometry-dependent τ_M values plotted as red squares in the Figure 5.9 are compiled in Table 5.2. Note, that the phonon bath temperature T_p is assumed to be constant on the considered time scale.

Below we briefly discuss the procedure for obtaining the curves describing the theoretical models shown in Figure 5.9. To obtain the predicted tendencies, we first estimated values for μ_{AT} and T_{C} from Ref. [41]. Thus, compared to pure Ni, adding 50% of Pd results in a drop of the magnetic moment μ_{AT} by about 10% and a decrease of the Curie temperature T_{C} by approximately 30%. Furthermore, as noted above, the relative change of the spin-flip probability is assumed to scale with $a_{\mathrm{sf}} \propto Z^4$ according to SOC [82]. To get an effective Z we linearly interpolated between $Z_{\mathrm{Ni}} = 28$ and $Z_{\mathrm{Pd}} = 46$ according to the alloy composition: $Z_{\mathrm{Ni_xPd_{1\text{-}x}}} = xZ_{\mathrm{Ni}} + (1-x)Z_{\mathrm{Pd}}$ (Ref. [82]). For equiatomic $\mathrm{Ni_{0.5}Pd_{0.5}}$, we therefore obtain $Z^4_{\mathrm{Ni_{0.5}Pd_{0.5}}} = [(Z_{\mathrm{Ni}}+Z_{\mathrm{Pd}})/2]^4 = 37^4$, resulting in an estimated increase in effective a_{sf} of over 200% compared to pure Ni ($Z^4_{\mathrm{Ni}} = 28^4$).

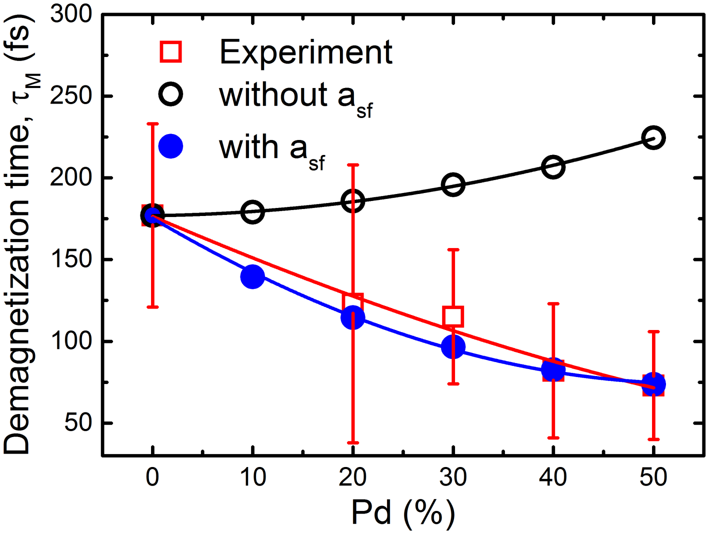

FIGURE 5.9: Stoichiometry-dependent demagnetization time. The illustration shows qualitative agreement in the τ_M variation, decreasing as the Pd content increases in the experimental data (red) and the prediction based on the M3TM with varying spin-flip probability a_{sf} (blue) owing to SOC. In contrast, demagnetization times with constant a_{sf} (black) without considering SOC appears in the completely opposite way.

In order to apply the scaling law to the experimental τ_M values, we rewrite the scaling $\tau_\mathrm{M}{\sim}\mu_\mathrm{AT}/(a_\mathrm{sf}T_\mathrm{C})$ as $\tau_\mathrm{M}{\sim}\mu_\mathrm{AT}/(Z^4T_\mathrm{C})$. Then, we calculate for each composition x in Figure 5.9 as $A_1\mu_\mathrm{AT}/(Z^4T_\mathrm{C})$ (including SOC, solid blue circles) and $A_2\mu_\mathrm{AT}/T_\mathrm{C}$ (without SOC, open black circles) employing μ_AT and T_C values from Ref. [41] and the effective $Z_\mathrm{Ni_xPd_{1\text{-}x}}$ introduced above. The proportionality factors A_1 and A_2 are determined from our experimental data point for pure Ni.

Our findings in Figure 5.9 accentuate the fact that a_sf due to Pd-mediated SOC may play a critical role for the determination of demagnetization time based on the M3TM. We note in this respect that *ab initio* calculations of the electron-phonon spin-flip scattering did confirm the existence of the electron-phonon spin-flip scattering mechanism assumed in the M3TM, but the computed demagnetization rates were smaller than the measured demagnetization rates, indicating the presence of other spin dissipation channels [83]. The *ab initio* calculations did, however, show that photon-driven creation of deep lying holes in combination with SOC causes a faster demagnetization [83]. This strong dependence of the spin-flip scattering of the deep lying holes on the SOC is consistent with our observations.

Chapter 6

Summary and discussion

This thesis provides a detailed analysis of magnetization dynamics in $\mathrm{Ni}_x\mathrm{Pd}_{1-x}$ alloys with varying stoichiometry using transversal magneto-optic Kerr effect (T-MOKE) with femtosecond-pulsed extreme ultraviolet (XUV) radiation. The study has been inspired by the idea that Pd, an intrinsic paramagnet, can become a ferromagnet when coupled to Ni in the $\mathrm{Ni}_x\mathrm{Pd}_{1-x}$ alloy system. At the same time, Pd can tune the spin-orbit coupling (SOC) of the entire system by varying Ni-Pd mixing ratio. The SOC-dependent dynamics in the $\mathrm{Ni}_x\mathrm{Pd}_{1-x}$ alloys was investigated by time-resolved measurements.

In order to theoretically support experimental results, fundamental consideration for magnetism and magnetic properties of ferromagnetic 3d transition metals were first treated. The study was expanded to the properties of the $\mathrm{Ni}_x\mathrm{Pd}_{1-x}$ alloys [41]. Depending on mixing ratio of Ni and Pd in the alloys, Curie temperature (T_C), magnetic moment (μ), spin-orbit interaction and electronic structure can be tuned. These stoichiometry-dependent parameters enable us to describe magnetization dynamics using microscopic three temperature model (M3TM). In addition, spin-reorientation transition of $\mathrm{Ni}_x\mathrm{Pd}_{1-x}$ thin film depending on film thickness and Pd concentration was also considered [42]. The stoichiometry-dependent magnetic asymmetry of $\mathrm{Ni}_x\mathrm{Pd}_{1-x}$ alloys was expected from relation between SO interaction and the valance band dispersion. Regarding to magnetization dynamics, some of plausible mechanisms responsible for the magnetization dynamics were introduced. Spin-flip scattering is considered as channel for spin angular momentum transfer in M3TM and superdiffusive spin transport explains magnetization dynamics in multilayer system. Optically-induced intersite spin transfer (OISTR) responsible for change of magnetization in both multilayer and alloy systems including magnetization switching in short time scale (below 40 fs) was also considered. Afterwards the theory for magneto-optic Kerr effect (MOKE) was stated. Transversal-MOKE originates from the off-diagonal elements of the dielectric tensor, and the signal varies as a function of incident angle of the light and wavelength-dependent magneto-optical constants. For XUV radiation, description of three step model for high harmonic generation (HHG) and phase-matching of harmonics was also given (see Chapter 2).

The $\mathrm{Ni}_x\mathrm{Pd}_{1-x}$ samples were prepared by molecular beam epitaxy (MBE) on a SiO_2 substrate. The magnetization direction of the alloys turns out-of-plane above a specific Pd content (higher than 50%) according to longitudinal-MOKE (L-MOKE) data. This spin reorientation transition (SRT) originates from the stoichiometry-dependent Pd-mediated SO interaction of the $\mathrm{Ni}_x\mathrm{Pd}_{1-x}$ alloys. The SRT from in-plane to out-of-plane in the $\mathrm{Ni}_x\mathrm{Pd}_{1-x}$ alloys determines the range of the samples for T-MOKE measurement, since the Kerr effect is observed from the sample with in-plane magnetization in the T-MOKE configuration. For a spectral analysis of the magnetic asymmetry and dynamics with element-selectivity, we introduced grating structure as a part of the sample layout and examined several fabrication methods of grating pattern (see Figure 3.1). The AFM measurement indicates that patterning of the grating in the substrate surface gives the best quality of grating, consequently, most of our $\mathrm{Ni}_x\mathrm{Pd}_{1-x}$ alloys were deposited on top of the pre-patterned substrates. We observed periodic dependence of the reflection of XUV radiation on the sample thickness and the gratings groove depth by simulation and calculation. The grating depth and the thin film thickness for efficient reflection of XUV radiation were chosen to be 7.375 nm and 20nm. Considering the attenuation length (7.8 nm to 8.5 nm) of the XUV radiation (40 to 75 eV) and 20 nm of the film thickness, the influence of the interface and the thickness dependence of the T-MOKE were not taken into account (see Chapter 3).

The magnetization dynamics in the $\mathrm{Ni}_x\mathrm{Pd}_{1-x}$ alloys was measured with pump-probe T-MOKE geometry using pulsed XUV radiation in the energy range from 20 to 72 eV. Ti:Sapphire laser with chirped pulse amplification (CPA) was employed for intense femtosecond pulse laser. XUV radiation was obtained from high-order harmonic generation (HHG) by focusing the pulse laser into narrow capillary filled with neon gas. To enhance the efficiency of HHG, the pulse duration and the energy of the laser were optimized, and the pulse duration was evaluated by frequency-resolved optical gating (FROG). The XUV light was focused on the sample and CCD camera by a toroidal mirror whose parameters can be calculated and simulated by the optical formalisms and RAY-UI simulation. The use of XUV light and the samples with patterned gratings for a spectral analysis allows the investigation of spin dynamics with element selectivity. Since XUV light covers absorption edges of Ni and Pd, we traced the dynamics in both elemental Ni- and Pd subsystems simultaneously by integrating parts of the measured spectra corresponding to the absorption edges of the involved elements (see Chapter 4).

From static T-MOKE data with increasing Pd content, the magnetic asymmetry at the Pd absorption $N_{2,3}$-edge (51 eV) becomes more pronounced by induced magnetic moment of Pd due to complex exchange interaction with ferromagnetic Ni leading to a joint valence band structure of Ni and Pd. The measured magnetic asymmetries of $\mathrm{Ni}_x\mathrm{Pd}_{1-x}$ alloys are in good agreement with the calculations based on density-functional theory (DFT) (see Figure 5.3). Change of magnetic asymmetries in Ni and Pd could be interpreted by stoichiometry-dependent SOC and hybridization effect of the valence bands of Ni and Pd in the $\mathrm{Ni}_x\mathrm{Pd}_{1-x}$ alloys as discussed in Section 2.2.

Prior to the discussion of magnetization dynamics, the dynamics in Ni subsystem of $\mathrm{Ni}_{0.8}\mathrm{Pd}_{0.2}$ alloy under two different experimental conditions were compared. One was measured from the flat sample surface by monochromatized XUV ($\sim$ 67 eV) and the other one was from the sample surface with the grating structure by full spectrum (20-72 eV). No significant difference of the spin dynamics from two different configurations leads to the conclusion that the type of sample surface makes no effect on the spin dynamics. The observed element-selective spin dynamics in the $\mathrm{Ni}_{0.5}\mathrm{Pd}_{0.5}$ alloy indicates that Ni subsystem shows 30% faster demagnetization than that of Pd subsystem. Nevertheless, the presence of spin transport was not confirmed from our experimental results and OISTR between the subsystems is not valid in the magnetization dynamics of the NiPd alloys within the observed time scale. On the other hand, the dynamics of the Ni subsystem with varying stoichiometry gives indirect understanding of the effect of Pd on the dynamics of the alloys. Our studies result in two major conclusions. First, the magnetization dynamics of $\mathrm{Ni}_x\mathrm{Pd}_{1-x}$ alloys with constant pump fluence show higher amount of quenching and slower relaxation time with increasing Pd content. This observation has been shown to scale with T/T_C ratio. Such temperature dependence of magnetization dynamics was also demonstrated in early studies [2],[81]. Stoichiometry-dependent absorption of pump pulse on the sample surface was not taken into account due to its insignificant influence compared to Curie temperature. Second, the magnetization dynamics in Ni subsystem with constant magnetization quenching shows good agreement with calculation on the basis of microscopic three temperature model (M3TM). The analysis lets us conclude that Pd-mediated spin-orbit coupling (SOC) plays a crucial role in the dynamics of $\mathrm{Ni}_x\mathrm{Pd}_{1-x}$ alloys based on microscopic three temperature model (M3TM) [3] (see Chapter 5).

In this study, induced magnetization in intrinsically paramagnetic Pd subsystem due to complex exchange interaction with ferromagnetic Ni in $\mathrm{Ni}_x\mathrm{Pd}_{1-x}$ alloys and the magnetization dynamics were experimentally confirmed employing pump-probe T-MOKE. Taking advantage of the pulsed laser generated XUV radiation from HHG and its spectral analysis in T-MOKE geometry, magnetization dynamics of the $\mathrm{Ni}_x\mathrm{Pd}_{1-x}$ alloys was measured with element-selectivity. According to magnetization dynamics with varying stoichiometry, Pd-mediated SOC plays a decisive role in determination of the demagnetization time of Ni subsystem in $\mathrm{Ni}_x\mathrm{Pd}_{1-x}$ alloys.

Chapter 7

Outlook

The research of magnetization in intrinsically paramagnetic Pd alloyed with ferromagnetic Ni presented in this thesis could be expanded to unexplored candidate materials even to their magnetization dynamics. Regarding the magnetization dynamics, physical mechanism responsible for the dynamics is not clear and still under investigation. This study could be a small piece of puzzle to solve this question. In addition, scientific interest on this research would promote further experiments. Contrary to our confirmation of the strong influence of SOC on the demagnetization of the $\mathrm{Ni}_x\mathrm{Pd}_{1-x}$ alloys, our experiments did not conclusively confirm the presence of spin transfer between elemental subsystems in chemically disordered $\mathrm{Ni}_x\mathrm{Pd}_{1-x}$ alloys. Angular momentum transfer from Fe-rich to Gd-rich nanoregions during the optically-induced spin reversal of inhomogeneous GdFeCo was experimentally confirmed in Ref. [14]. According to the Ref. [17], theoretical effort also suggests spin transfer between sublattices in multilayer and alloy system via OISTR in short time scale. Thus, we cannot completely exclude the possibility of angular momentum transfer between the subsystems in the $\mathrm{Ni}_x\mathrm{Pd}_{1-x}$ alloys. Magnetization dynamics with shorter and more intense pump pulses might give more information about the spin transfer between subsystems in the magnetic alloy system, even in Ni/Pd multilayer. Further theoretical investigations of the magnetic asymmetry of $\mathrm{Ni}_x\mathrm{Pd}_{1-x}$ alloys could help to define the exact position of the absorption edges of the elemental subsystems. If the absorption edges are properly defined and possibly show no significant overlap, then the analysis of the dynamics in the Pd subsystem should be possible by further experiments using XUV light with higher photon flux. Further experiments could explore a possibility of magnetization switching using optically-induced spin current as well as technologically interesting combinations of materials including ferromagnet-semiconductor or FM-metal-FM oxides for novel functionalities in data processing spintronic devices.

Appendix

Multipass Amplification Process

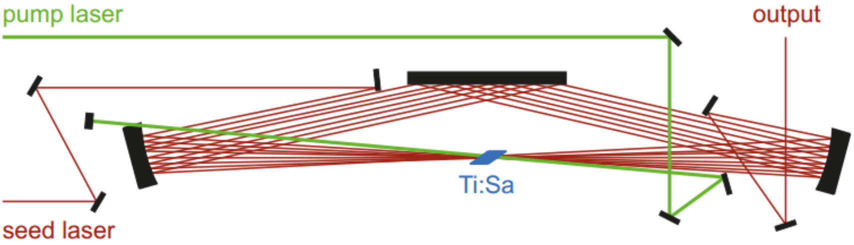

Figure 1: Schematics of the multipass amplification process [64], [69]. Laser pulse is amplified by geometrically arranged multiple passes of the laser through gain medium (Na). The gain medium has a limited gain which can be solved by making proper overlap of different beam paths on the Ti:Sapphire crystal(gain medium) pumped by a pump laser. Amplification depends on the overlap of the multiple paths and the overlap is efficient if the crystal is thin.

RAY-UI Software for Optical Simulation

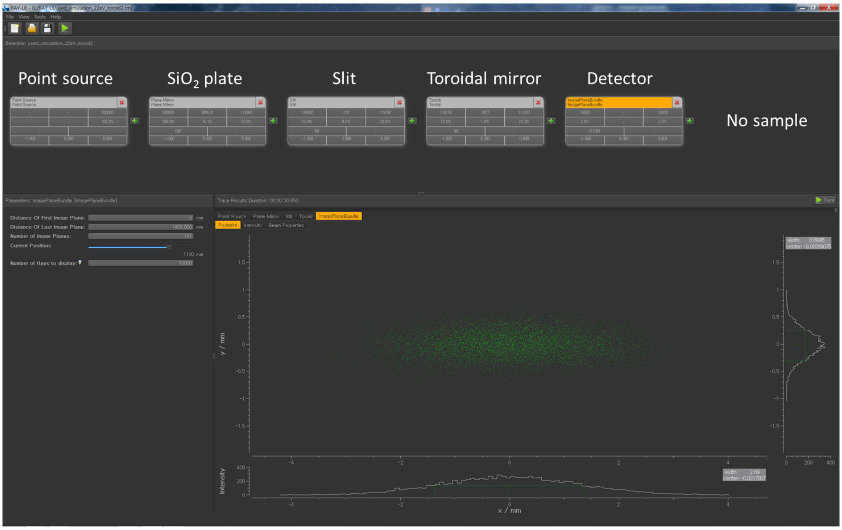

Parameters: ImagePlaneBundle [ImagePlaneBundle]

Distance Of First Image Plane: 0 mm
Distance Of Last Image Plane: 1400,000 mm
Number of Image Planes: 141
Current Position: 1100 mm
Number of Rays to display: 10000

FIGURE 2: Screenshot of RAY-UI for optical simulation. As the toroidal mirror is used to focus the probe- and pump pulse on the sample and CCD for better spectral resolution. The parameters of the toroidal mirror can be simulated by RAY-UI according to the experimental geometry. Optics can be freely added in the beam path as desired. The intensities and profiles of transmitted- and reflected light source can be traced by the software.

MATLAB Source Code for Subpixel Shift Correction of Spectra

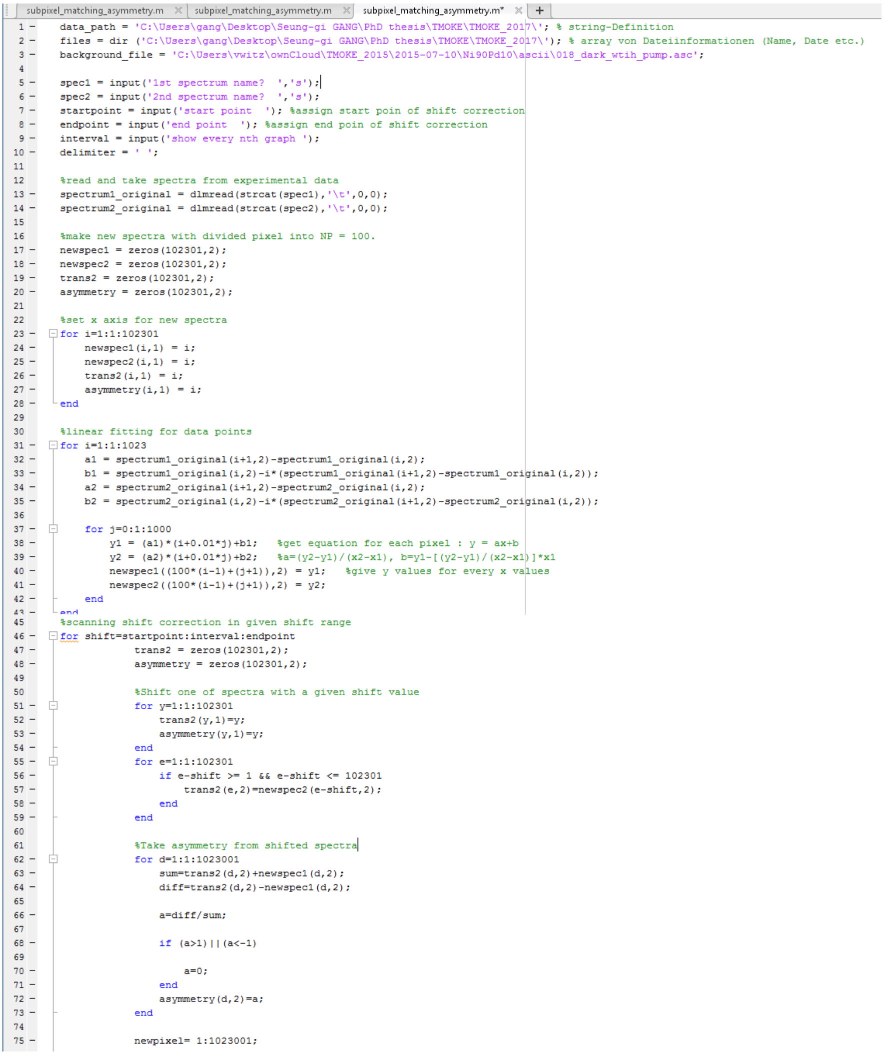

```matlab
data_path = 'C:\Users\gang\Desktop\Seung-gi GANG\PhD thesis\TMOKE\TMOKE_2017\'; % string-Definition
files = dir ('C:\Users\gang\Desktop\Seung-gi GANG\PhD thesis\TMOKE\TMOKE_2017\'); % array von Dateiinformationen (Name, Date etc.)
background_file = 'C:\Users\vwitz\ownCloud\TMOKE_2015\2015-07-10\Ni90Pd10\ascii\018_dark_wtih_pump.asc';

spec1 = input('1st spectrum name?  ','s');
spec2 = input('2nd spectrum name?  ','s');
startpoint = input('start point  '); %assign start poin of shift correction
endpoint = input('end point  '); %assign end poin of shift correction
interval = input('show every nth graph ');
delimiter = ' ';

%read and take spectra from experimental data
spectrum1_original = dlmread(strcat(spec1),'\t',0,0);
spectrum2_original = dlmread(strcat(spec2),'\t',0,0);

%make new spectra with divided pixel into NP = 100.
newspec1 = zeros(102301,2);
newspec2 = zeros(102301,2);
trans2 = zeros(102301,2);
asymmetry = zeros(102301,2);

%set x axis for new spectra
for i=1:1:102301
    newspec1(i,1) = i;
    newspec2(i,1) = i;
    trans2(i,1) = i;
    asymmetry(i,1) = i;
end

%linear fitting for data points
for i=1:1:1023
    a1 = spectrum1_original(i+1,2)-spectrum1_original(i,2);
    b1 = spectrum1_original(i,2)-i*(spectrum1_original(i+1,2)-spectrum1_original(i,2));
    a2 = spectrum2_original(i+1,2)-spectrum2_original(i,2);
    b2 = spectrum2_original(i,2)-i*(spectrum2_original(i+1,2)-spectrum2_original(i,2));

    for j=0:1:1000
        y1 = (a1)*(i+0.01*j)+b1;   %get equation for each pixel : y = ax+b
        y2 = (a2)*(i+0.01*j)+b2;   %a=(y2-y1)/(x2-x1), b=y1-[(y2-y1)/(x2-x1)]*x1
        newspec1((100*(i-1)+(j+1)),2) = y1;   %give y values for every x values
        newspec2((100*(i-1)+(j+1)),2) = y2;
    end
end
%scanning shift correction in given shift range
for shift=startpoint:interval:endpoint
            trans2 = zeros(102301,2);
            asymmetry = zeros(102301,2);

            %Shift one of spectra with a given shift value
            for y=1:1:102301
                trans2(y,1)=y;
                asymmetry(y,1)=y;
            end
            for e=1:1:102301
                if e-shift >= 1 && e-shift <= 102301
                    trans2(e,2)=newspec2(e-shift,2);
                end
            end

            %Take asymmetry from shifted spectra
            for d=1:1:1023001
                sum=trans2(d,2)+newspec1(d,2);
                diff=trans2(d,2)-newspec1(d,2);

                a=diff/sum;

                if (a>1)||(a<-1)

                    a=0;
                end
                asymmetry(d,2)=a;
            end

            newpixel= 1:1023001;
```

FIGURE 3: MATLAB code for subpixel shift correction. If the magnetic field is applied to the magnetic sample, then the sample can be slightly moved leading to the offset between spectra. If the offset is larger than a single pixel, then the offset can be compensated by simply moving one of the spectra by unit of pixel. If the offset is smaller than a single pixel, the shift correction can be done by dividing a pixel into smaller segments and moving the segments. The process of the subpixel correction is given as the MATLAB code.

Element-Selective Spin Dynamics for Four Different Spectral Regions in $Ni_{0.5}Pd_{0.5}$ Alloy

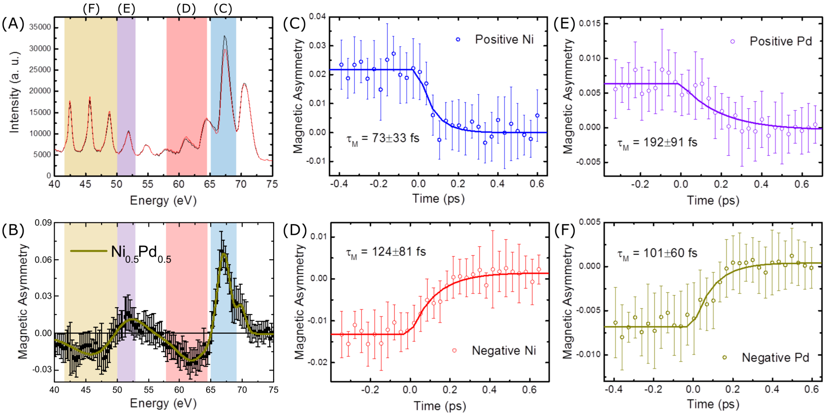

FIGURE 4: Element-selective magnetization dynamics from 4 different parts of Ni- and Pd asymmetries. (A) Spectra of XUV source reflected on $Ni_{0.5}Pd_{0.5}$ thin film showing 4 different parts; positive- and negative part of Ni and Pd (B) Magnetic asymmetry taken from the spectra(A) Magnetization dynamics in (C) positive part of Ni asymmetry, (D) negative part of Ni asymmetry, (E) Positive part of Pd asymmetry and (F) negative part of Pd asymmetry. Both Ni and Pd show bipolar shape of magnetic asymmetries. We checked magnetization dynamics in 4 different parts of the asymmetries; positive- and negative parts of Ni and Pd. Each part shows different dynamics which needs more discussion. Positive part of Ni asymmetry shows the shortest demagtization time and the positive part of Pd asymmetry exhibits the longest demagnetization time.

Abbreviations

3TM	**T**hree-**T**emperature **M**odel
AFM	**A**tomic **F**orce **M**icroscope
CCD	**C**harge-**C**oupled **D**evice
CPA	**C**hirped **P**ulse **A**mplification
FELs	**F**ree **E**lectron **L**asers
FROG	**F**requency-**R**esolved **O**ptical **G**ating
HHG	**H**igh **H**armonic **G**eneration
L-MOKE	**L**ongitudinal **M**agneto-**O**ptic **K**err **E**ffect
M3TM	**M**icroscopic **3** **T**emperature **M**odel
MBE	**M**olecular **B**eam **E**pitaxy
MO	**M**agneto **O**ptics
MOKE	**M**agneto-**O**ptic **K**err **E**ffect
OISTR	**O**ptically-induced **I**ntersite **S**pin **Tr**ansfer
RIBE	**R**eactive **I**on **B**eam **E**tching
P-MOKE	**P**olar **M**agneto-**O**ptic **K**err **E**ffect
SHG	**S**econd **H**armonic **G**eneration
SO	**S**pin **O**rbit
SOC	**S**pin **O**rbit **C**oupling
SRT	**S**pin **R**eorientation **T**ransition
TBP	**T**ime-**B**andwidth **P**roduct
T-MOKE	**T**ransversal **M**agneto-**O**ptic **K**err **E**ffect
TR-MOKE	**T**ime **R**esolved **M**agneto-**O**ptic **K**err **E**ffect
XUV	**E**x**t**reme **U**ltra**v**iolet

Bibliography

[1] S Valencia, A Kleibert, A Gaupp, J Rusz, D Legut, J Bansmann, W Gudat, and P M Oppeneer. Quadratic X-Ray Magneto-Optical Effect upon Reflection in a Near-Normal-Incidence Configuration at the M Edges of 3 d-Transition Metals. *Phys. Rev. Lett.*, 104(18):187401, 2010.

[2] T Roth, A J Schellekens, S Alebrand, O Schmitt, D Steil, B Koopmans, M Cinchetti, and M Aeschlimann. Temperature dependence of laser-induced demagnetization in Ni: A key for identifying the underlying mechanism. *Phys. Rev. X*, 2(2):021006, 2012.

[3] B Koopmans, G Malinowski, F Dalla Longa, D Steiauf, M Fähnle, T Roth, M Cinchetti, and M Aeschlimann. Explaining the paradoxical diversity of ultrafast laser-induced demagnetization. *Nat. Mater.*, 9(3):259, 2010.

[4] M Battiato, K Carva, and P M Oppeneer. Superdiffusive spin transport as a mechanism of ultrafast demagnetization. *Phys. Rev. Lett.*, 105(2):027203, 2010.

[5] D Rudolf, La-O Chan, M Battiato, R Adam, J M Shaw, E Turgut, P Maldonado, S Mathias, P Grychtol, H T Nembach, et al. Ultrafast magnetization enhancement in metallic multilayers driven by superdiffusive spin current. *Nat. Commun.*, 3: 1037, 2012.

[6] E Beaurepaire, J-C Merle, A Daunois, and J-Y Bigot. Ultrafast spin dynamics in ferromagnetic nickel. *Phys. Rev. Lett.*, 76(22):4250, 1996.

[7] M Aeschlimann, M Bauer, S Pawlik, W Weber, R Burgermeister, D Oberli, and H C Siegmann. Ultrafast spin-dependent electron dynamics in fcc Co. *Phys. Rev. Lett.*, 79(25):5158, 1997.

[8] G Malinowski, F Dalla Longa, J H H Rietjens, P V Paluskar, R Huijink, H J M Swagten, and B Koopmans. Control of speed and efficiency of ultrafast demagnetization by direct transfer of spin angular momentum. *Nat. Phys.*, 4(11):855, 2008.

[9] A Melnikov, I Razdolski, T O Wehling, E Th Papaioannou, V Roddatis, P Fumagalli, O Aktsipetrov, A I Lichtenstein, and U Bovensiepen. Ultrafast transport of laser-excited spin-polarized carriers in Au/Fe/MgO (001). *Phys. Rev. Lett.*, 107(7): 076601, 2011.

[10] A Eschenlohr, M Battiato, P Maldonado, N Pontius, T Kachel, K Holldack, R Mitzner, A Föhlisch, P M Oppeneer, and C Stamm. Ultrafast spin transport as key to femtosecond demagnetization. *Nat. Mater.*, 12(4):332, 2013.

[11] E Turgut, J M Shaw, P Grychtol, H T Nembach, D Rudolf, R Adam, M Aeschlimann, C M Schneider, T J Silva, M M Murnane, et al. Controlling the competition between optically induced ultrafast spin-flip scattering and spin transport in magnetic multilayers. *Phys. Rev. Lett.*, 110(19):197201, 2013.

[12] I Radu, K Vahaplar, C Stamm, T Kachel, N Pontius, H A Dürr, T A Ostler, J Barker, R F L Evans, R W Chantrell, et al. Transient ferromagnetic-like state mediating ultrafast reversal of antiferromagnetically coupled spins. *Nature*, 472 (7342):205, 2011.

[13] T A Ostler, J Barker, R F L Evans, R W Chantrell, U Atxitia, O Chubykalo-Fesenko, S El Moussaoui, L B P J Le Guyader, E Mengotti, L J Heyderman, et al. Ultrafast heating as a sufficient stimulus for magnetization reversal in a ferrimagnet. *Nat. Commun.*, 3:666, 2012.

[14] C E Graves, A H Reid, T Wang, B Wu, S De Jong, K Vahaplar, I Radu, D P Bernstein, M Messerschmidt, L Müller, et al. Nanoscale spin reversal by non-local angular momentum transfer following ultrafast laser excitation in ferrimagnetic GdFeCo. *Nat. Mater.*, 12(4):293, 2013.

[15] V G Bar'yakhtar. Zh. É ksp. Teor. Fiz. 87, 1501 1984 Sov. Phys. *Sov. Phys. JETP*, 60:863, 1984.

[16] V G Bar'yakhtar, V I Butrim, and B A Ivanov. Exchange relaxation as a mechanism of the ultrafast reorientation of spins in a two-sublattice ferrimagnet. *JETP Lett.*, 98(5):289–293, 2013.

[17] John Kay Dewhurst, Peter Elliott, Sam Shallcross, Eberhard K. U. Gross, and Sangeeta Sharma. Laser-Induced Intersite Spin Transfer. *Nano letters*, 18(3):1842–1848, 2018.

[18] U Muschiol, M Seider, CM Schneider, and M-T Lin. Electronic structure of epitaxial Ni x Pd 1- x alloy films on Cu 3 Au (100). *Journal of Applied Physics*, 89(11):6892–6894, 2001.

[19] J Stöhr and H C Siegmann. Magnetism. *Solid State Sci. Springer, Berlin, Heidelberg*, 5, 2006.

[20] M Plötzing. Laser-Induced Ultrafast Electron- and Spin-Dynamics in the Electron Band Structure of Co(001), PhD thesis, University of Duisburg-Essen and Forschungszentrum Jülich, 2016.

[21] W Gerlach and O Stern. Der experimentelle nachweis der richtungsquantelung im magnetfeld. *Z. Phys.*, 9(1):349–352, 1922.

[22] Charles Kittel. On the gyromagnetic ratio and spectroscopic splitting factor of ferromagnetic substances. *Physical Review*, 76(6):743, 1949.

[23] J Pelzl, R Meckenstock, D Spoddig, F Schreiber, J Pflaum, and Z Frait. Spin–orbit-coupling effects on g-value and damping factor of the ferromagnetic resonance in Co and Fe films. *Journal of Physics: Condensed Matter*, 15(5):S451, 2003.

[24] W Heisenberg. W. Heisenberg, Zeits. f. Physik 39, 499 (1926). *Zeits. f. Physik*, 39: 499, 1926.

[25] Paul Adrien Maurice Dirac. On the theory of quantum mechanics. *Proc. R. Soc. Lond. A*, 112(762):661–677, 1926.

[26] D E Bürgler. *Memristive Phenomena - From Fundamental Physics to Neuromorphic Computing, A8.* Forschungszentrum Jülich GmbH, 2016.

[27] S Blundell. *Magnetism in Condensed Matter (Oxford master series in condensed matter physics.* Oxford University Press, 2001.

[28] W PAULI Jr. On the quantum mechanics of magnetic electrons. *Nature*, 119:282, 1927.

[29] P Strange. *Relativistic quantum mechanics: with applications in condensed matter and atomic physics.* Cambridge University Press, 1998.

[30] EC Stoner. EC Stoner, Proc. Roy. Soc. 154, 656 (1936). *Proc. Roy. Soc.*, 154:656, 1936.

[31] EC Stoner. EC Stoner, Proc. R. Soc. London, Ser. A 165, 372 (1938). *Proc. R. Soc. London, Ser. A*, 165:372, 1938.

[32] CM Teodorescu and GA Lungu. Band ferromagnetism in systems of variable dimensionality. *Journal of Optoelectronics and Advanced Materials*, 10(11):3058–3068, 2008.

[33] P Mohn. *Magnetism in the solid state: an introduction*, volume 134. Springer Science & Business Media, 2006.

[34] O Gunnarsson. Band model for magnetism of transition metals in the spin-density-functional formalism. *J. Phys. F Met. Phys.*, 6(4):587, 1976.

[35] Robert D Cowan. *The theory of atomic structure and spectra.* Number 3. Univ of California Press, 1981.

[36] La-O Chan, Mark Siemens, Margaret M Murnane, Henry C Kapteyn, Stefan Mathias, Martin Aeschlimann, Patrik Grychtol, Roman Adam, Claus M Schneider, Justin M Shaw, et al. Ultrafast demagnetization dynamics at the M edges of magnetic elements observed using a tabletop high-harmonic soft X-ray source. *Physical Review Letters*, 103(25):257402, 2009.

[37] JH Mentink, Johan Hellsvik, DV Afanasiev, BA Ivanov, Andrei Kirilyuk, AV Kimel, Olle Eriksson, MI Katsnelson, and Th Rasing. Ultrafast spin dynamics in multi-sublattice magnets. *Physical review letters*, 108(5):057202, 2012.

[38] S Mathias, La-O Chan, P Grychtol, P Granitzka, E Turgut, J M Shaw, R Adam, H T Nembach, M E Siemens, S Eich, et al. Probing the timescale of the exchange interaction in a ferromagnetic alloy. *P. Natl. A. Sci*, 109(13):4792–4797, 2012.

[39] GR Harp, D Weller, TA Rabedeau, RFC Farrow, and MF Toney. Magneto-optical Kerr spectroscopy of a new chemically ordered alloy: Co 3 Pt. *Physical review letters*, 71(15):2493, 1993.

[40] H Ibach and H Lüth. Festkörperphysik: Einführung in die Grundlagen, 2009.

[41] H P J Wijn. *Magnetic Properties of Metals: D-Elements, Alloys and Compounds.* Springer Science & Business Media, 1991.

[42] M Seider, R Kaltofen, U Muschiol, M-T Lin, and CM Schneider. Growth and magnetic properties of thin epitaxial Ni x Pd 1- x alloy films on Cu 3 Au (100). *Journal of Applied Physics*, 87(9):5762–5764, 2000.

[43] Victor L Moruzzi, James F Janak, and Arthur R Williams. *Calculated electronic properties of metals.* Elsevier, 2013.

[44] W Kuch. W. Kuch, A. Dittschar, K. Meinel, M. Zharnikov, CM Schneider, J. Kirschner, J. Henk, and R. Feder, Phys. Rev. B 53, 11621 (1996). *Phys. Rev. B*, 53:11621, 1996.

[45] B Schmiedeskamp, B Kessler, Norbert Müller, G Schönhense, and Ulrich Heinzmann. Spin-resolved photoemission from Pd (111). *Solid state communications*, 65 (7):665–670, 1988.

[46] S Mathias, J M Shaw, E Turgut, P Grychtol, R Adam, D Rudolf, H T Nembach, T J Silva, M Aeschlimann, C M Schneider, et al. Ultrafast element-specific magnetization dynamics of complex magnetic materials on a table-top. *J. Electron Spectrosc.*, 189:164–170, 2013.

[47] T Kampfrath, M Battiato, P Maldonado, G Eilers, J Nötzold, S Mährlein, V Zbarsky, F Freimuth, Y Mokrousov, S Blügel, et al. Terahertz spin current pulses controlled by magnetic heterostructures. *Nat. Nanotechnol.*, 8(4):256, 2013.

[48] M Faraday. Experimental researches in electricity. Nineteenth series. *Philos. T. R. Soc. Lond.*, 136:1–20, 1846.

[49] J Kerr. XLIII. On rotation of the plane of polarization by reflection from the pole of a magnet. *Lond. Edinb. Dubl. Phil. Mag.*, 3(19):321–343, 1877.

[50] M Plötzing. Ultrafast Demagnetization Dynamics in Ni_xPd_{1-x}-alloys, Master's Thesis, RWTH Aachen University, 2011.

[51] P M Oppeneer. Magneto-optical Kerr spectra. *Handbook of Magnetic Materials*, 13:229–422, 2001.

[52] A A Zholents and M S Zolotorev. Femtosecond x-ray pulses of synchrotron radiation. *Phys. Rev. Lett.*, 76(6):912, 1996.

[53] B Pfau, S Schaffert, L Müller, C Gutt, A Al-Shemmary, F Büttner, R Delaunay, S Düsterer, S Flewett, R Frömter, et al. Ultrafast optical demagnetization manipulates nanoscale spin structure in domain walls. *Nat. Commun.*, 3:1100, 2012.

[54] A McPherson, G Gibson, H Jara, U Johann, T S Luk, I A McIntyre, K Boyer, and C K Rhodes. Studies of multiphoton production of vacuum-ultraviolet radiation in the rare gases. *JOSA B*, 4(4):595–601, 1987.

[55] T Pfeifer, Ch Spielmann, and G Gerber. Femtosecond x-ray science. *Rep. Prog. Phys.*, 69(2):443, 2006.

[56] C Winterfeldt. Generation and control of high-harmonic radiation. 2006.

[57] C C Gunatilaka and K A I L Wijewardena Gamalath. Electron dynamics in a strong laser field. *World Scientific News*, 35:1–16, 2016.

[58] J-Y Chauleau, B J McMorran, R Belkhou, N Bergeard, T O Menteş, M A Nino, A Locatelli, J Unguris, S Rohart, J Miltat, et al. Magnetization textures in NiPd nanostructures. *Phys. Rev. B*, 84(9):094416, 2011.

[59] D L Windt. IMD—Software for modeling the optical properties of multilayer films. *Computers in physics*, 12(4):360–370, 1998.

[60] $http://henke.lbl.gov/optical_constants$.

[61] S W Lovesey and S P Collins. *X-ray scattering and absorption by magnetic materials*. Number 1. Oxford University Press, 1996.

[62] K-H Hellwege. über rasterförmige Reflexionsgitter. *Zeitschrift für Physik A Hadrons and Nuclei*, 106(9):588–596, 1937.

[63] K-H Hellwege. Über rasterförmige Reflexionsgitter, Nachtrag. *Zeitschrift für Physik A Hadrons and Nuclei*, 111(7):495–497, 1939.

[64] M von Witzleben. Element-selective studies of magnetization dynamics in $\mathrm{Ni}_x\mathrm{Pd}_{1-x}$-alloys, Master's Thesis, RWTH Aachen University, 2015.

[65] W Demtröder. Aufbau der Atomkerne. In *Experimentalphysik 2: Electrizität und Optik*. Springer-Verlag, 2014.

[66] Michael Perry, B Shore, R Boyd, and J Britten. Multilayer dielectric gratings: Increasing the power of light. *Science & Technology Review*, 9:25–33, 1995.

[67] J-C Diels and W Rudolph. *Ultrashort laser pulse phenomena: fundamentals, techniques, and applications on a femtosecond time scale*. Elsevier, 2006.

[68] R Trebino. *Frequency-resolved optical gating: the measurement of ultrashort laser pulses*. Springer Science & Business Media, 2012.

[69] S Backus, Charles G Durfee III, M M Murnane, and Henry C Kapteyn. High power ultrafast lasers. *Rev. Sci. Instrum.*, 69(3):1207–1223, 1998.

[70] R Paschotta. Solid state lasers for ultrashort pulses-a diverse family. *PHOTONIK-STUTTGART-*, 39(I):56, 2007.

[71] J H Apfel. Phase retardance of periodic multilayer mirrors. *Appl. Optics*, 21(4): 733–738, 1982.

[72] *https://www.shimadzu.com/opt/guide/diffraction/11.html*.

[73] P Grychtol, R Adam, S Valencia, S Cramm, D E Bürgler, and C M Schneider. Resonant magnetic reflectivity in the extreme ultraviolet spectral range: Interlayer-coupled Co/Si/Ni/Fe multilayer system. *Phys. Rev. B*, 82(5):054433, 2010.

[74] M Hecker, P M Oppeneer, S Valencia, H-Ch Mertins, and C M Schneider. Soft X-ray magnetic reflection spectroscopy at the 3p absorption edges of thin Fe films. *J. Electron Spectrosc.*, 144:881–884, 2005.

[75] P Yeh. Optics of anisotropic layered media: a new 4× 4 matrix algebra. *Surf. Sci.*, 96(1-3):41–53, 1980.

[76] Š Višňovskỳ. Optics of magnetic multilayers. *Czech. J. Phys.*, 41:663–694, 1991.

[77] A Thompson, D Attwood, E Gullikson, M Howells, K J Kim, J Kirz, J Kortright, I Lindau, Y Liu, P Pianetta, et al. X-ray Data Booklet, Vol. 3. *Berkeley California: Lawrence Berkeley National Laboratory*, 2009.

[78] N Bergeard, V López-Flores, V Halté, M Hehn, C Stamm, N Pontius, E Beaurepaire, and C Boeglin. Ultrafast angular momentum transfer in multisublattice ferrimagnets. *Nat. Commun.*, 5:3466, 2014.

[79] K C Kuiper, T Roth, A J Schellekens, O Schmitt, B Koopmans, M Cinchetti, and M Aeschlimann. Spin-orbit enhanced demagnetization rate in Co/Pt-multilayers. *Appl. Phys. Lett.*, 105(20):202402, 2014.

[80] S Wienholdt, D Hinzke, K Carva, P M Oppeneer, and U Nowak. Orbital-resolved spin model for thermal magnetization switching in rare-earth-based ferrimagnets. *Phys. Rev. B*, 88(2):020406, 2013.

[81] BY Mueller, A Baral, S Vollmar, M Cinchetti, M Aeschlimann, HC Schneider, and B Rethfeld. Feedback effect during ultrafast demagnetization dynamics in ferromagnets. *Physical review letters*, 111(16):167204, 2013.

[82] F Willems, C T L Smeenk, N Zhavoronkov, O Kornilov, I Radu, M Schmidbauer, M Hanke, C von Korff Schmising, M J J Vrakking, and S Eisebitt. Probing ultrafast spin dynamics with high-harmonic magnetic circular dichroism spectroscopy. *Phys. Rev. B*, 92(22):220405, 2015.

[83] K Carva, M Battiato, and P M Oppeneer. Ab initio investigation of the Elliott-Yafet electron-phonon mechanism in laser-induced ultrafast demagnetization. *Phys. Rev. Letters*, 107(20):207201, 2011.

Publications and Conference Contributions

Publication

2018	Physical Review B (Article) Element-selective investigation of femtosecond spin dynamics in NiPd magnetic alloys using extreme ultraviolet radiation S. Gang, R. Adam, M. Plötzing, M. von Witzleben, C. Weier, U. Parlak, D. E. Bürgler, J. Rusz, P. Maldonado, P. M. Oppeneer, C. M. Schneider Phys. Rev. B **97**, 064412 (2018)

Talks

2017	Ultrafast Magnetism Conference, Kaiserslautern (Talk) Element-selective investigation of femtosecond spin dynamics in Ni_xPd_{1-x} magnetic alloys using extreme ultraviolet radiation
2017	DPG Spring meeting, Dresden (Talk) Femtosecond spin dynamics in Ni_xPd_{1-x} magnetic alloys

Posters

2016 PoF-3 Scientific Exchange Meeting, Jülich (Poster)
Element-selective investigation of the spin dynamics in $\mathrm{Ni}_x\mathrm{Pd}_{1-x}$ magnetic alloys in the extreme ultraviolet spectral range

2016 8^{th} Joint European Magnetic Symposia, Glasgow (Poster)
Element-selective investigation of the spin dynamics in $\mathrm{Ni}_x\mathrm{Pd}_{1-x}$ magnetic alloys in the extreme ultraviolet spectral range

2016 DPG Spring meeting, Regensburg (Poster)
Element-selective investigation of the spin dynamics in $\mathrm{Ni}_x\mathrm{Pd}_{1-x}$ magnetic alloys in the extreme ultraviolet spectral range

Curriculum Vitae

PersonalDetails

Name:	Seung-gi Gang
Date of Birth:	24th February 1984
Place of Birth:	Jinju, Republic of Korea

Education

Since 2014	PhD at University of Duisburg-Essen and Forschungszentrum Jülich, PGI-6 Subject: Element-selective investigation of femtosecond spin dynamics in NiPd magnetic alloys using extreme ultraviolet radiation
2010-2012	Mater in Material Science and Engineering at Gwangju Institute of Science and Technology (GIST), Korea Subject: Femtosecond Soft X-ray High Harmonic Generation using a Ti:Sapphire Laser
2002-2010	Bachelor in Applied Physics at Hanyang University, Korea Subject: Nonlinearity of Mach-Zehnder Modulation

AdditionalActivities

2012-2014	Researcher at Korea Atomic Energy Research Institute, Korea Subject: Hydrogen absorption methods for hydrogen storage materials, Physisorption, Chemisorption and Spillover Experimental tools: (in-situ) Raman spectroscopy, Neutron scattering, XPS, ESR

Acknowledgements

I would like to express my special thanks and appreciation to all the people who made this work possible with their effort. In particular, I am grateful to:

Prof. Claus M. Schneider for giving me an opportunity to join his institute as a PhD student in the nice environment. Thank you for supervising my PhD project with comments which inspired and motivated me.

Dr. Roman Adam for accepting me in his group. I was lucky that he supervised my research and provided words of encouragement. I was always inspired by his amazing passion. I never forget his support with patience.

Dr. Daniel E. Bürgler for providing me valuable support which made this work possible.

I would like to give my special thanks to **Dr. Christian Weier**. He helped me to get used to the laser lab and gave me nice instruction and memories in the lab with fun.

Dr. Moritz Plötzing for giving me opportunities to learn his work. I was able to get used to the lab work with his support.

Moritz von Witzleben for having fun to build T-MOKE setup together. We had argument and discussion continuously which made the experiments possible.

Umut Parlak for providing samples for my PhD research and sharing many things as being in the similar circumstances. I was impressed for his dedication and effort for research.

Jan Rusz, **Pablo Maldonado**, and **Prof. Peter M. Oppeneer** from Upsala university for providing valuable feedback and calculations supproting the experimental results.

Jürgen Lauer and **Norbert Schnitzler** for providing us nice software which made stable and systematic measurements possible.

Heinz Pfeifer, **Arnd Bremen**, **Bernd Küper**, **PGI workshop** for technical supporting which provides many options we can apply to the experiments.

I would also like to thank **all PGI-6 members** including **Frau Margret Frey, Dr. Markus Eschbach, Dr. Christoph Schmitz, Dr. Volkmar Hess, Patrick Lömker, Fabian Fritz, Pika Gospodaric, Ewa Mlynczak, Christian Greb, Sarah Heidtfeld**.

I would like to my special thanks to my family and, especially, to my dear **Youran** and my son **Ian** for their invaluable emotional support.

Band / Volume 44
Quantitative scanning tunneling spectroscopy of non-polar III-V compound semiconductor surfaces
M. Schnedler (2015), 122 pp
ISBN: 978-3-95806-075-3

Band / Volume 45
Model-based Algorithm Development with Focus on Biosignal Processing
Y. Yao (2015), x, 169 pp
ISBN: 978-3-95806-080-7

Band / Volume 46
Growth and characterization of crystalline rare-earth based thin oxide fims for the application as gate dielectric in nanotechnology
A. B. Schäfer (2015), xiii, 157 pp
ISBN: 978-3-95806-111-8

Band / Volume 47
TEM/STEM Investigations of Phase Change Materials for Non-volatile Memory Applications
M. Bornhöfft (2017), viii, 135 pp
ISBN: 978-3-95806-221-4

Band / Volume 48
Investigation of ternary nitride semiconductor alloys by scanning tunneling microscopy
V. Portz (2017), 140 pp
ISBN: 978-3-95806-232-0

Band / Volume 49
Redox processes and ionic transport in resistive switching binary metal oxides
K. Skaja (2017), VII, 203 pp
ISBN: 978-3-95806-236-8

Band / Volume 50
Investigation of switching mechanism in Ta_2O_5 -based ReRAM devices
K. Wonjoo (2017), iii, 138 pp
ISBN: 978-3-95806-261-0

Band / Volume 51
Development of ReRAM-based Devices for Logic- and Computation-in-Memory Applications
T. Breuer (2017), x, 179 pp
ISBN: 978-3-95806-270-2

Band / Volume 52
Resistive switching memory devices from atomic layer deposited binary and ternary oxide thin films
N. Aslam (2017), X, 172 pp
ISBN: 978-3-95806-274-0

Band / Volume 53
Operando X-ray photoemission electron microscopy (XPEEM) investigations of resistive switching metal-insulator-metal devices
C. J. Schmitz (2017), IX, 153 pp
ISBN: 978-3-95806-283-2

Band / Volume 54
Optimization of powder and ceramic processing, electrical characterization and defect chemistry in the system $Yb_xCa_{1-x}MnO_3$
M. Rahmani (2018), XIV, 164 pp
ISBN: 978-3-95806-323-5

Band / Volume 55
Organic-Metal Hybrid Interfaces at the Mesoscopic Scale
G. Zamborlini (2018), xi, 133 pp
ISBN: 978-3-95806-328-0

Band / Volume 56
Configurable frequency synthesizer for large scale physics experiments
N. Parkalian (2019), xxi, 114 pp
ISBN: 978-3-95806-393-8

Band / Volume 57
Resistive switching phenomena in stacks of binary transition metal oxides grown by atomic layer deposition
H. Zhang (2019), ix, 196 pp
ISBN: 978-3-95806-399-0

Band / Volume 58
Element-Selective Investigation of Femtosecond Spin Dynamics in Ni_xPd_{1-x} Magnetic Alloys using Extreme Ultraviolet Radiation
S. Gang (2019), 93, xx pp
ISBN: 978-3-95806-411-9

Weitere ***Schriften des Verlags im Forschungszentrum Jülich*** unter
http://wwwzb1.fz-juelich.de/verlagextern1/index.asp

Information
Band / Volume 58
ISBN 978-3-95806-411-9

Mitglied der Helmholtz-Gemeinschaft

JÜLICH
Forschungszentrum